



저작자표시-비영리-변경금지 2.0 대한민국

이용자는 아래의 조건을 따르는 경우에 한하여 자유롭게

- 이 저작물을 복제, 배포, 전송, 전시, 공연 및 방송할 수 있습니다.

다음과 같은 조건을 따라야 합니다:



저작자표시. 귀하는 원저작자를 표시하여야 합니다.



비영리. 귀하는 이 저작물을 영리 목적으로 이용할 수 없습니다.



변경금지. 귀하는 이 저작물을 개작, 변형 또는 가공할 수 없습니다.

- 귀하는, 이 저작물의 재이용이나 배포의 경우, 이 저작물에 적용된 이용허락조건을 명확하게 나타내어야 합니다.
- 저작권자로부터 별도의 허가를 받으면 이러한 조건들은 적용되지 않습니다.

저작권법에 따른 이용자의 권리는 위의 내용에 의하여 영향을 받지 않습니다.

이것은 [이용허락규약\(Legal Code\)](#)을 이해하기 쉽게 요약한 것입니다.

[Disclaimer](#)

공학박사 학위논문

능동적 학습과 설계 프로그래밍을 이용하여 효율적  
인 3D 프린팅을 위한 반자동 작업 과정  
및 임상적 유용성

Semi-automated workflow for efficient 3D  
printing including segmentation, design, and  
measurement in medicine, and its clinical  
usability using active learning and CAD  
programming

울산대학교 대학원

의과학과

김태훈

능동적 학습과 설계 프로그래밍을 이용하여 효율적  
인 3D 프린팅을 위한 반자동 작업 과정  
및 임상적 유용성

지도교수 김 남 국 고 범 석

이 논문을 공학박사 학위 논문으로 제출함

2023 년 8 월

울산대학교대학원  
의 과 학 과  
김 태 훈

김태훈의 공학박사 학위 논문을 인준함

심사위원장 양 동 현 (인)

심사위원 김 남 국 (인)

심사위원 고 범 석 (인)

심사위원 김 국 배 (인)

심사위원 유 진 수 (인)

울산대학교대학원

2023년 8월

## **Abstract**

In the field of medicine, 3D printing (3DP) technology has been applied to patient-specific surgical guides, simulators, surgical planning, education, implants. The essential tasks such as image acquisition, segmentation, 3D computer aided design (CAD) modeling, or measurements must be performed in medical field. However, these tasks can be repetitive, time-consuming, labor-intensive, and lack of consistency. To address these shortcomings, improvements can be achieved by segmenting CT images using deep learning, generating a 3D model, and performing semi-automated modeling using a script-based application programming interface (API). This study was conducted in three parts: 1) Active learning (AL) was utilized to automated and enhanced segmentation, reducing the labeling workload, 2) automated patient-specific modeling and measurement of landmarks were achieved through the 3D models based on automated segmentation using script-based application programming interfaces (API), and 3) the usefulness and efficiency of patient-specific surgical guides produced using 3DP technology were demonstrated with clinical application.

Firstly, medical image segmentation is essential to obtain various information within the human body, providing visualization of anatomical structures and information on diagnosis, surgical planning, organs, or lesions for medical professionals. Conventional image segmentation often involves manual segmentation on a pixel-by-pixel basis using various tools. However, these segmentation methods often face difficulties in achieving consistent segmentation due to various factors such as low contrast and image noise, leading to significant time consumption. In recent years, significant advances in image segmentation have been made using deep learning models such as convolution neural networks (CNN), fully convolutional networks (FCN), and U-Net. In this study, we introduced an AL approach for enhanced segmentation using a smart labeling, which efficiently increases labeled data by training on a small initial dataset with manually labeled data and correcting the predicted new data with human experts in kidney CT with renal cell carcinoma, mandibular condyle CBCT, thoraacoabdominal aortic dissection CT, abdominal aortic aneurysm CT. Various networks including 2D or 3D U-Net, Cascade 3D U-Net, UNETR, SwinUNETR, and nnU-Net were selectively used for AL in various tasks. The evaluation was performed using dice similarity coefficient (DSC) and Hausdorff distance (HD) to assess the agreement of areas

and distances at predefined stages, accuracy for the multi-classes to be segmented, time comparison for segmentation using manual segmentation and smart labeling, and stress tests to determine the optimal amount of data.

Secondly, using a 3D CAD tool based on a 3D model obtained through automated segmentation, patient-specific modeling or landmark measurement for diagnosis and lesion tracking can be performed. By using CAD systems, design modifications can be easily generated to improve accuracy in clinical applications, and they are optimized to meet specific requirements of clinicians. However, like manual segmentation, conventional modeling methods are time-consuming and require significant labor. An automated CAD modeling system using a script-based API provides excellent performance, accuracy, and efficiency in a short time, overcoming the limitations of conventional modeling methods. Automated CAD modeling typically involves setting inputs and parameters for 3D modeling, generating algorithm and programming code based on the specifications, and integrating the code with API of CAD software, enabling modeling and modification. In thoracoabdominal aortic dissection CT and abdominal aortic aneurysm CT, automated 3D CAD modeling and measurement were compared with conventional manual methods, and a series of processes required for automated modeling were optimized, modularized, and validated to perform design and measurement for patients with various anatomical structures. The evaluation involved analyzing the accuracy of 3D models and measurements obtained through conventional manual and automated CAD modeling, as well as the time required for modeling.

Finally, 3DP technology was found to have the advantage of addressing clinical unmet needs for pediatric cases, rare and complex conditions, and surgeries that are difficult to standardize, as most medical devices are commonly developed or customized for adult patients with common diseases. 3DP technologies proceed by adding materials layer-by-layer until the object is completely built. It can be classified into various methods depending on the materials used and the printing process. The 3D model obtained through automated segmentation and 3D CAD modeling is converted to standard tessellation language (STL) format and printed using the appropriate 3DP, followed by sterilization before clinical application. We introduce two new reconstruction techniques using patient-specific 3D-

printed graft reconstruction guides in open surgical repair of thoracoabdominal aortic dissection: (1) model-based technique (MBT) that presents the projected aortic graft, visualizing the main aortic body and its major branches and (2) guide-based technique (GBT) in which the branching vessels in the visualizing guide are replaced by marking points identifiable by tactile sense. The effectiveness was demonstrated by evaluating conventional and new techniques base on accuracy, marking time requirement, reproducibility, and results of survey to surgeons on the efficiency and efficacy. The accuracy of 3DP guides can be affected by various factors such as the external environment, duration of 3D printer, resolution, materials, shape of the 3D model, printing conditions, and post-processing, which may lead to discrepancies between the printed model and the original 3D model.

In conclusion, we have developed an automated workflow for the segmentation and modeling processes necessary for applying 3DP in the clinical application. This approach significantly reduces repetitive and labor-intensive tasks, maintains consistency through codification, and saves time, thereby alleviating their workflow and accelerating the application of 3DP compared to conventional methods. Furthermore, the clinical usefulness and efficiency of 3D printed patient-specific surgical guides demonstrated in addressing clinical unmet needs.

Key words: Automation, Segmentation, Active learning (AL), Computer aided design (CAD), application programming interfaces (API), 3D printing (3DP), Clinical application

## Contents

<b>Abstract</b> .....	<b>i</b>
<b>Contents</b> .....	<b>iv</b>
<b>List of Tables</b> .....	<b>vi</b>
<b>List of Figures</b> .....	<b>viii</b>
<b>List of Algorithm</b> .....	<b>xi</b>
<b>List of Abbreviations</b> .....	<b>xii</b>
<b>1 Introduction</b> .....	<b>1</b>
1.1 Motivations .....	5
1.2 Contributions.....	5
<b>2 Background</b> .....	<b>6</b>
2.1 Medical image segmentation using deep-learning.....	6
2.1.1 Convolution neural network (CNN) .....	6
2.1.2 Fully convolutional networks (FCN) .....	8
2.1.3 U-Net .....	8
2.1.4 Cascade U-Net.....	9
2.1.5 no-new-U-Net (nnU-Net) .....	10
2.1.6 UNet Transformers (UNETR).....	11
2.1.7 Shifted windows UNet Transformers (SwinUNETR) .....	12
2.1.8 Active learning (AL).....	13
2.2 Computer aided design (CAD) modeling .....	14
2.2.1 Manual 3D CAD modeling.....	14
2.2.2 Script-based application programming interface (API) .....	16
2.3 3D printing technologies with clinical application .....	18
2.3.1 Fused deposition modeling (FDM).....	18
2.3.2 Stereolithography apparatus (SLA) .....	18
2.3.3 Digital Light Processing (DLP) .....	19



2.3.4 Color-Jet printing (CJP).....	19
2.3.5 Multi-jet printing (MJP) .....	19
2.3.6 Photopolymer jetting (PolyJet) .....	20
2.3.7 Selective laser sintering (SLS).....	20
<b>3 Semi-automated and enhanced segmentation using semantic segmentation with active learning (AL) .....</b>	<b>21</b>
3.1 Kidney substructures with RCC in Kidney.....	21
3.2 Mandibular condyle in dental CBCT .....	32
3.3 Thoracoabdominal aortic dissection in CT angiography .....	43
3.4 Abdominal aortic aneurysm in abdominal CT .....	52
<b>4 Semi-automated design and measurement with application programming interface (API) of computer aided design (CAD).....</b>	<b>62</b>
4.1 Aortic graft reconstruction guides in thoracoabdominal aortic dissection.....	62
4.2 Landmark measurement in abdominal aortic aneurysm .....	73
<b>5 Utilization of patient-specific guides fabricated using 3D printing from viewpoint of clinical application .....</b>	<b>84</b>
5.1 3D printed surgical guides in thoracoabdominal aortic dissection .....	84
<b>6 Discussion .....</b>	<b>97</b>
<b>7 Conclusion .....</b>	<b>121</b>
<b>References.....</b>	<b>122</b>
<b>Abstract (In Korean).....</b>	<b>134</b>
<b>Acknowledgements.....</b>	<b>137</b>

## List of Tables

Table 3-1. Dice similarity coefficient for each stage of kidney with cascade 3D U-Net in kidney CT.	<b>30</b>
Table 3-2. Comparison of segmentation time for kidney between manual and AL-corrected segmentation in kidney CT. ....	<b>31</b>
Table 3-3. Root mean square (RMS) evaluation from 3D modeling for kidney. ....	<b>31</b>
Table 3-4. Dice similarity coefficient and Hausdorff distance for each stage of mandibular condyles with a basic 3D U-Net and cascade 3D U-Net in CBCT.....	<b>41</b>
Table 3-5. Segmentation time of mandibular condyles for manual, basic 3D U-Net, and cascade 3D U-Net in stage 5 of CBCT.....	<b>43</b>
Table 3-6. Dice similarity coefficient for abdominal aortic dissection with UNETR and SwinUNETR of MONAI and 2D U-Net, 3D U-Net, 2D-3D U-Net ensemble, and cascade 3D U-Net of nnU-Net. .	<b>50</b>
Table 3-7. 95% Hausdorff distance for thoracoabdominal aortic dissection with UNETR and SwinUNETR of MONAI and 2D U-Net, 3D U-Net, 2D-3D U-Net ensemble, and cascade 3D U-Net of nnU-Net. ....	<b>51</b>
Table 3-8. The segmentation time for manual and correction using SwinUNETR in thoracoabdominal aortic dissection. ....	<b>52</b>
Table 3-9. Dice similarity coefficient for abdominal aortic aneurysm with UNETR and SwinUNETR of MONAI and 2D U-Net, 3D U-Net, 2D-3D U-Net ensemble, and cascade 3D U-Net of nnU-Net. .	<b>59</b>
Table 3-10. 95% Hausdorff distance for abdominal aortic aneurysm with UNETR and SwinUNETR of MONAI and 2D U-Net, 3D U-Net, 2D-3D U-Net ensemble, and cascade 3D U-Net of nnU-Net.....	<b>60</b>
Table 3-11. The segmentation time for manual and correction using 3D U-Net of nnU-Net in abdominal aortic aneurysm. ....	<b>61</b>
Table 4-1. Ten patients' profiles for thoracoabdominal aortic dissection, including classification, level of segmental arteries, and range of graft reconstruction. ....	<b>64</b>
Table 4-2. Hausdorff average distance of corresponding points between conventional and automated modeling methods for each patient with visualizing and marking guides. ....	<b>71</b>
Table 4-3. Modeling time for conventional and automated modeling methods with two types of patient-specific graft reconstruction guides. ....	<b>73</b>
Table 4-4 Manufacturer's guideline of patient selection for EVAR [141]. ....	<b>74</b>

Table 4-5. The differences between manual and automatic measurements for the aortic neck diameter, aortic aneurysm, right iliac artery, left iliac artery diameter, aortic neck length, the tortuosity of right and left iliac artery including curve, line length, and ration between two lengths. ....	<b>80</b>
Table 5-1 Individual profiles of the subject patients including classification, level of segmental artery, and range of replacement. ....	<b>86</b>
Table 5-2. Measurements and time requirements of graft reconstruction using DGM, IBT, MBT, and GBT.....	<b>93</b>
Table 5-3. Correlation coefficient between DGM and three techniques for diagonal length, height, and angle.....	<b>95</b>
Table 5-4. Retrospective survey in relation to understanding, usefulness, satisfaction, surgical outcome, and recommendability for use in other applications for IBT without 3D printing technique and MBT and GBT with 3D printing technique. ....	<b>96</b>
Table 6-1. The summary of each task. ....	<b>99</b>
Table 6-2. Dice similarity coefficient for each institution with each stage of mandibular condyles with a basic 3D U-Net and cascade 3D U-Net in CBCT.....	<b>102</b>
Table 6-3. Intra- and inter-observer variation for 4 classes in abdominal aortic aneurysm. ....	<b>108</b>
Table 6-4. The best network for each stage and class in 4 studies. ....	<b>109</b>
Table 6-5. Comparison between 2D and 3D U-Net of nnU-Net in two aortic studies.....	<b>111</b>
Table 6-6. Comparison between high- and low-resolution with 6 networks in two aortic studies.....	<b>112</b>
Table 6-7. Hausdorff average distance of 5 patients for validation between conventional and automated modeling methods with visualizing and marking guides. ....	<b>114</b>
Table 6-8. Modeling time of 5 patients for validation with conventional and automated modeling methods consisted of two types of patient-specific graft reconstruction guides.....	<b>114</b>
Table 6-9. Comparison of correlation between 3 researchers for in the aortic neck diameter, aortic neck length, right and left tortuosity including curve length, line length, and ratio.....	<b>116</b>

## List of Figures

Figure 1-1. The overall procedure of 3DP technology for clinical application. ....	1
Figure 2-1. The convolution neural network (CNN) architecture. ....	6
Figure 2-2. The fully convolutional networks (FCN) architecture. ....	8
Figure 2-3. The U-Net architecture. ....	9
Figure 2-4. Cascade U-Net methods (A) The first training for the location of segmentation from CT images with basic U-Net, (B) The second training for the classes from the first training. ....	10
Figure 2-5. The UNet TRansformers (UNETR) architecture. ....	12
Figure 2-6. The Shifted windows UNet TRansformers (SwinUNETR) architecture. ....	13
Figure 2-7. The process of the active learning (AL). ....	14
Figure 2-8. The process of the application programming interface (API). ....	17
Figure 2-9. The principle and structure of 3D printing (3DP) technologies. (A) the fused deposition modeling (FDM) type, (B) the stereolithography apparatus (SLA) type, (C) the color-jet printing (CJP) type, (D) the multi-jet printing (MJP) type, (E) the photopolymer jetting (PolyJet) type, and (F) the selective laser sintering (SLS) type. ....	21
Figure 3-1. The overall procedure s of cascade 3D U-Net using active learning (AL) in kidney CT. ..	23
Figure 3-2. The manual segmentation techniques including (A) thresholding, (B) region growing, (C) dilation and erosion, and (D) edit mask. ....	24
Figure 3-3. Pre-processing procedure for kidneys with a 3D U-Net and cascade 3D U-Net (A) Normalization image, (B) Division by the right and left sides, (C) Flip the right images to horizontal, and (D) Crop image including the margin ....	26
Figure 3-4. Data distribution in each stage for active learning (AL) in kidney CT. ....	27
Figure 3-5. The architecture of (A) a basic 3D U-Net and (B) a cascaded 3D U-Net. ....	28
Figure 3-6. Root mean square (RMS) evaluation from 3D modeling about kidney with RCC. ....	32
Figure 3-7. The overall procedure s of a basic 3D U-Net and its based cascade 3D U-net using active learning (AL) in CBCT. ....	34
Figure 3-8. Pre-processing procedure for mandibular condyles with a basic 3D U-Net and cascade 3D U-Net (A) Normalization image, (B) Division by the right and left sides, (C) Flip the right images to horizontal, and (D) Crop image including the margin. ....	36
Figure 3-9. Data distribution for mandibular condyle in each stage for active learning (AL) ....	38

Figure 3-10 The architecture of (A) a basic 3D U-Net and (B) a cascaded 3D U-Net. ....	<b>39</b>
Figure 3-11. The difference map between ground truth and prediction in 3D U-Net and cascaded 3D U-Net. (A) The best case and (B) worst case of 3D U-net, and (C) the best case and (D) worst case of cascaded 3D U-Net. ....	<b>42</b>
Figure 3-12. (A) The octopod thoracoabdominal aortic aneurysm (TAAA) aortic graft. (B) Representative computed tomographic images at the visceral and intercostal level. (C) Intraoperative findings of the octopod TAAA graft [120]. ....	<b>44</b>
Figure 3-13. Overall flow of thoracoabdominal aortic dissection and abdominal aortic aneurysm for smart labeling with human in the loop in CT angiography. ....	<b>46</b>
Figure 3-14. Data distribution for thoracoabdominal aortic dissection in each stage for active learning (AL) .....	<b>49</b>
Figure 3-15. Data distribution in each stage for active learning (AL) for abdominal aortic aneurysm. ....	<b>56</b>
Figure 4-1. Overall procedure for the evaluation of two types of patient-specific graft reconstruction guides consisting of visualizing and marking guides for aortic dissection and comparison between conventional and automatic modeling methods. ....	<b>63</b>
Figure 4-2. The conventional modeling method for patient-specific visualizing and marking guides. (A) Automated segmentation of thoracoabdominal aorta, including major blood vessels in the CT angiography images. (B) The extracting center line of the native aorta (black line) and the smoothed center line of the main (green line) and vascular grafts (blue line). (C) Designing the main and vascular grafts. (D, left) Combination of the main and vascular grafts for the visualizing guide and (D, right) the protrusion toward the corresponding surfaces between the main and vascular grafts. (E) Creation of two virtual planes to determine the extent of the thoracoabdominal aortic dissection and trimming of the model. (F, left) Completion of visualizing and (F, right) marking guides. ....	<b>67</b>
Figure 4-3. Comparison of the aligned difference map is shown with the absolute mean differences in the areas between conventional and automated modeling methods with (A) visualizing and (B) marking guides. ....	<b>72</b>
Figure 4-4. The clinical defined measurement landmarks for AAA models. ....	<b>75</b>
Figure 4-5. Conventional image-based measurement. ....	<b>76</b>

Figure 4-6. Bland–Altman plot indicating the distribution of the differences between manual and automatic method, divided by (A) the aortic neck diameter and (B) the aortic aneurysm diameter. ....**81**

Figure 4-7. Bland–Altman plot indicating the distribution of the differences between manual and automatic method, divided by (A) the right iliac artery diameter, (B) the left iliac artery diameter, and (C) the aortic neck length.....**82**

Figure 4-8. Bland–Altman plot indicating the distribution of the differences between manual and automated method, divided by (I) the curve length, (J) the line length, and (K) the tortuosity ratio for left iliac artery. ....**82**

Figure 4-9. Bland–Altman plot indicating the distribution of the differences between manual and automatic method, divided by (A) the curve length, (B) the line length, and (C) the tortuosity ratio for left iliac artery. ....**83**

Figure 5-1. Overall process of graft reconstruction with the conventional IBT, MBT, and GBT. ....**85**

Figure 5-2. Two types of patient-specific graft reconstruction guide application for open repair of thoracoabdominal aortic dissection. (A) CT angiography images and segmentation of diseased aorta and spine. (B) The modeling the centreline of graft based on that of a native aorta. (C) 3D modeling of the visualizing and marking guides. (D) 3D-printed visualizing guide and marking guide; (E) graft reconstruction and clinical application in operating room. (F) The 3D model of postoperative graft. .**89**

Figure 5-3. Patient-specific graft reconstruction process with MBT and GBT in operating room. ....**90**

Figure 5-4. Guide to evaluating the accuracy of three techniques-IBT, MBT, and GBT; (A) Locating celiac artery and segmental arteries marked on graft. (b) Spreading the graft using scissors. (c) Measuring the length, height, and angle between celiac artery and segmental arteries. ....**92**

Figure 5-5. Bland–Altman plot indicating the distribution of the differences between DGM and IBT, divided by (A) diagonal line, (B) height and (C) angle; between the DGM and MBT, divided by (D) diagonal line, (E) height, (F) angle; and between the DGM and GBT, divided by (G) diagonal line, (H) height, and (I) angle. ....**94**

Figure 6-1. A case for cascaded 3D U-Net (A) images, (B) prediction, and (C) ground truth in kidney CT. ....**100**

Figure 6-2. The errors for prediction of cascade 3D U-net including (A) noise and (B) under segmentation. ....**103**

Figure 6-3. A case for SwinUNETR with CT images, prediction (SwinUNETR and 2D U-Net, and ground truth in thoracoabdominal aortic dissection. .... **105**

Figure 6-4 Best case for 3D U-Net with images, prediction (3D U-Net and UNETR), and ground truth. .... **107**

Figure 6-5. The subjective assessment and measurement error of elliptical aortic center and blood vessels in CT images. If a red line is selected instead of a green line, there is an error in angle measurement. .... **118**

Figure 6-6. Making time according to the number of segmental arteries for IBT, MBT and GBT. .... **119**

## **List of Algorithm**

Algorithm 4-1. Automated modeling method for the visualizing guide and marking guide.....	<b>69</b>
Algorithm 4-2. The module for part inspection. ....	<b>70</b>
Algorithm 4-3. The module for finding the maximum curve.....	<b>77</b>
Algorithm 4-4. The algorithms for the automatic measurement of the aortic neck diameter, aortic aneurysm diameter, the common iliac artery diameter, aortic neck length, the tortuosity of common iliac artery, and aortic neck angulation. ....	<b>78</b>



## List of Abbreviations

2D	2-Dimensional
3D	3-Dimensional
3DP	3D Printing
AAA	Abdominal Aortic Aneurysms
ABS	Acrylonitrile Butadiene Styrene
AL	Active learning
AMC	Asan Medical Center
API	Application Programming Interface
AR	Augmented Reality
CAD	Computer Aided Design
CBCT	Cone Beam CT
CJP	Color-Jet Printing
CNN	Convolution Neural Network
CT	Computed Tomography
DGM	Designed Graft Model
DICOM	Digital Imaging and COmmunications in Medicine
DLP	Digital Light Processing
DL	Deep learning
DSC	Dice Similarity Coefficient
EVAR	EndoVascular Aneurysm Repair
FCN	Fully Convolutional Networks
FDM	Fused Deposition Modeling
FOV	Field Of View
GBT	Guide-Based Technique
GPU	Graphics Processing Unit
HD	Hausdorff Distance
HIPS	High Impact PolyStyrene
HU	Hounsfield Units
IBT	Image-Based Technique

ICC	Intraclass Correlation Coefficients
KUMC	Korea University Medical Center
LoA	Limits of Agreement
MBT	Model-Based Technique
MJP	Multi-Jet Printing
MONAI	Medical Open Network for Artificial Intelligence
MR	Mixed Reality
MRI	Magnetic Resonance Imaging
nnU-Net	No-New-U-Net
PACS	Picture Archiving and Communication System
PLA	Polylactic Acid
PolyJet	Photopolymer Jetting
PVA	PolyVinyl Alcohol
RCC	Renal Cell Carcinoma
RMS	Root Mean Square
ROI	Region Of Interest
RP	Rapid Prototyping
SD	Standard Deviation
SLA	Stereolithography Apparatus
SLS	Selective Laser Sintering
STL	STereoLithography
SwinUNETR	Shifted windows UNet Transformers
TMJ	TemporoMandibular Joint
TPU	Thermoplastic PolyUrethane
UENTR	UNet Transformers
US	Ultrasound
UV	UltraViolet
VR	Virtual Reality

# 1 Introduction

To apply 3D printing (3DP) technology to the medical field, it is essential to go through the process of medical image acquisition, image segmentation, 3D computer-aided design (CAD) modeling, 3DP, and post-processing (Figure 1-1). Medical image data is acquired by imaging devices such as computed tomography (CT), magnetic resonance imaging (MRI), and ultrasound (US) images. Important factors such as contrast or signal-to-noise ratio, spatial resolution, and image thickness should be considered during image acquisition since the quality of the image can affect the feasibility of 3DP. The next step is to segment the region of interest (ROI) such as organs or lesions from the acquired data. 3D models are generated using surface rendering techniques, and CAD modeling is performed to design a model suitable for the intended use, such as guides, simulators, educational phantoms, and molds. The objects are checked for suitability for 3DP, and then the data is exported in 3D file formats such as stereolithography (STL) format. After selecting an appropriate 3DP technology and performing post-processing steps such as support removal, the 3DP objects are sterilized for clinical application. Finally, the 3D objects are applied clinically in the operating room [1, 2]. There are currently various 3DP technologies available for research, development, and commercial applications. These technologies can be classified into different types, including fused deposition modeling (FDM), SLA, digital light processing (DLP), color-jet printing (CJP), multi-jet printing (MJP), photopolymer jetting (PolyJet), selective laser sintering (SLS).

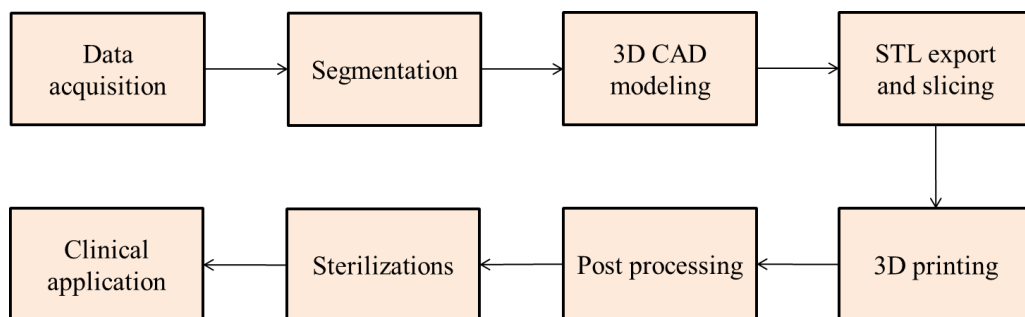


Figure 1-1. The overall procedure of 3DP technology for clinical application.

Medical image segmentation is essential for obtaining non-invasive information about the structures within the human body, allowing radiologists and physicians to study and visualize anatomy, simulate biological processes, localize pathologies, track disease progression, and determine the necessity of radiotherapy or surgeries with CT, MRI, and US images [3-5]. The ability to accurately segment medical images is critical for providing a better understanding of the human body and its functions, aiding in the diagnosis and treatment of various medical conditions [6, 7]. The accuracy of segmentation is crucial for the functionality of computer-aided diagnosis systems, as it directly affects the system's ability to provide accurate diagnoses and treatment plans. Therefore, segmentation plays a vital role in medical imaging, and its importance cannot be overstated [8-10]. The traditional segmentation techniques have relied on manually crafted methods that are dependent on the expertise of the clinician. This often involves the use of segmentation tools such as thresholding, region growing, morphology operations, and brushes to explicitly define the ground truth on a per-pixel basis. Despite advancements in semi-automated segmentation methods, manual segmentation remains a standard practice in many imaging applications [11, 12]. The image segmentation methods are classified as follows: 1) The image-based segmentation, 2) subjective surface segmentation, and 3) atlas-based segmentation method. Image-based segmentation methods use templates that are adjusted to fit the image data while minimizing integration errors. These methods often use control points to parameterize the shape of the template for a given structure, and the whole shape is transformed to match the new image. Active shape models and active appearance models are two common shape-based techniques used in image segmentation [13, 14]. The subjective surface segmentation method uses advection-diffusion models to control segmentation functions for object segmentation. A segmentation seed is required to configure the initial segmentation function, and its position determines the function's shape. In some applications, clinical experts can manually label multiple images, and the invisible image can be segmented by extrapolating from the labeled training image [15, 16]. The atlas-based segmentation method combines multiple training images into a single atlas image or uses them individually [17-19]. Image registration is used to align the atlas or training image to a new image for segmentation. Parametric atlas methods combine training images into one atlas image, while nonparametric

methods use individual training images. However, accurate segmentation of medical images faces many challenges [20]. Medical image segmentation is a challenging task due to factors such as low contrast, noise, inhomogeneity of anatomical structures, and similar visual appearances of tissues and vessels. The 3D and 4D images also present additional challenges such as variability in object-of-interest shapes and textures over time [21-23]. As a result, conventional segmentation techniques may not work well for all subjects or images. Various segmentation techniques such as contour-, region-, and pixel/voxel-based approaches aim to obtain boundaries, connected regions, or perform classification at the pixel/voxel level, respectively [24].

In recent years, deep learning (DL) model such as fully convolutional networks (FCN) have made significant progress in segmentation tasks, particularly in medical image segmentation [25]. The U-Net architecture has been found to be effective in this domain, leading to improved accuracy and robustness in medical image segmentation for various anatomical structures and diseases. As a result, these advancements in DL have had a significant impact on medical image segmentation, allowing for more precise and reliable segmentation for different anatomical structures and diseases [7, 26-28]. The limited availability of medical image datasets and the high costs and efforts involved in expert labeling pose serious challenges to DL methods in medical image segmentation. DL architectures require large amounts of data to avoid overfitting, which can be difficult to obtain in real-world medical imaging. Rare diseases and complex anatomical structures present additional difficulties in image segmentation due to their high variability.

Active learning (AL) framework were developed to enhance segmentation using a smart labeling method, which efficiently increases labeled data by training on a small initial dataset with manually labeled data and correcting the predicted new data with human experts. The goal is to make the labeling process more efficient by focusing on the most important samples [29-35].

In the medical field, it is important to have an efficient CAD system that can design the patient-specific surgical guides, simulators, education phantoms, and biological applications [36-41]. The CAD system would be utilized in multiple technologies, including 3DP, augmented reality (AR), virtual reality (VR), mixed reality (MR), and medical robotics [1,

42-50]. An efficient CAD system offers several advantages, such as reducing lead time and enhancing productivity and quality. CAD allows for easy modifications to designs to improve accuracy in clinical situations. A database can be used to manage different patient-specific models, which can improve communication between designers. The modeling facilities in the CAD system are tailored to meet the specific needs of clinicians. However, finding CAD software that meets all the demands of the medical field can be challenging [51, 52]. CAD systems with many parameters and high memory requirements need more processing time and hardware. Mistakes in input data could lead to harmful outcomes [53]. Moreover, the conventional modeling process is laborious, time-consuming, and monotonous [52-54]. To address these challenges, an automated CAD modeling system has been developed that can achieve greater accuracy, improved performance, and shorter modeling times compared to the traditional approach. Furthermore, this CAD system can be utilized with minimal human intervention.

The 3DP technology was initially developed by Charles W. Hull in August 1984, using the Stereolithography apparatus (SLA), and was patented [55]. Over the course of 30 years following the patent application, Hull's mechanical process of fabricating objects from CAD models has been applied to numerous business fields, and has continued to be actively developed in various areas since the patent expired in 2014 [56]. The 3DP technology, known as rapid prototyping or additive manufacturing, proceed by adding materials layer-by-layer until the object is completely built. The 3DP is distinct from the computerized numerical control process of subtractive manufacturing [57]. Recently, 3DP has had an impact on various fields such as medicine, machinery, architecture, fashion, and education. In the medicine, the acquisition of digital imaging and communications in medicine (DICOM) based on CT, MRI, and US has led to extensive research and development in various areas such as patient-specific guides, simulators, transplant prostheses, surgical tools, and education for diverse fields including the aorta, kidneys, heart, lungs, liver, prostate, and teeth [2, 57-61].

## **1.1 Motivations**

In the medical field, 3DP technology is rapidly utilized for patient-specific guides, simulators, surgical planning, and education phantoms, and implants. To apply 3DP in the medical field, essential tasks such as medical image acquisition, segmentation, 3D modeling and design, and measurement must be performed. However, these repetitive manual tasks are tedious, labor-intensive, time-consuming and lack of consistency for workers. These challenges can be solved by introducing automated workflow with deep learning technology in segmentation and application programming interface (API) in CAD modeling. The advantages of automated workflows include the reduction of repetitive tasks, which are often tedious, labor-intensive, and time-consuming. These automated workflows ensure consistency between tasks and researchers, promoting standardized practices. Moreover, it easily apply to various clinical field. The objectives of this study divided into three sections: Firstly, the development of an automated and enhanced segmentation algorithm using AL techniques to reduce labeling effort. Secondly, the development of automation for the design of patient-specific guides based on the 3D model acquired from automated segmentation, as well as automated measurement of clinically defined landmarks to predict complications. Lastly, the usefulness and efficiency of patient-specific surgical guides produced using 3DP technology were demonstrated with clinical application.

## **1.2 Contributions**

The main contribution of this study is the development of a semi-automated workflow from medical image acquisition to 3DP. Firstly, DL-based automated segmentation is developed using various networks for kidney with renal cell carcinoma (RCC), mandibular condyle, thoracoabdominal aortic dissection, and abdominal aortic aneurysm. In addition, AL techniques with smart labeling are employed to reduce labeling effort by dividing the limited dataset into multiple stages and evaluating the accuracy between the ground truth and predicted segmentation to determine an optimized dataset for training. The second contribution of this research is the development of a semi-automated CAD modeling and

measurement method based on 3D model for thoracoabdominal dissection and abdominal aortic aneurysm. The process involves designing patient-specific guides and modularizing a series of steps for design with optimization and measuring clinically defined specific landmarks that can be applied to all patients. Lastly, the contribution of this study is to develop patient-specific surgical guides for thoracoabdominal aortic dissection using various 3DP techniques, and to evaluate their accuracy and effectiveness through clinical application.

## 2 Background

### 2.1 Medical image segmentation using deep-learning

#### 2.1.1 Convolution neural network (CNN)

Artificial neural networks known as CNN have proven to be a powerful tool in detecting, classifying, segmenting, reconstructing, and performing natural language processing on medical image structures. CNN works by extracting and processing features from input data to identify patterns and objects in medical images [62-68]. The architecture of a CNN consists of convolution layers, pooling layers, and fully connected layers, with multiple convolution and pooling layers stacked repetitively, and one or more fully connected layers (Figure 2-1).

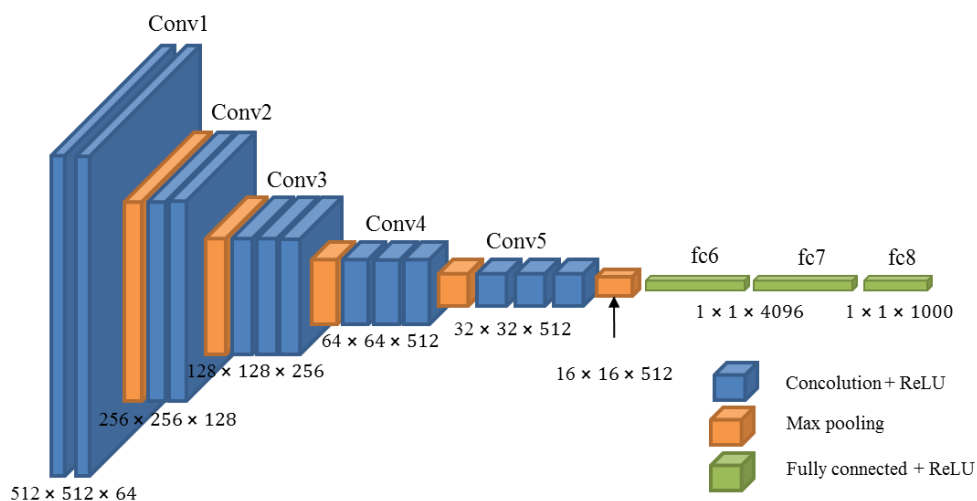


Figure 2-1. The convolution neural network (CNN) architecture.



The convolutional layer plays a crucial role in identifying and extracting features from input images. It comprises a group of filters, also known as kernels, that move across the input data and perform element-wise multiplication, followed by summation to produce a feature map. The convolution operation involves moving a filter across the input data, multiplying the filter values with the corresponding pixel values at each location, and adding up the results to produce a single value in the output feature map. The convolution operation is performed at every possible location of the filter over the input data, resulting in a complete feature map being generated. The receptive field or size of the filter determines the range of the convolution operation. If the filter size is larger, it will capture more global features, whereas a smaller filter will capture more local features. The stride of convolution determines the spacing between two consecutive locations of the filter. If the stride is larger, the output feature map size will be reduced, while a smaller stride will result in an increased output feature map size. Convolutional layers usually consist of multiple filters, each with its own set of weights, enabling the layer to learn multiple feature maps concurrently. After the convolutional layer generates multiple feature maps, they are sent to the next layer for additional processing. The pooling layer is employed to the downsampling that decrease the dimensionality of these feature maps produced by the convolutional layer. By reducing the size of the feature maps based on the window size and stride, the pooling layer produces smaller feature maps with fewer parameters. Using the pooling layer helps prevent overfitting and reduce computational complexity, while still retaining the significant features learned by the convolutional layer. There are two frequently used pooling layers in CNNs: max pooling and average pooling. Max pooling chooses the maximum value from a rectangular window within the feature map, and the resulting value is used as the output. In contrast, average pooling calculates the average value from a rectangular window within the feature map and uses it as the output. In CNN architectures, the fully connected layer is often positioned at the end of the network, following the convolutional and pooling layers. Its purpose is to map the extracted features to the final output classes. The fully connected layer is fed with the flattened output from the previous layer, which is a one-dimensional vector, and performs a matrix multiplication operation using a weight matrix and bias vector. This operation generates a new set of features that are used to map the extracted features to the

final output classes.

### 2.1.2 Fully convolutional networks (FCN)

The FCN is a deep neural network architecture that is tailored for image segmentation purposes. It works by substituting fully connected layers with convolutional layers, which allows the network to handle input images of variable sizes [25]. The FCN architecture usually consists of two primary parts: an encoder and a decoder. The encoder component of the FCN architecture is composed of convolutional and pooling layers, which are responsible for extracting crucial features from the input image. On the other hand, the decoder component consists of deconvolutional layers that perform upsampling of the feature maps to their original size, thereby generating the segmentation map. The FCN architecture introduces a significant advancement through the use of skip connections. These connections allow the network to combine feature maps from various layers and provide the decoder with access to low-level features from the encoder. This technique is instrumental in preserving detailed spatial information and generating precise segmentation maps (Figure 2-2).

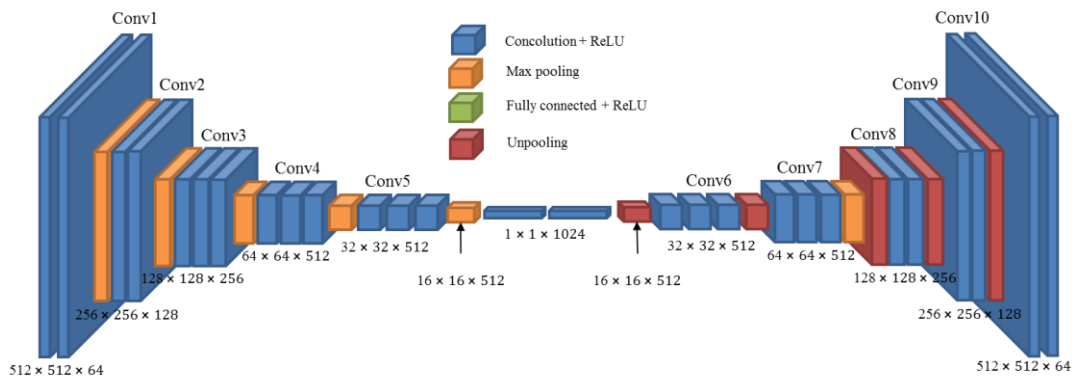


Figure 2-2. The fully convolutional networks (FCN) architecture.

### 2.1.3 U-Net

U-Net is a commonly used variation of the FCN that is tailored for biomedical image segmentation. Its design revolves around an encoder-decoder architecture that utilizes skip connections to enhance its performance [69-71]. U-Net is composed of an encoder that

reduces the spatial resolution of the input image and a decoder that increases the resolution of the output segmentation map. The encoder is a conventional CNN that comprises multiple convolutional and pooling layers. In contrast, the decoder consists of a sequence of deconvolutional layers that upsample the feature maps to match the original input size. Apart from the conventional encoder-decoder architecture, U-Net employs skip connections that link matching encoder and decoder layers. By enabling the decoder to utilize the high-resolution feature maps generated by the encoder, these connections preserve fine spatial details and enhance the precision of segmentation outcomes (Figure 2-3).

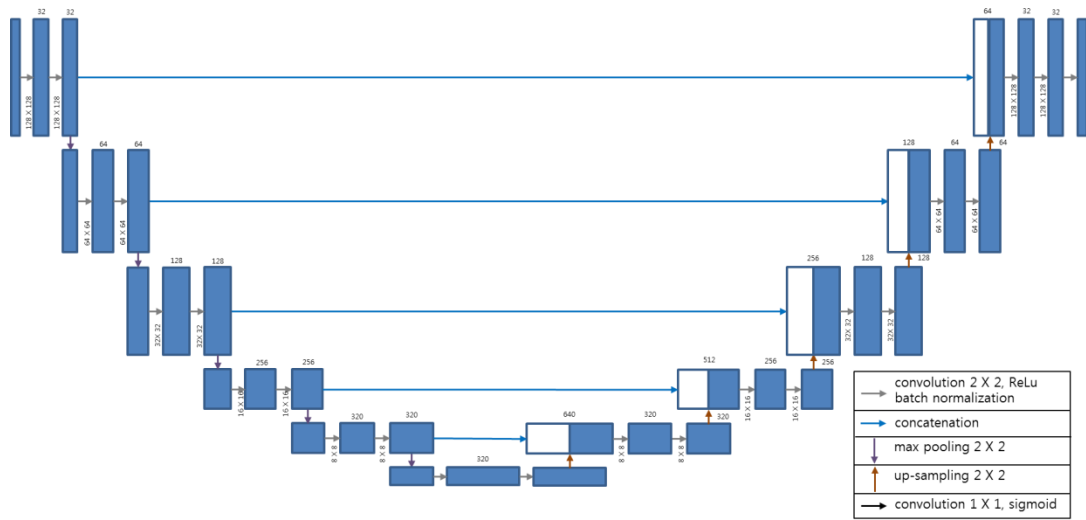


Figure 2-3. The U-Net architecture.

#### 2.1.4 Cascade U-Net

The cascade U-Net is an enhanced version of the U-Net architecture that aims to improve the reliability and precision of medical image segmentation [72-74]. It operates on a two-stage segmentation strategy that involves two separate U-Net networks, trained in sequence. The cascade U-Net approach involves two stages of segmentation, with the first stage generating a preliminary segmentation using a basic U-Net architecture. The initial segmentation is then fed into a modified U-Net architecture in the second stage. The modified U-Net architecture utilized in the cascade U-Net strategy contains supplementary skip connections that link the corresponding layers in the two U-Net networks. By

incorporating these skip connections, the second network in the cascade U-Net architecture is able to access and make use of both low- and high-level features extracted by the first network (Figure 2-4).

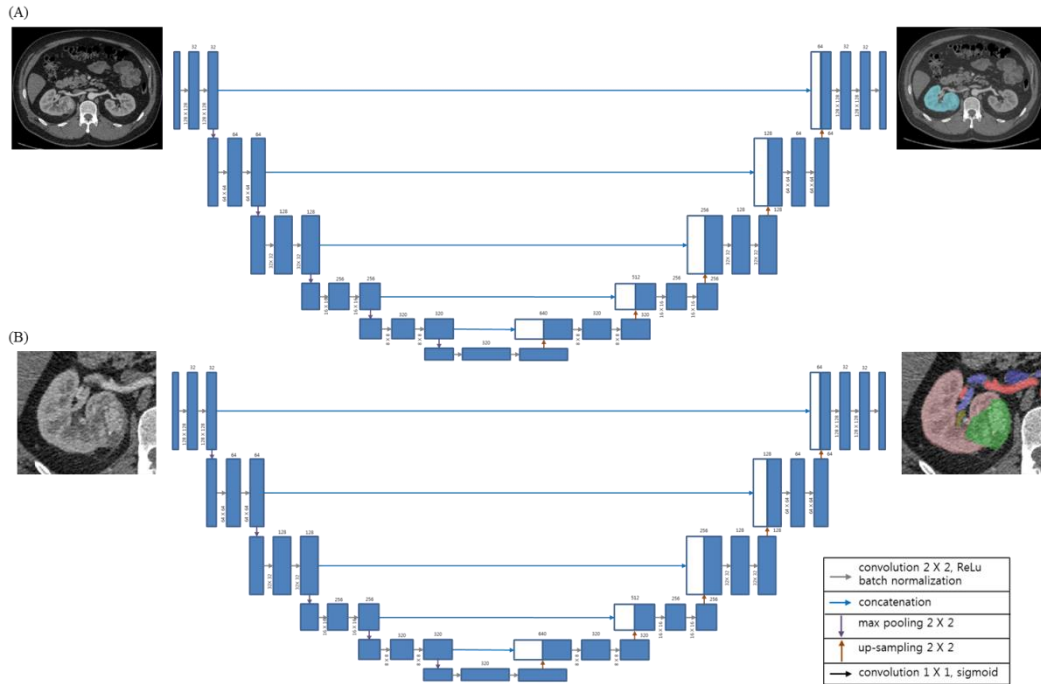


Figure 2-4. Cascade U-Net methods (A) The first training for the location of segmentation from CT images with basic U-Net, (B) The second training for the classes from the first training.

### 2.1.5 no-new-U-Net (nnU-Net)

Due to the 3D nature of medical images, a group of fundamental U-Net architectures are typically utilized, such as a 2D (2-Dimensional) U-Net, a 3D U-Net, a 2D-3D U-Net ensemble, and a cascade 3D U-Net [75]. The nnU-Net is designed to automatically optimize the hyperparameters of the U-Net architecture to achieve the best possible performance for a given medical image segmentation task. This self-adapting framework is based on the principle of automatically tuning the architecture to optimize performance. The nnU-Net employs a modified version of the U-Net architecture that incorporates various additional features to enhance its performance. These features include instance normalization, residual

connections, and convolutional layers with varying dilation rates, among others. The nnU-Net utilizes the foreground as a novel data preprocessing technique. It crops input images to different sizes and then pads them to a uniform size before inputting them into the network. The nnU-Net framework enhances the accuracy and robustness of the segmentation outcomes, particularly when the input images have diverse sizes and aspect ratios. The self-adapting framework of the nnU-Net is achieved via nested cross-validation loops that train and evaluate the network on various subsets of the training data. The iterative approach of nnU-Net optimizes hyperparameters like learning rate, number of filters, and dropout rate automatically by adapting the network to the specific segmentation task. This eliminates the need for manual parameter selection or tuning and leads to improved accuracy and robustness of the segmentation results.

#### 2.1.6 UNet Transformers (UNETR)

The UNETR is a medical image segmentation architecture developed by the medical open network for artificial intelligence (MONAI) framework that utilizes transformers to process and analyze medical image data [76-78]. The UNETR is based on combining the U-Net architecture with the transformer model, a self-attention mechanism. The UNETR architecture comprises two essential components: the encoder and the decoder. The encoder is a transformer model that is modified to extract high-level features from the input image through a series of self-attention layers. The decoder is a U-Net architecture that uses the features extracted by the encoder to produce the segmentation map (Figure 2-5). Compared to traditional U-Net-based segmentation models, the UNETR architecture offers a number of advantages. One key advantage is the use of self-attention mechanism in the transformer model, which enables the network to better capture long-range dependencies in the input image. This is especially important in medical images with complex structures and textures. In addition, the UNETR architecture can be trained end-to-end using standard backpropagation techniques, which makes the training process more efficient and enables better optimization of the network. In summary, the UNETR architecture is a flexible and robust solution for medical image segmentation that leverages the advantages of both U-Net

and transformer models. The MONAI framework offers a convenient platform for developing and deploying DL models in medical image analysis.

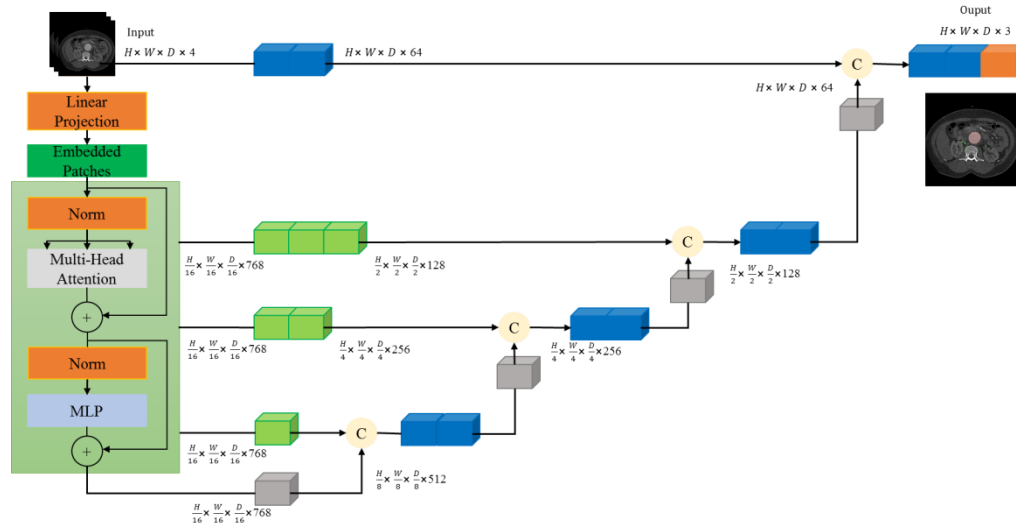


Figure 2-5. The UNet TRansformers (UNETR) architecture.

### 2.1.7 Shifted windows UNet TRansformers (SwinUNETR)

The SwinUNETR is a modified version of the UNETR architecture that has been created specifically for medical image segmentation by the MONAI framework [77-80]. The SwinUNETR is built on the combination of two architecture types: the Swin Transformer, which is a hierarchical transformer-based approach that uses self-attention layers to extract features from input images at different scales, and the U-Net architecture, which is used for medical image segmentation. The Swin Transformer divides the input image into patches and applies multiple self-attention layers to extract features at different scales. The SwinUNETR comprises two primary components, namely the encoder and decoder. The encoder component utilizes the Swin Transformer to extract high-level features from the input image via several self-attention layers. The decoder component utilizes the U-Net architecture and utilizes the features obtained by the encoder to generate the segmentation map (Figure 2-6). Compared to traditional U-net-based segmentation models, the SwinUNETR architecture has several advantages. One such benefit is the Swin Transformer's hierarchical structure, which

enables the network to capture both local and global features in medical images with complex structures and textures. In addition, the Swin Transformer is more efficient to implement and easier to train and deploy than traditional transformers. Overall, the SwinUNETR architecture is a powerful and efficient approach to medical image segmentation that combines the strengths of both the Swin Transformer and U-Net architectures. The MONAI framework is used to implement the SwinUNETR model and provides a user-friendly interface for training and deploying DL models in medical image analysis.

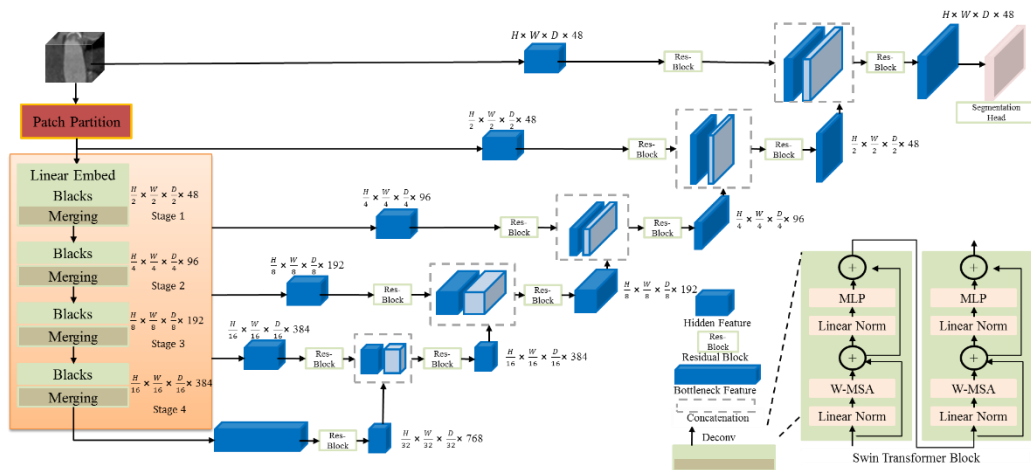


Figure 2-6. The Shifted windows UNet TRansformers (SwinUNETR) architecture.

### 2.1.8 Active learning (AL)

Training DL architectures typically requires a large amount of input data to prevent overfitting. However, medical images are often limited in number, and their annotation requires specialized medical expertise. Labeling images for rare diseases and complex structures is particularly challenging due to high anatomical variability. To address this issue and increase the efficiency of the learning process, several studies have introduced AL frameworks, which reduce the burden of manual annotation [29-35, 81]. The procedure for AL is depicted in Figure 2-7. The entire dataset is divided into N stages, and the initial labeling and training processes are conducted. If there are additional stages, inference is

performed on the unlabeled images, and the human-in-the-loop process is initiated, involving re-labeling and re-training by the annotators. Once labeling is completed for all stages, evaluation is conducted as the final step.

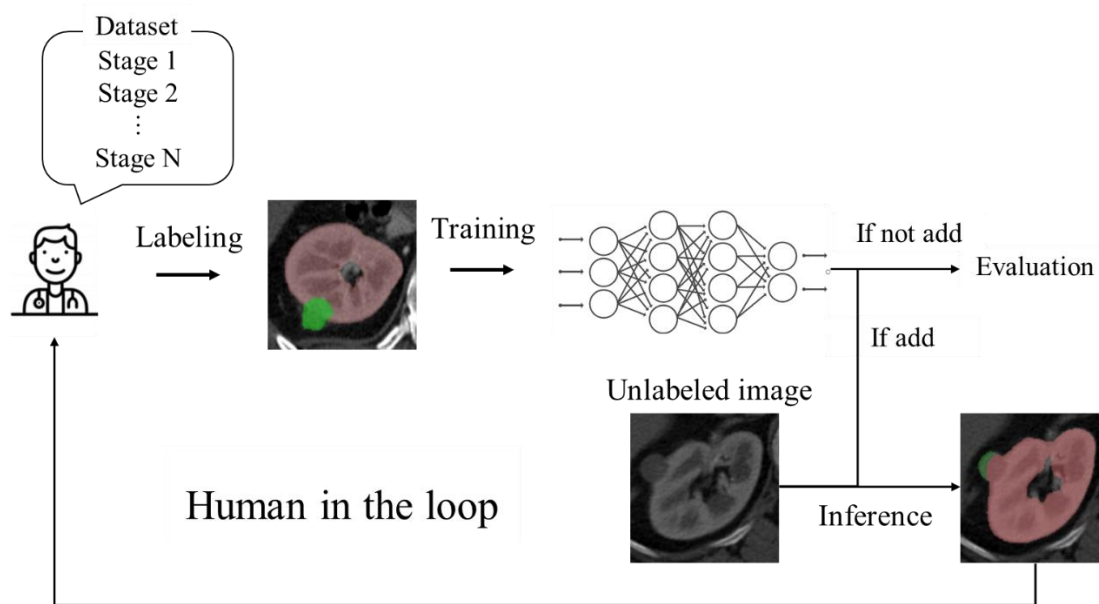


Figure 2-7. The process of the active learning (AL).

## 2.2 Computer aided design (CAD) modeling

### 2.2.1 Manual 3D CAD modeling

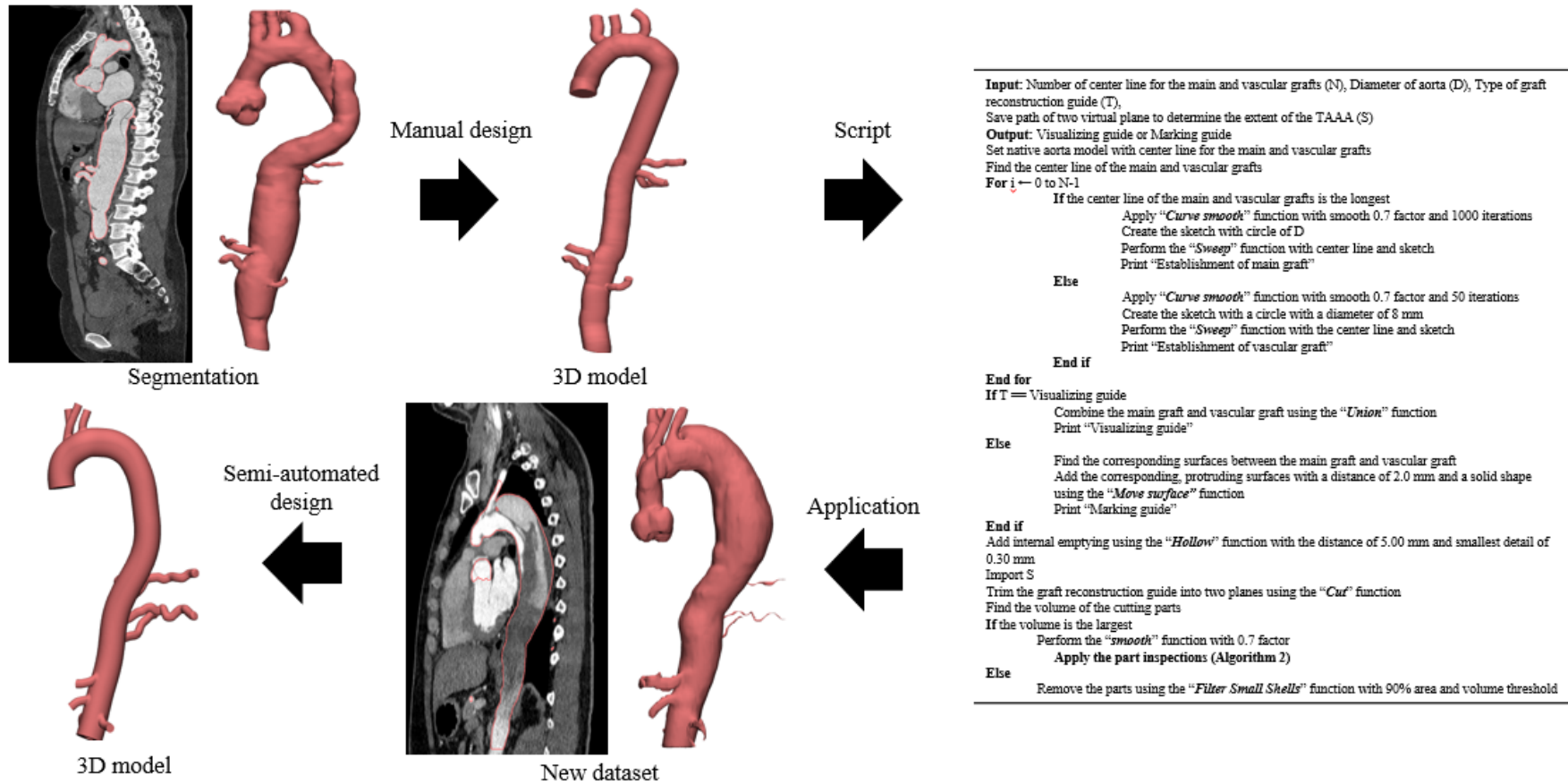
In the medical field, an efficient CAD system is required for various applications, such as modeling patient-specific surgical guides, education phantoms, simulators, and biology applications [36, 38-41, 82, 83]. These designs incorporate a range of manufacturing and visualization processes, such as additive and subtractive manufacturing, VR, AR, MR, and medical robotics. The combination of these techniques has enabled the development of advanced medical applications with enhanced precision and efficiency [1, 42, 44, 46-50]. Efficient CAD offers several benefits, including reduced lead time, increased productivity, and quality. CAD allows for easy modification of designs, which can lead to improved accuracy in clinical situations. Furthermore, a database of patient-specific models can



facilitate communication between designers and improve overall design quality. CAD systems in the medical field offer modeling capabilities that are tailored to meet the specific needs of clinicians. However, it can be challenging to find CAD software that fulfills all the requirements for medical applications [51, 52]. CAD modeling can be divided into two methods: 1) parametric modeling and 2) direct modeling. Parametric modeling is a technique used in 3D CAD modeling that employs parameters like dimensions, constraints, and relationships to define the geometry of the model. It offers precise control over the model's geometry and facilitates modifications by simply changing the parameters. The method is typically utilized in designing intricate objects and assemblies. Changes made to one part of the model automatically affect other dependent parts, enabling easy modifications without starting from scratch. In contrast, direct modeling is a more intuitive approach where the designer manipulates the model's geometry directly, without using parameters. This approach offers more creativity and flexibility in design as the designer can modify the model quickly and easily without constraints [84, 85]. Direct modeling is a method of 3D CAD modeling that does not rely on parameters to define the geometry of the model. Instead, the designer manipulates the model's geometry directly, giving them greater freedom and flexibility to make changes quickly and easily. This approach allows for more creative and intuitive design and avoids the constraints imposed by predefined parameters. Direct modeling is a suitable approach for generating initial design concepts and creating organic shapes. This method is particularly beneficial when dealing with irregular geometries, as it enables designers to produce intricate shapes quickly and efficiently [86-88]. CAD systems that have numerous parameters and require high memory consume more hardware resources and time to process data, and incorrect input data may lead to erroneous outputs. Furthermore, the traditional modeling approach is not only tedious and time-consuming but also demands a significant amount of labor [52-54]. An automated CAD modeling system has been developed to address the limitations of traditional modeling methods, providing superior performance, accuracy, and efficiency in less time. This system can be used with minimal human involvement.

### 2.2.2 Script-based application programming interface (API)

Automated 3D CAD modeling is the process of using algorithms and programming to automatically generate 3D CAD models, which is facilitated through API provided by CAD software. These APIs give developers the ability to access and manipulate CAD software programmatically, which allows them to automatically create and modify 3D models. There are various CAD software that support APIs using scripting languages, for instance, AutoCAD has AUTOLISP, Unigraphics has GRIP, Rhinocero has Rhino script, Maya uses MEL, 3D Max has MaxScript, and Materialize has 3-matic and magics script based on Python [51, 53, 54]. The process of semi-automated 3D CAD modeling and measurements using an API is illustrated in Figure 2-8. Utilizing segmentation and 3D models generated from medical images, manual modeling and measurements are performed. A series of steps and parameters for modeling and measurements are scripted to enable automated modeling and measurements when new patient data is received. Using APIs for automated 3D CAD modeling can offer various advantages, such as improved productivity, minimized mistakes, and accelerated design cycles. It also allows designers and engineers to swiftly and effortlessly experiment with different design possibilities and concepts.



1  
2  
3

Figure 2-8. The process of the application programming interface (API).

## **2.3 3D printing technologies with clinical application**

### **2.3.1 Fused deposition modeling (FDM)**

FDM is the most widely known and commonly used 3DP technology, which involves using filaments created from various materials such as polylactic acid (PLA), acrylonitrile butadiene styrene (ABS), thermoplastic polyurethane (TPU), Polyvinyl Alcohol (PVA), High Impact Polystyrene (HIPS). The process involves melting the filament using an extruder and stacking it layer by layer onto a plate. In the FDM process, a heat-sensitive filament is inserted into the extruder, where it is heated and then extruded through a nozzle via a stepper motor while the extruder moves in the x-y plane to create the desired objects. Once a layer is complete, the plate moves down along the z-axis, and the process is repeated for each subsequent layer (Figure 2-9 (A)). Post-processing typically involves removing supports using simple tools or dissolving them in water or a solvent, depending on the material used, such as PVA or HIPS. In addition, surface treatment with acetone may be performed on materials such as ABS as needed [89-91].

### **2.3.2 Stereolithography apparatus (SLA)**

SLA is the longest-standing and one of the most popular 3DP techniques, which uses photopolymerizable resins of the polymer family. The apparatus consists of a reservoir to contain the resin, an ultraviolet (UV) laser, and a build plate. The printing process of SLA involves reflecting an ultraviolet laser beam off mirrors to expose the resin on the build plate layer by layer as the mirrors move along the x-y plane. The height of the build plate is adjusted to stack each layer along the z-axis (Figure 2-9 (B)). Post-processing typically involves removing support structures and a raft from the model, washing it with isopropyl alcohol to remove excess resin, and conducting additional curing to increase its strength [91-93].

### 2.3.3 Digital Light Processing (DLP)

DLP is a type of 3DP that shares many similarities with SLA. Both use photopolymerizable resins and consist of a resin tank, projector, and build plate. However, DLP printing exposes the resin to 2D images projected onto the build plate, in contrast to SLA's point-based laser exposure. The post-processing steps for DLP are similar to SLA, involving removal of supports and rafts, cleaning the resin, and performing additional curing [91, 94].

### 2.3.4 Color-Jet printing (CJP)

CJP is used to a combination of gypsum powder and a binding agent to fabricate 3D objects, and to enhance the 3D printed objects strength during post-processing, color bonding is employed. The CJP is made up of a powder chamber, build chamber, rollers, and a binder head. In the CJP process, a layer of powder from the powder chamber is spread onto the build chamber using rollers, after which the binder is sprayed onto the powder layer based on the model shape. The tray in the powder chamber moves up one layer, while the tray in the build chamber moves down one layer. This process is repeated by spreading another layer of powder using rollers and repeating the previous steps to continue building the model (Figure 2-9 (C)). To post-process CJP, the support powder material is removed and recycled by vacuuming it back into the powder chamber. The 3D printed objects are strengthened with color bonding. A significant benefit of using the CJP method is that the powder is utilized as a support material, eliminating any visible signs of support marks on the final objects [95].

### 2.3.5 Multi-jet printing (MJP)

The MJP technique utilizes photopolymer resins that are acrylic-based and wax, and is composed of a plate for layering, a print head, and a UV lamp used for curing the material. During 3DP, the print head moves back and forth in the x-y plane, dispensing the material while it is simultaneously cured using the UV lamp. The plate is then moved in the z-axis to

layer the cured material and continue the printing process (Figure 2-9 (D)). The post-processing method for MJP involves heating water to around 70°C and keeping the printed parts in it for about 15-20 minutes to remove the wax used as support material. The heating time may vary depending on the size of the printed parts [95, 96].

### 2.3.6 Photopolymer jetting (PolyJet)

The PolyJet method shares many similarities with the MJP method in terms of its composition and 3DP process. However, unlike MJP, PolyJet can spray multiple materials, including base and binding materials, simultaneously, which enables a broader range of material options and more precise printing (Figure 2-9 (E)). Furthermore, the post-processing method for PolyJet is simpler and less time-consuming than MJP, as it involves using waterjet to remove support material, resulting in zero support marks on the printed parts[91, 97].

### 2.3.7 Selective laser sintering (SLS)

SLS method is similar to CJP in its composition, using metal and ceramic powders, and consisting of a powder chamber, build chamber, roller, and laser head. The printing process is almost identical to CJP, except that a CO<sub>2</sub> laser is used in the laser head to bond the metal and ceramic powders instead of spraying a binder (Figure 2-9 (F)). The post-processing involves removing the powder used as support material and performing surface treatment using tools like a sand blaster [98, 99].

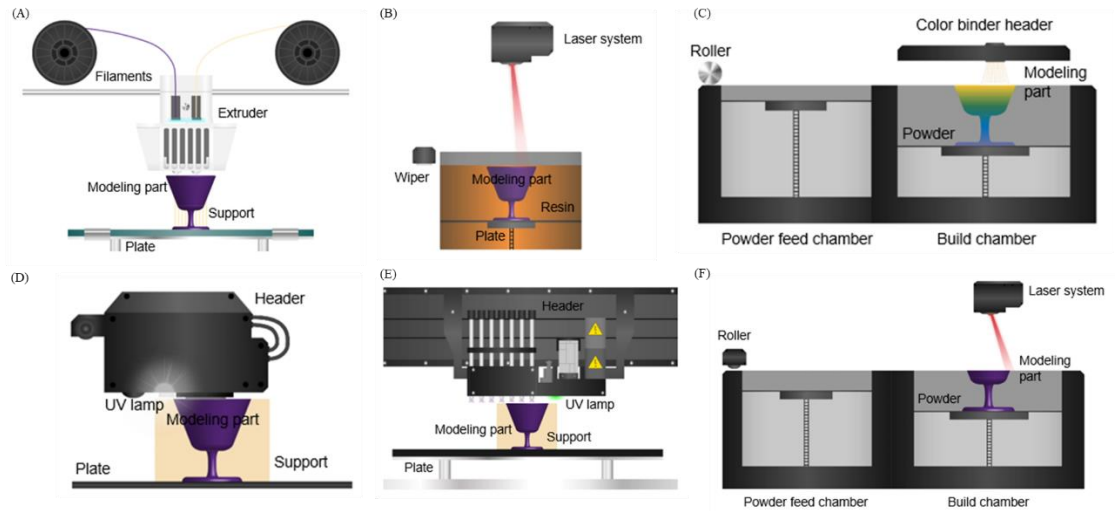


Figure 2-9. The principle and structure of 3D printing (3DP) technologies. (A) the fused deposition modeling (FDM) type, (B) the stereolithography apparatus (SLA) type, (C) the color-jet printing (CJP) type, (D) the multi-jet printing (MJP) type, (E) the photopolymer jetting (PolyJet) type, and (F) the selective laser sintering (SLS) type.

### 3 Semi-automated and enhanced segmentation using semantic segmentation with active learning (AL)

#### 3.1 Kidney substructures with RCC in Kidney

RCC is a common type of kidney cancer that affects many people in the United States, causing thousands of deaths each year. RCC often goes undetected because it rarely causes symptoms and is usually discovered by chance during CT scans done for other reasons. The size, location, and depth of kidney tumors can vary widely, and researchers are interested in studying the results of partial or radical nephrectomy (surgical removal of part or all of the kidney) in relation to the tumor's morphology. Accurate segmentation of kidney tumors in medical imaging is crucial for reliable disease classification and effective treatment planning. Partial nephrectomy, a surgical procedure that removes only part of the kidney, has been shown to be as effective as radical nephrectomy in terms of cancer control, while also preserving renal function. In fact, recent studies have found that partial nephrectomy may result in better outcomes in terms of both survival and morbidity, and as a result, there is a

growing trend towards its use, even in more complex surgical cases [100]. The partial nephrectomy procedure involves the use of vascular clamps on the renal artery and/or renal vein to temporarily stop blood flow to the affected area, followed by removal of the kidney tumor. The renal vessels and surrounding tissue are then carefully reconnected, and the clamps are removed to restore blood flow. It is essential to limit the time that blood flow is stopped, known as the ischemia time, to no more than 20 – 30 minutes to prevent permanent damage to the surrounding kidney tissue [101]. This study aimed to develop the automated segmentation was employed with AL to enhance efficiency and reduce labeling efforts for the limited training data available.

### *Procedure*

The study procedure is depicted in Figure 3-1. First, kidney CT images were obtained and manually segmented by experts to create a ground truth, which was confirmed by a clinician with over ten years of experience. Next, the images were pre-processed, and a detection module with 3D U-Net structures was used for training. Predictions were then made to establish ROIs. The images and labels were cropped to include a margin around the ROI, and the segmentation module with a cascade 3D U-Net was used for training. If more datasets were available, the training model predicted the segmentation of new kidney CT images, and the AL-corrected segmentation was used to expand the ground truth data. The pre-processing and training process was repeated with the original and added datasets until no additional datasets were available. The study involved evaluating and analyzing the results obtained from the repeated training.



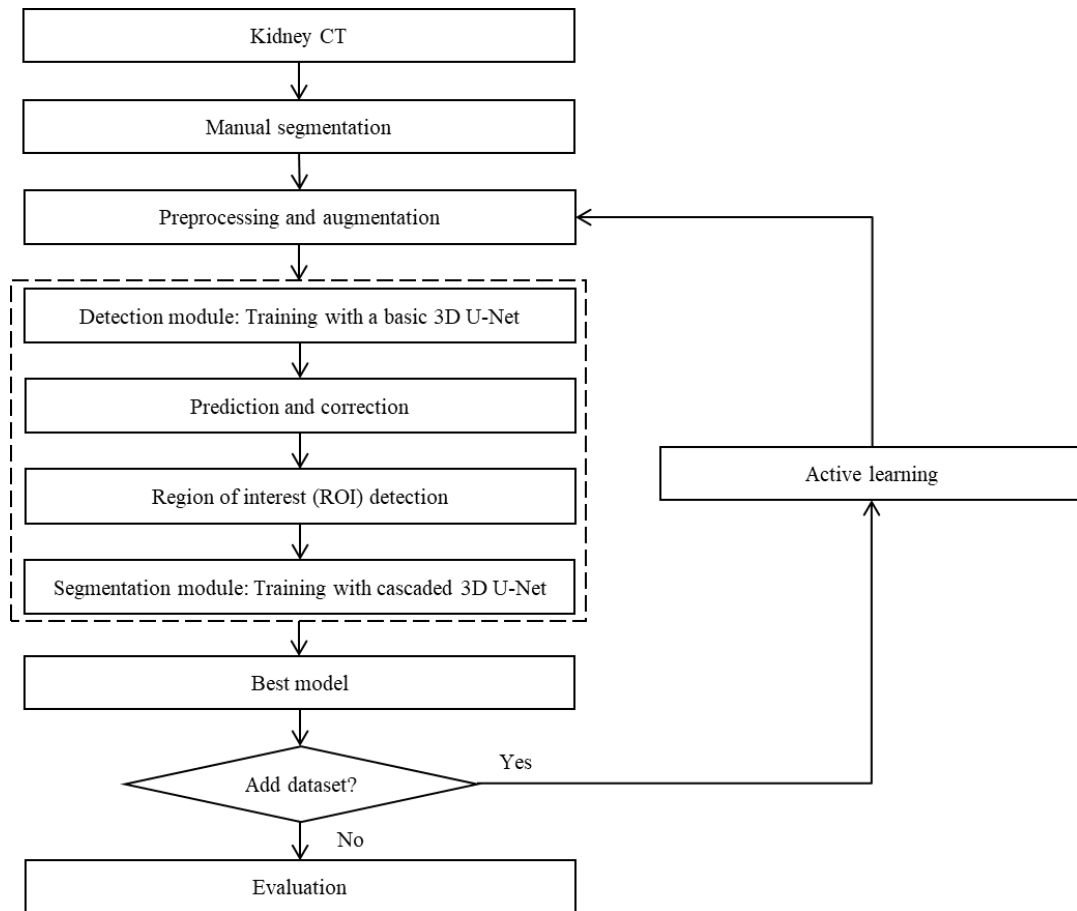


Figure 3-1. The overall procedure s of cascade 3D U-Net using active learning (AL) in kidney CT.

### *Dataset*

The study utilized 50 kidneys from 36 patients, of which 30 had RCCs, and 20 were normal kidneys. The kidneys were obtained from abdominal CT scans (Siemens Healthcare's Sensation 16), which had a slice thickness of 1.00 – 1.25 mm each. The CT scans had four phases: non-contrast, renal cortical, renal parenchymal, and renal excretory phases. For the classification of kidneys, the renal cortical phase, which highlighted the arteries, was used. The kidneys were categorized into five subclasses: artery, vein, ureter, parenchyma with medulla, and RCC in the case of kidneys with RCC. Kidneys that had cysts or stones were excluded from this study. The Institutional Review Board for human research at AMC granted approval for a retrospective study without requiring informed consent. The imaging data were de-identified to comply with the privacy rule of the Health Insurance Portability

and Accountability Act.

*Manually initial and AL-corrected segmentation*

The first step of the segmentation process involved positioning the FOV of the native aorta and applying a "Thresholding" technique (Figure 3-2 (A)), followed by selecting a seed point with 6-connectivity using "Region growing" (Figure 3-2 (B)). To fill the area outside the HU of the native aorta, the "Dilation and Erosion" function under "Morphology Operations" was utilized (Figure 3-2 (C)). The "Edit Mask" function was also utilized to eliminate any erroneous areas during the segmentation process (Figure 3-2 (D)). For AL-corrected segmentation, the same techniques as the initial segmentation were employed to generate predicted binary masks with the original CT image metadata. These masks were then superimposed onto the CT images and manually AL-corrected to create the final ground truth segmentation.

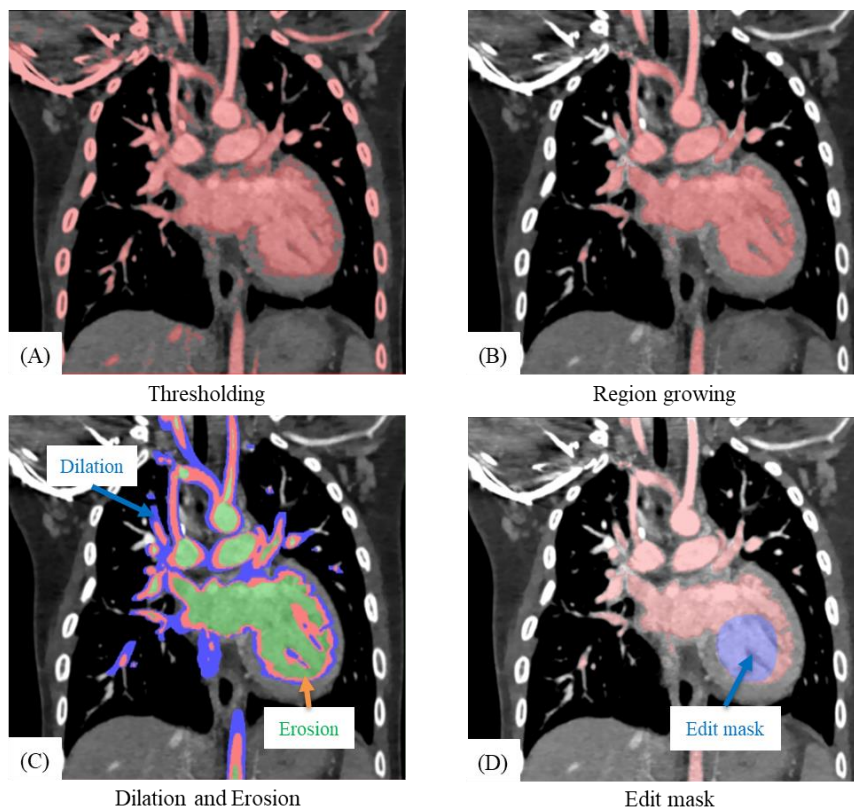


Figure 3-2. The manual segmentation techniques including (A) thresholding, (B) region growing, (C) dilation and erosion, and (D) edit mask.

### *Pre-processing*

Pre-processing involved two main tasks, which were normalization and image flip and resize. The initial pre-processing step was min-max normalization, which was applied to adjust the contrast of the CT images. This process involved converting all features to a value between 0 (minimum) and 1 (maximum), according to Eq. (1). Second, since each subject had two kidneys (Figure 3-3 (A)), separating the kidneys doubled the dataset (Figure 3-3 (B)). After dividing the right and left sides in the axial view, the left images were preserved, and the right images were horizontally flipped (Figure 3-3 (C)). Images in a basic 3D U-Net were resized to an FOV of  $128 \times 256 \times 192$  mm (Figure 3-3 (C)), and images in cascade 3D U-Net were resized to an FOV of  $96 \times 96 \times 96$  mm (Figure 3-3 (D)).

$$x_{new} = \frac{x_i - x_{min}}{x_{max} - x_{min}}, x_{min} = \frac{WL - WW}{2}, x_{max} = \frac{WL + WW}{2} \quad (1)$$

### *Active learning (AL)*

During the first stage of the study, five subcategories (artery, vein, ureter, parenchyma, and RCC) were manually outlined as the standard reference for initial training using 20 kidney samples. Subsequently, in the next stage, new data sets were manually AL-corrected by referring to the AL-corrected segmentation results, which was the outcome of using CNN segmentation. In the second stage of the study, 16 kidneys from the previous stage were utilized for training, along with new data consisting of 8 kidneys with RCCs and 8 normal kidneys as depicted in Figure 3-4. After stage 2, the outcomes of CNN segmentation for the new data were manually edited in preparation for the next stage, following the same method as used in stage 1. In the final stage of the study (stage 3), 40 kidneys were employed for training purposes while 10 kidneys were utilized for testing. The outcomes of all the previously mentioned stages were used to evaluate the accuracy of the study.

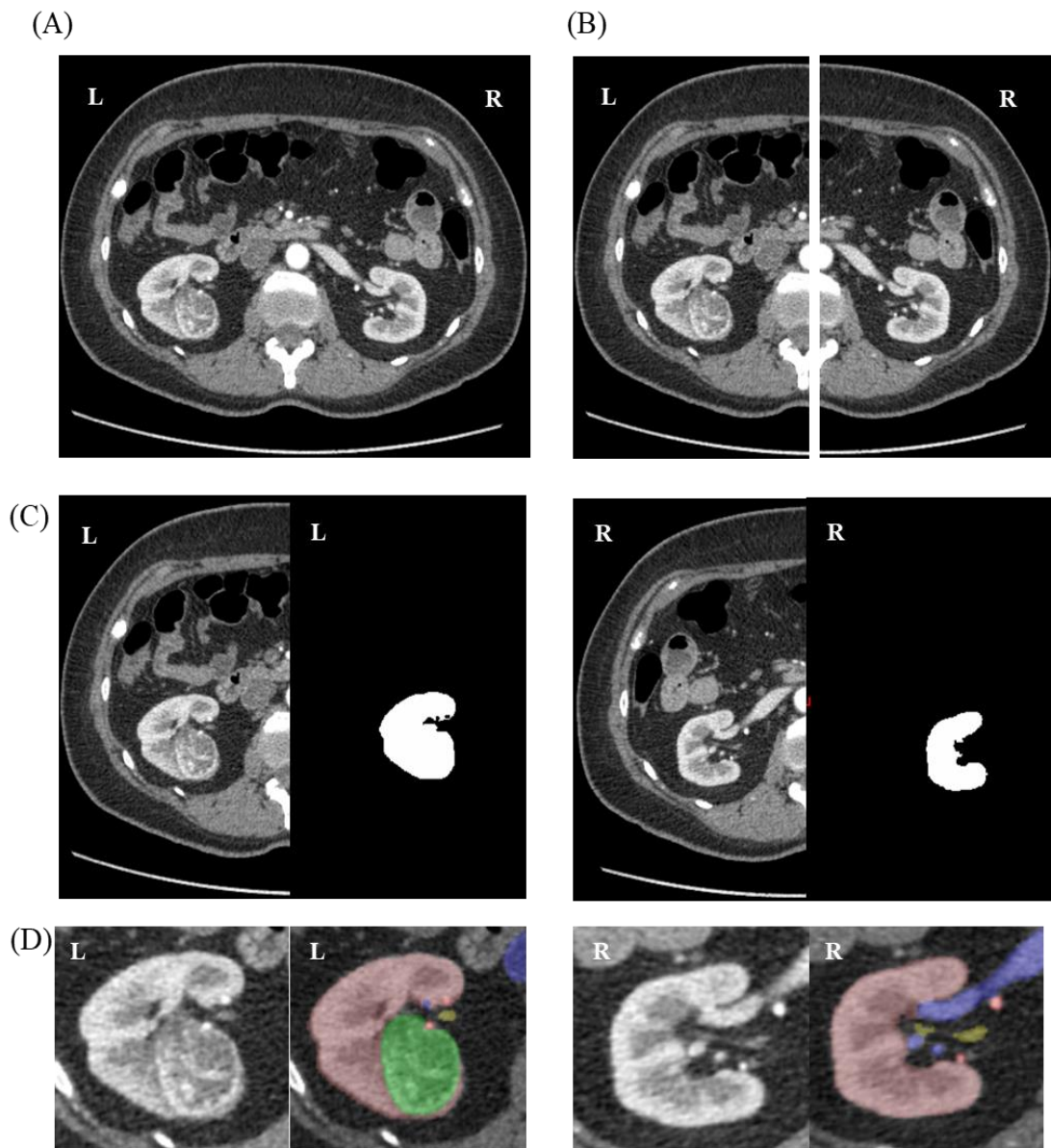


Figure 3-3. Pre-processing procedure for kidneys with a 3D U-Net and cascade 3D U-Net  
 (A) Normalization image, (B) Division by the right and left sides, (C) Flip the right images to horizontal, and (D) Crop image including the margin.

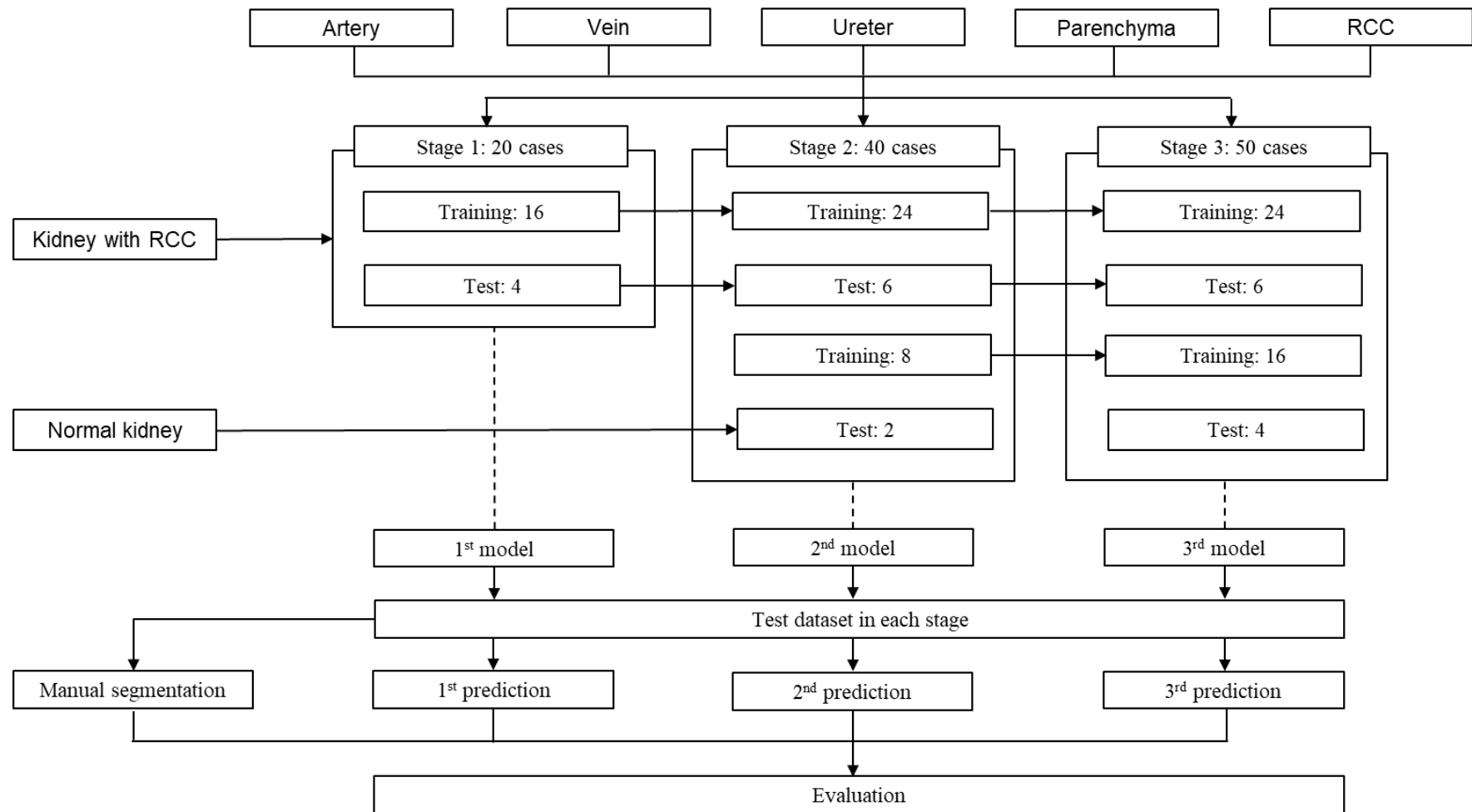


Figure 3-4. Data distribution in each stage for active learning (AL) in kidney CT.

### Networks and experimental settings

The cascade 3D U-Net model was trained separately in an end-to-end fashion. To determine the ROI, a cuboidal bounding box was utilized around the kidney after the first U-Net module (Figure 3-5 (A)). Subsequently, the second U-Net module was trained for the final segmentation to create the mask for the five subclasses of the kidney (Figure 3-5 (B)). In addition, a Gaussian was added to each input image. The Keras 2.2.4 model with a TensorFlow 1.14.0 backend was employed, and the training was executed with an NVIDIA GTX 1080 Ti GPU. Our cascade method usually necessitates a substantial number of epochs for both stages of training. During the first stage of training, the number of datasets was limited (N=20), resulting in saturation of training at approximately 150 epochs. However, for the second and third stages, a larger number of datasets (N = 40 and 50) were utilized, requiring 300 epochs of training. The Adam optimizer was implemented with a learning rate of 10<sup>-5</sup>, weight decay of 0.0005, momentum of 0.9, and the average dice coefficient loss as the training loss, with a batch size of 1.

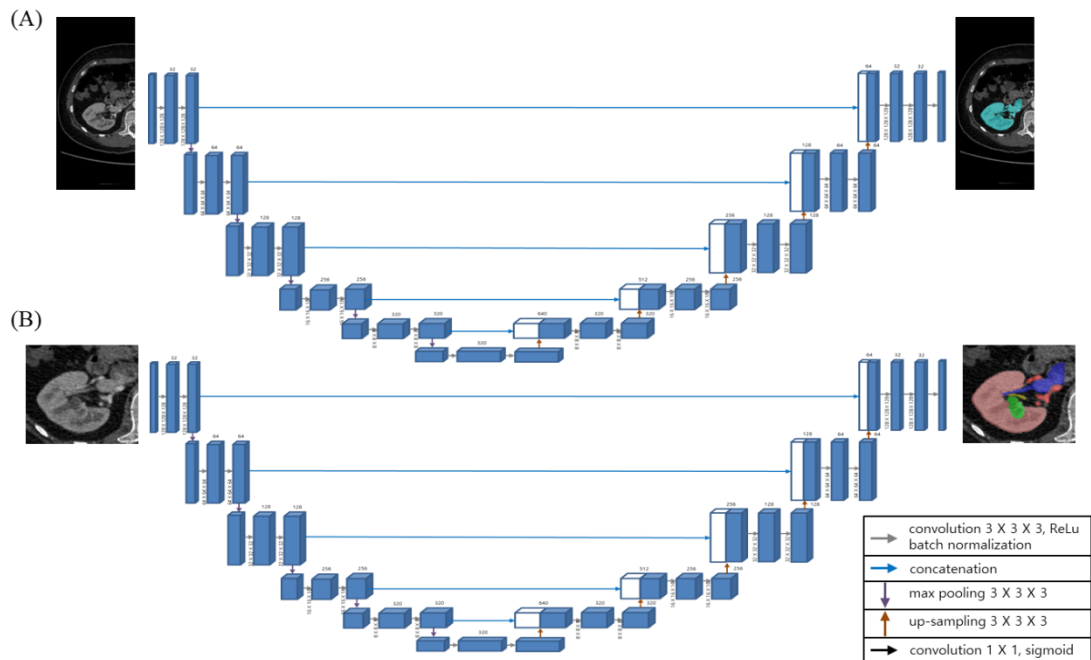


Figure 3-5. The architecture of (A) a basic 3D U-Net and (B) a cascaded 3D U-Net

### Evaluation

To evaluate whether the performance of the network improves with AL, we examined the dice similarity coefficient (DSC) at each stage and conducted a paired t-test to compare stages 1 and 3, as well as stages 2 and 3. DSC was utilized to evaluate the matching area of the predicted label against the ground truth. The DSC ranges from 0 to 1, with 0 indicating no overlap between the volumes and 1 indicating a perfect overlap between the volumes. The DSC was calculated using eq (2).

$$DSC(V_{GT}, V_{Pred}) = \frac{2|V_{GT} \cap V_{Pred}|}{|V_{GT}| + |V_{Pred}|} \quad (2)$$

where  $V_{GT}$  and  $V_{Pred}$  were the volume of ground truth and predicted label, respectively. We also assessed the accuracy and labeling efficiency of the AL-corrected segmentation to validate its effectiveness. We created 3D models from the results of manual, CNN, and AL-corrected segmentation, and compared their accuracy. The comparison was based on surface points, and we used quantitative root mean square (RMS) values. Specifically, we compared 17,650 points to assess the differences between the 3D models generated from manual and CNN segmentations, as well as those generated from manual and AL-corrected segmentations. To compare the accuracy between CNN segmentation and AL-corrected segmentation, we used 26,471 points and calculated the RMS value using the same method as in Eq. (3), where  $x$  represents the difference between the corresponding points in the two models, and  $n$  is the total number of points used in the comparison.

$$RMS = \sqrt{\frac{1}{n}(x_1^2 + x_2^2 + x_3^2 + \dots + x_n^2)} = \sqrt{\frac{1}{n} \sum_{k=1}^n x_k^2} \quad (3)$$

The time efficiency of manual and AL-corrected segmentation based on predicted labels generated by the basic 3D and cascade 3D U-Nets was also evaluated.

## Results

Table 3-1 shows the DSC for the five subclasses in each stage. The average DSC values for the five subclasses increased with each stage. Among the subclasses, parenchyma segmentation had the highest DSC and lowest SD, while RCC had the lowest DSC and highest SD.

Table 3-1. Dice similarity coefficient for each stage of kidney with cascade 3D U-Net in kidney CT.

Class	Dice similarity coefficient (DSC)			P	
	Stage 1	Stage 2	Stage 3	Stage 1 and 3	Stage 2 and 3
Artery	0.443 ± 0.101	0.660 ± 0.087	0.636 ± 0.129	0.372	0.704
Vein	0.726 ± 0.104	0.779 ± 0.084	0.750 ± 0.134	0.837	0.873
Ureter	0.480 ± 0.120	0.604 ± 0.077	0.606 ± 0.085	0.088	0.655
Parenchyma	0.958 ± 0.056	0.961 ± 0.007	0.963 ± 0.007	0.697	0.772
RCC	0.115 ± 0.146	0.468 ± 0.304	0.526 ± 0.346	0.239	0.131
Total	0.545 ± 0.303	0.707 ± 0.213	0.711 ± 0.217	0.252	0.330

Table 3-2 shows the comparison of segmentation time for the five substructures between manual and AL-corrected segmentation. This study found that using AL-corrected segmentation reduced the time for segmenting the artery, vein, ureter, parenchyma, and RCC by 19.13, 12.17, 19.38, 8.33, and 17.13 min, respectively, resulting in an overall segmentation time reduction of 76 min, which is more than half of the time required for manual segmentation.



Table 3-2. Comparison of segmentation time for kidney between manual and AL-corrected segmentation in kidney CT.

Time	Manual segmentation (min)	CNN-assisted segmentation (min)
Artery	41.13	22.00
Vein	35.02	23.00
Ureter	24.38	5.00
Parenchyma	26.43	18.10
RCC	22.13	5.00
Total	149.10	73.10

The CNN segmentation took less than 1 second per case, except for the initial loading of the package. The results of the quantitative evaluation in 3D models showed that AL-corrected segmentation highly corresponded with manual segmentation, while CNN segmentation did not. Details of the differences among the three segmentation methods are presented in Table 3-3 and Figure 3-6

Table 3-3. Root mean square (RMS) evaluation from 3D modeling for kidney.

Comparison	RMS (mm)
Manual segmentation and CNN segmentation	$2.22 \pm 2.06$
AL-corrected segmentation and CNN segmentation	$2.77 \pm 2.77$
Manual segmentation and CNN-assisted segmentation	$0.86 \pm 0.80$

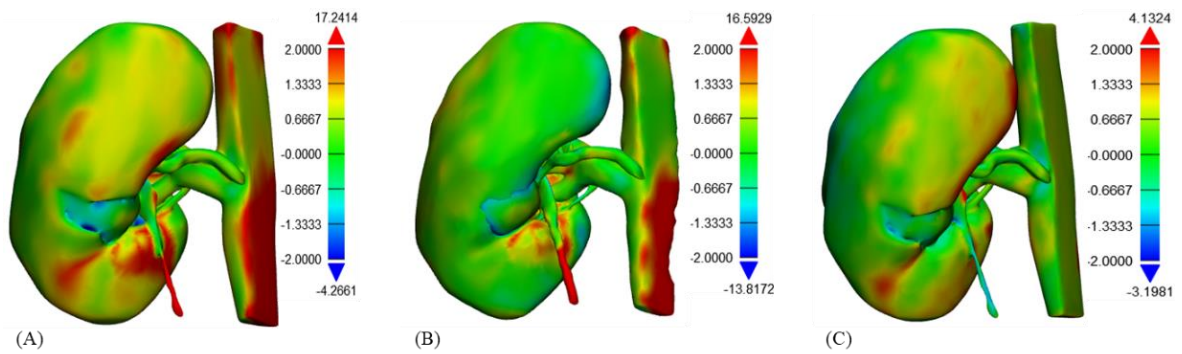


Figure 3-6. Root mean square (RMS) evaluation from 3D model about kidney with RCC

### 3.2 Mandibular condyle in dental CBCT

The mandibular condyle is responsible for the growth of the lower jaw, and orthopaedic appliances like activators, facemasks, and chin cups can be used to control the direction and amount of this growth during development. These appliances generate forces that influence the growth pattern of the mandible [102-104]. Once growth of the mandibular condyle is finished, it undergoes natural remodeling based on the functional load placed on the temporomandibular joint (TMJ). However, if the TMJ is excessively loaded due to parafunctional habits like clenching and bruxism, this can cause degenerative changes in the condyles [105]. Orthognathic surgery can alter the pattern of functional loading on the TMJ, potentially leading to remodeling of the mandibular condyle [106]. It is important to make an accurate assessment of the morphology of the mandibular condyle to understand how growth has been modified, diagnose osteoarthritis of the TMJ, and evaluate skeletal changes resulting from orthodontic and orthognathic treatments. To quantitatively assess changes in the morphology of the condyle, a 3D model can be constructed by segmenting volumetric images obtained from techniques such as CT [107, 108]. Volumetric segmentation, which is the process of identifying and separating the object of interest from surrounding structures in a 3D volume, can be accomplished through manual, semi-automatic, or fully automatic methods. Manual and semi-automatic methods involve segmenting the object of interest in each 2D slice image and reconstructing the 3D volume, which can be done using medical image analysis software [109-111]. Manual or semi-automatic segmentation can be

challenging as it requires extensive training to accurately identify and segment the condylar head from the surrounding glenoid fossa. This is due to the low bone density of the TMJ area and the lack of contrast, especially in low-dose CT images such as cone beam CT (CBCT) [112]. DL algorithms, specifically U-Net, a convolutional neural network, have been used for automated segmentation of the mandibular condyle. Liu et al. [113] utilized U-Net to initially classify CT images into three regions: condyle, glenoid fossa, and background. They then used the snake algorithm for secondary segmentation. Kim et al. [114] utilized a 2D U-Net algorithm to directly segment the mandibular condyles in axial slice images, which were then reconstructed into a 3D model. However, annotating 2D slice images for a 3D volume can be a time-consuming process. To address this issue, AL and self-supervised learning algorithms have been developed and applied to reduce the amount of training data required [81]. Çiçek et al. [58] proposed using the 3D U-Net architecture instead of annotating 2D images. This architecture is similar to the previous U-Net, but it utilizes 3D volumes as input data and includes 3D convolutions, 3D max pooling, and 3D up-convolutional layers. The main advantage of using the 3D U-Net is that it considers the 3D integrity of anatomy and pathologic lesions during training, which is not possible with the 2D U-Net. In addition, the 3D U-Net is able to generalize well [27, 115]. To improve the segmentation performance, researchers have recently used cascade 3D U-Net, which involves using two or more networks. The second network is used to detect the ROI and focus training on the target region, resulting in more accurate segmentation. In a study conducted by Liu et al, [116] the performance of cascade 3D U-Net for brain tumor segmentation was compared. They found that the DSC of the cascade U-Net improved by 0.014, 0.052, and 0.033 for the whole tumor, tumor core, and enhanced tumor, respectively, indicating better segmentation accuracy. Ham et al. [117] proposed an automated segmentation method for four different components, namely craniofacial hard tissues, maxillary sinus, mandible, and mandibular canals, from facial CBCT scans using the 3D U-Net architecture. They were used to segment the entire craniofacial hard tissues with four CBCTs, while twenty CBCTs were used for automated segmentation of the mandible. However, since the mandibular segmentation model targeted the entire mandible, the segmentation results lacked accuracy in the condylar region for analytical purposes. Therefore, we developed an automated segmentation algorithm for the

mandibular condyles using cascade 3D U-Net and conducted a stress test to determine the optimal dataset size for developing the model.

*Procedure*

The overall study procedure is illustrated in Figure 3-7. The acquired CBCT images were manually segmented by experts to generate the ground truth, which was further confirmed by a clinician with more than ten years of experience. After pre-processing, training was carried out using 3D U-Net structures and predictions were performed to establish ROIs. The images and labels were cropped, including a margin around the ROI, and training was again performed with a cascade 3D U-Net. To compare accuracy, a basic 3D U-Net and a cascade 3D U-Net were used after ROI detection. If more datasets are available, the trained model is used to predict the segmentation of new CBCT images, and the AL-corrected segmentation is used to expand the ground truth data. The pre-processing and training process is then repeated with both the original and additional datasets until no more datasets are available. Finally, the results obtained from the repeated training are evaluated and analyzed.

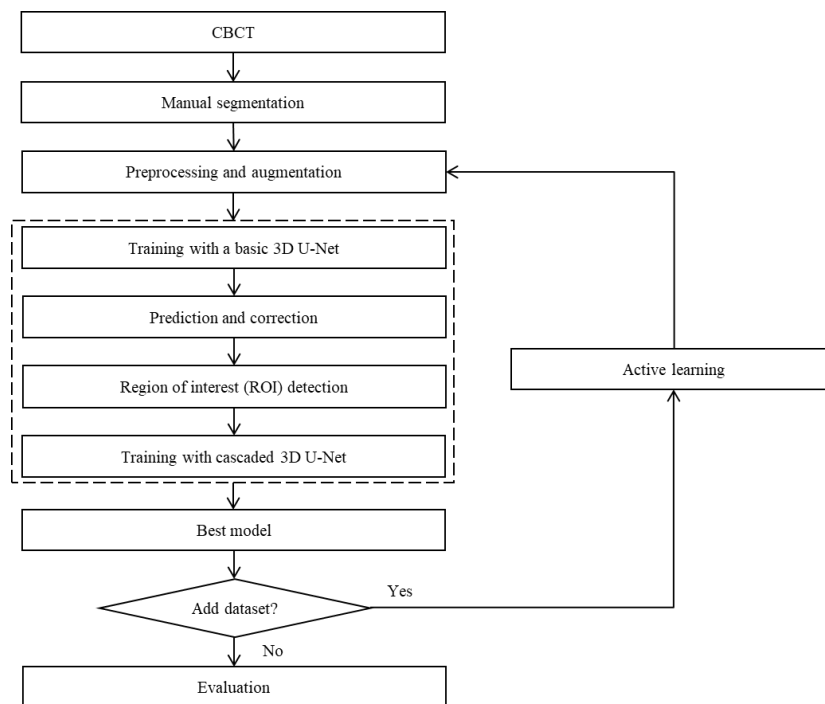


Figure 3-7. The overall procedure s of a basic 3D U-Net and its based cascade 3D U-net using active learning (AL) in CBCT.

### *Dataset*

This study received approval from the institutional review boards of Korea University Medical Center (KUMC) (IRB no. 2019AN0213) and AMC (IRB no. 2019-0927). The patient data used in the study were de-identified. The CBCT dataset was obtained from patients who had undergone CBCT scans at the department of dentistry between 2018 and 2020 with a slice thickness of 0.30 mm, a field of view (FOV) of 400–768 X 400–768 X 256–576, and a pixel size of 0.30 mm. Patients aged between 18 and 40 years were included in the study, while those who exhibited osteoarthritic changes in the condyles were excluded. The CBCT scans were converted to the DICOM format and anonymized. The dataset comprised of 234 mandibular condyles from 117 subjects. To ensure consistent orientation across all images, the images of the right-side condyles were horizontally flipped.

### *Manually initial and AL-corrected segmentation*

To perform the initial segmentation, the FOV of the native aorta was positioned, and "*Thresholding*" was used to select the HU of the aorta (Figure 3-2 (A)). A seed point with 6-connectivity was chosen using "*Region growing*" (Figure 3-2 (B)). The area outside the HU of the native aorta was filled by applying "*Dilation and Erosion*" under "*Morphology Operations*" (Figure 3-2 (C)). For small segmental arteries, aneurysms with a limited amount of injected contrast medium, and blood vessel wall dissection, manual segmentation was carried out using the "*Edit Mask*" feature (Figure 3-2 (D)). This function was also utilized to eliminate any inaccurate regions. In AL-corrected segmentation, the same techniques were applied as in the initial segmentation to produce predicted binary masks with the original CT image metadata. These masks were superimposed onto the CT images, and were manually refined to create the ground truth segmentation.

### *Pre-processing*

The ROI for the condyle head was defined after re-orienting the image using the orbital and Frankfort horizontal plane, and the lower border of the condyle was identified as the horizontal plane passing through the sigmoid notch. Pre-processing involved two main tasks, which were normalization and image flip and resize. The initial pre-processing step was min-

max normalization, which was applied to adjust the contrast of the CT images. This process involved converting all features to a value between 0 (minimum) and 1 (maximum), according to Eq. (1), with a center of 300 and a width of 2000. Second, since each subject had two mandibular condyles (Figure 3-8 (A)), separating the condyles doubled the dataset (Figure 3-8 (B)). After dividing the right and left sides in the axial view, the left images were preserved, and the right images were horizontally flipped (Figure 3-8 (C)). Images in a basic 3D U-Net were resized to an FOV of  $128 \times 256 \times 192$  mm (Figure 3-8 (C)), and images in cascade 3D U-Net were resized to an FOV of  $80 \times 80 \times 80$  mm (Figure 3-8 (D)).

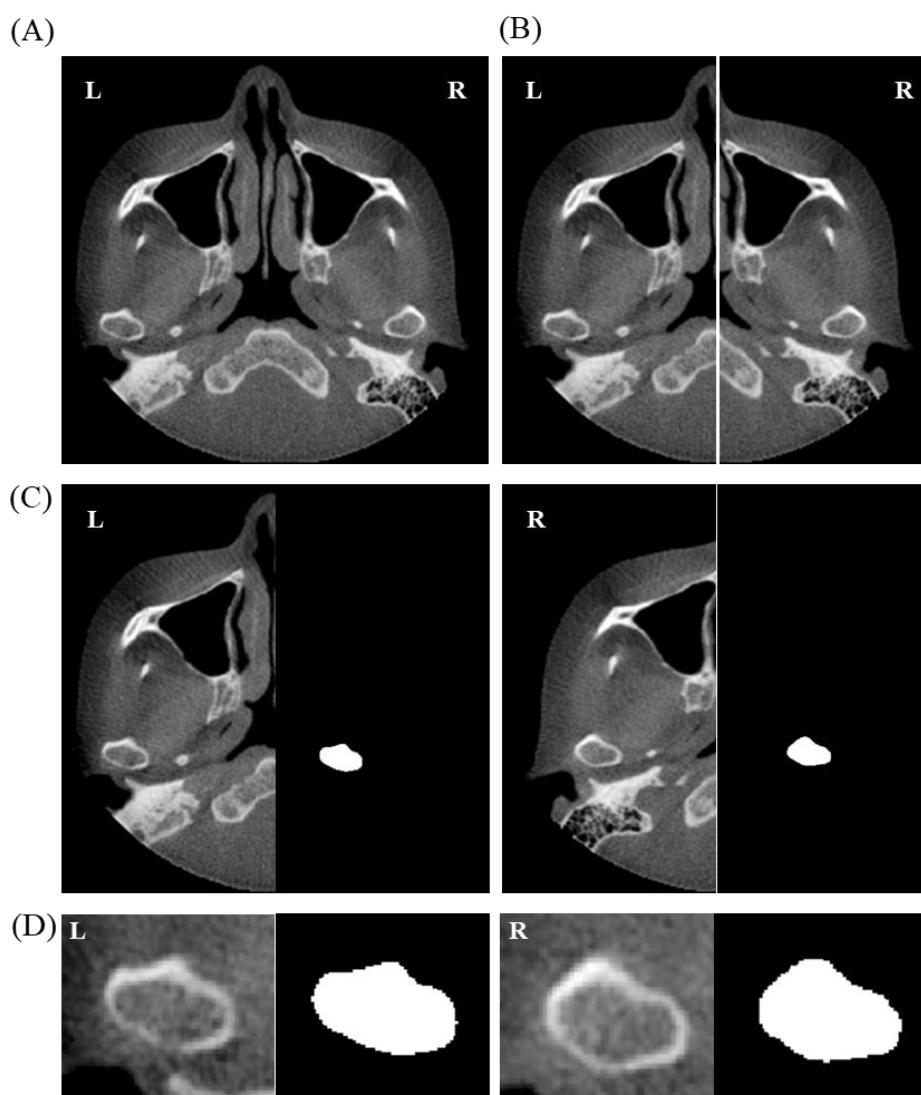


Figure 3-8. Pre-processing procedure for mandibular condyles with a basic 3D U-Net and cascade 3D U-Net (A) Normalization image, (B) Division by the right and left sides, (C) Flip the right images to horizontal, and (D) Crop image including the margin.

### *Active learning (AL)*

To facilitate AL, we categorized the 234 mandibular condyles of 117 subjects into five stages, each with its own distribution of training, validation, and testing data as shown in Figure 3-8. During the first stage, we manually established ground truths for training, validation, and testing using 80 mandibular condyles from KUMC, with 64 for training, 8 for validation, and 8 for testing. In the following stage, we refined the results of the cascade 3D U-Net model to manually generate AL-corrected segmentation ground truths for new data. For stage 2, we augmented the 120 mandibular condyles from KUMC used in the previous stage with additional new data for training purposes. For subsequent stages after stage 1, we manually AL-corrected the results obtained from the cascade 3D U-Net model for new data to generate AL-corrected segmentation ground truths, similar to the approach used in stage 1. We followed a similar process for stages 3 and 4 using 120 mandibular condyles of KUMC for stage 3 and 128 mandibular condyles of KUMC and 72 mandibular condyles of AMC for stage 4. In the final stage, we used all 162 mandibular condyles of KUMC and 72 mandibular condyles of AMC for training and evaluated the accuracy using the results obtained from all the previous stages (Figure 3-9).

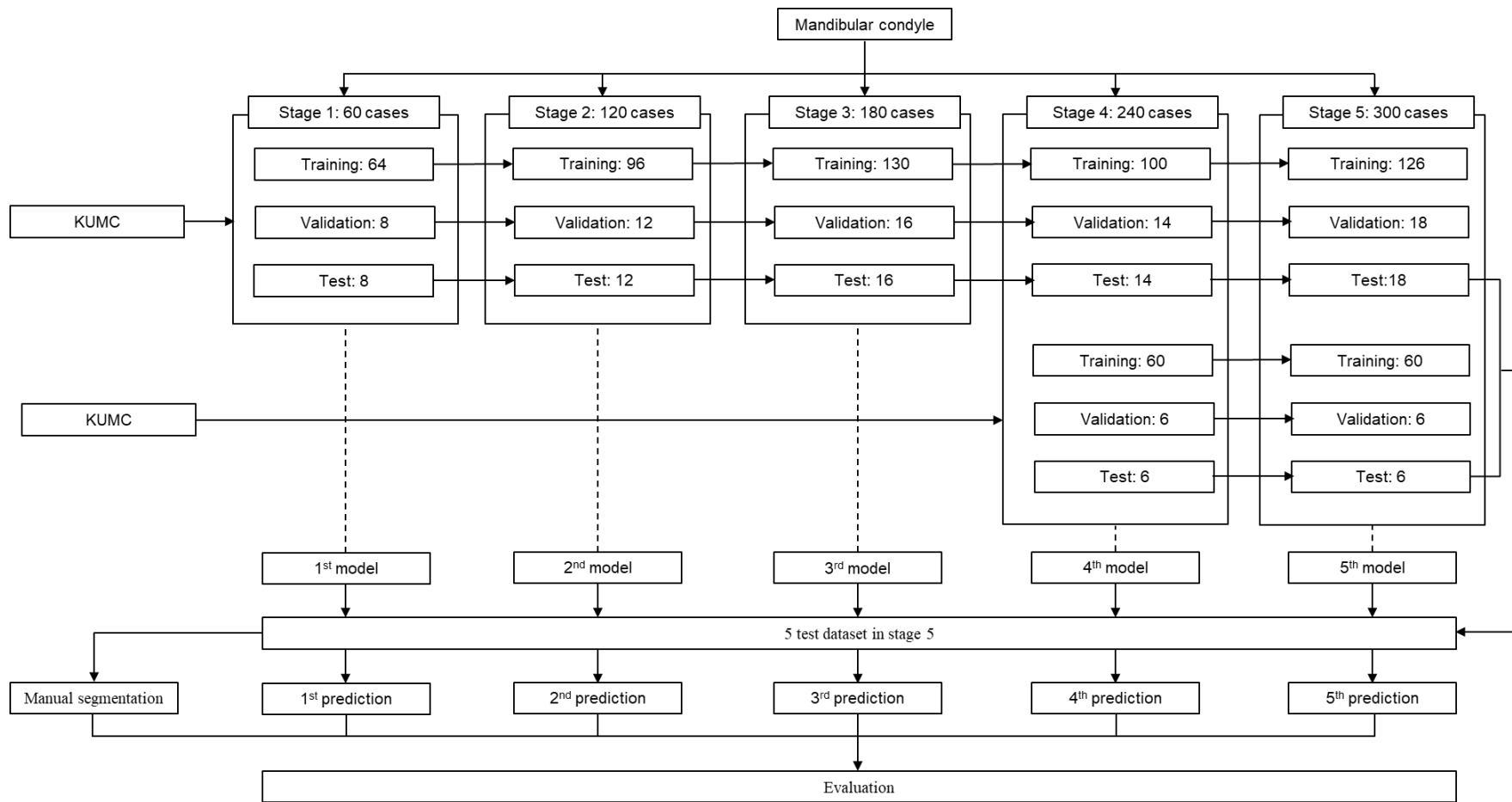


Figure 3-12. Data distribution for mandibular condyle in each stage for active learning

Figure 3-9. Data distribution for mandibular condyle in each stage for active learning (AL).



### Networks and experimental settings

To perform the segmentation task, two types of 3D U-Net models were utilized: a basic 3D U-Net and a cascade 3D U-Net. Initially, the basic 3D U-Net was employed for pre-processing and segmenting the condyles (Figure 3-10 (A)). Then, the cascade 3D U-Net was applied to the ROIs (mandibular condyle), including their margins, which were detected by the basic 3D U-Net. The predicted mandibular condyle region was used to define margins, which were determined by setting the maximum (max) and minimum (min) values for the x, y, and z axes, and then expanded by five pixels based on empirical evidence. The medical images and labels were then cropped to this margin region, and the resulting input datasets were trained again using the 3D U-Net architecture (Figure 3-10 (B)). Ultimately, the cascade 3D U-Net was used to generate predicted labels for the mandibular condyle. The average dice coefficient loss was utilized as the training loss. The training was performed using a NVIDIA TITAN RTX GPU with 24,220 MiB of available memory, and the Keras 2.3.0 and TensorFlow 1.15.0 backend were utilized to execute the training module.

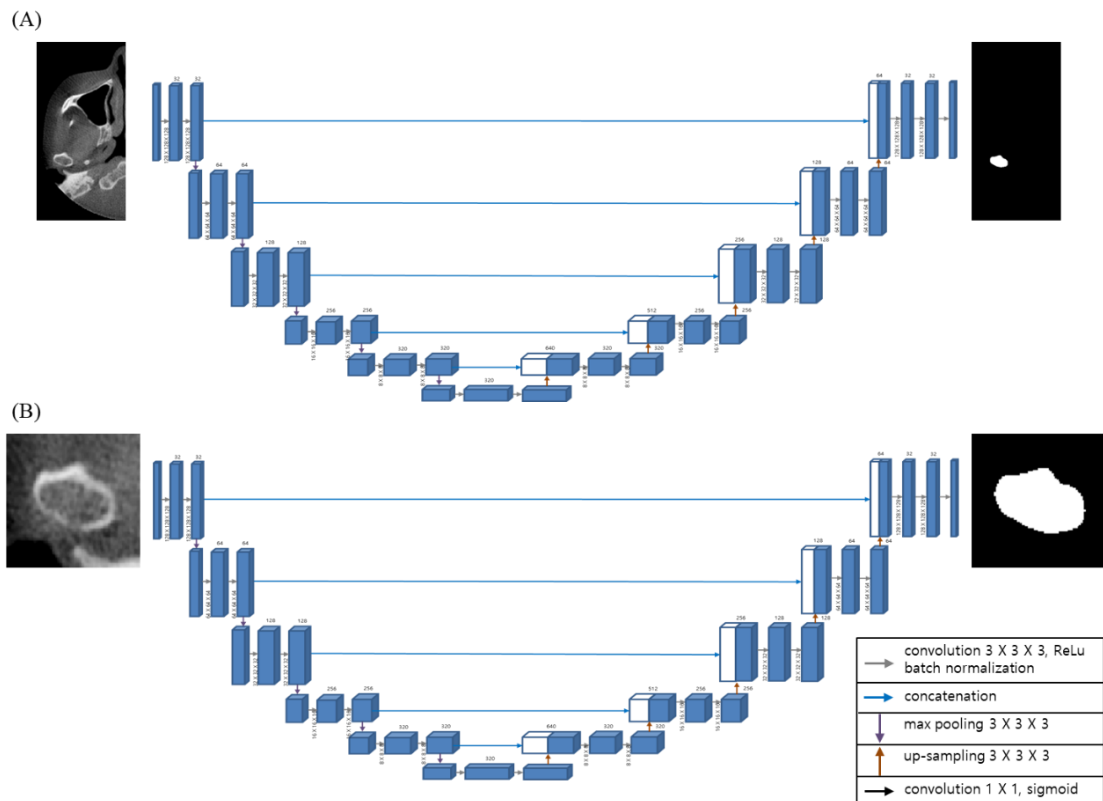


Figure 3-10 The architecture of (A) a basic 3D U-Net and (B) a cascaded 3D U-Net.

### *Evaluation*

The performance of the basic 3D U-Net and the cascade 3D U-Net models was evaluated using the DSC, which ranges from 0 to 1, with 0 indicating no overlap between the volumes and 1 indicating a perfect overlap. The DSC values were calculated using Eq. (2). 95% HD (Hausdorff distance) was used to evaluate the matching distance between the ground truth and predicted label obtained by the basic 3D U-Net and the cascade 3D U-Net using Eq. (4). The 95% HD is a metric that is calculated based on the distances as an Eq. (4) with sets  $A = \{a_1, a_2, a_3, \dots, a_n\}$  and  $B = \{b_1, b_2, b_3, \dots, b_n\}$ .

$$HD(A, B) = \max\left(\max_{a \in A} \min_{b \in B} A - B, \max_{a \in B} \min_{b \in A} B - A\right) \quad (4)$$

where sets A and B were points of ground truth and predicted labels. It is similar to the maximum HD, but it eliminates the impact of outliers by taking the 95th percentile of the distances. This ensures that the metric is not overly influenced by a very small subset of extreme values. To compare the performance difference between the basic 3D U-Net and the cascade 3D U-Net, a paired t-test was utilized to determine significant differences. The time efficiency of manual and AL-corrected segmentation based on predicted labels generated by the basic 3D and cascade 3D U-Nets was also evaluated.

### *Results*

The results of the DSC and HD for each stage are presented in Table 3-4, along with their average and SD. A comparison between the basic 3D U-Net and cascade 3D U-Net showed that the use of the cascade 3D U-Net resulted in higher DSC values in all stages, and DSC were statistically significant differences except for stage 4. However, In HD, on the contrary to DSC, a basic 3D U-Net showed better performance and a statistically significant difference (Table 3-4).

Table 3-4. Dice similarity coefficient and Hausdorff distance for each stage of mandibular condyles with a basic 3D U-Net and cascade 3D U-Net in CBCT.

Metric	Model	Stage 1	Stage 2	Stage 3	Stage 4	Stage 5
DSC	Basic 3D U-Net	$0.854 \pm 0.077$	$0.872 \pm 0.100$	$0.891 \pm 0.056$	$0.917 \pm 0.029$	$0.922 \pm 0.021$
	Cascade 3D U-Net	$0.908 \pm 0.042$	$0.916 \pm 0.045$	$0.921 \pm 0.036$	$0.930 \pm 0.027$	$0.932 \pm 0.023$
	P	<0.001	<0.01	<0.001	0.053	<0.05
HD95	Basic 3D U-Net	$2.514 \pm 1.274$	$2.205 \pm 1.494$	$1.990 \pm 1.103$	$1.495 \pm 0.484$	$1.289 \pm 0.303$
	Cascade 3D U-Net	$3.376 \pm 1.951$	$3.349 \pm 2.244$	$2.756 \pm 1.500$	$2.897 \pm 2.707$	$2.823 \pm 2.402$
	P	<0.01	<0.001	<0.001	<0.05	<0.01

Figure 3-11 shows the best and worst cases for a difference map between the ground truth and prediction with basic 3D U-Net and cascaded 3D U-Net in stage 5. The positive and negative areas depict over-segmentation and under-segmentation, respectively. The best cases of basic 3D U-Net and cascaded 3D U-Net showed a DSC of 0.960 (error range, -0.23–0.44 mm) and 0.961 (error range, -0.36–0.29 mm), respectively (Figure 3-11 (A) and (C)); the worst cases of basic 3D U-Net and cascaded 3D U-Net showed a DSC of 0.864 (error range, -1.07–0.46 mm) and 0.890 (error range -0.32–1.69 mm), respectively (Figure 3-11 (B) and (D)).

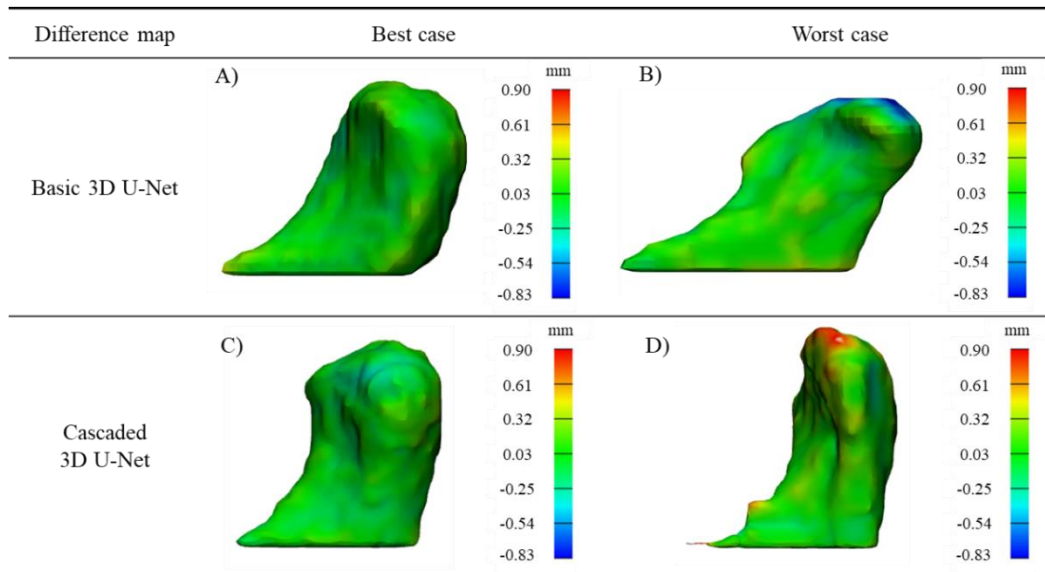


Figure 3-11. The difference map between ground truth and prediction in 3D U-Net and cascaded 3D U-Net. (A) The best case and (B) worst case of 3D U-net, and (C) the best case and (D) worst case of cascaded 3D U-Net.

Table 3-5 reports the time required for manual and AL-corrected segmentation based on predicted labels obtained using basic 3D U-Net and cascade 3D U-Net. The average time for manual segmentation was  $14.75 \pm 3.63$  minutes, while segmentation using basic 3D U-Net and cascade 3D U-Net took  $4.13 \pm 1.94$  minutes and  $2.31 \pm 1.54$  minutes, respectively. The spent time between manual and AL-corrected segmentation with a basic 3D U-Net and a cascade 3D U-Net were statistically significant difference ( $p < 0.001$ )

Table 3-5. Segmentation time of mandibular condyles for manual, basic 3D U-Net, and cascade 3D U-Net in stage 5 of CBCT.

Patient No.	Manual (min)		Basic 3D U-Net (min)		Cascade 3D U-Net (min)	
	R	L	R	L	R	L
1	23.08	16.43	5.58	3.75	6.80	6.28
2	14.08	9.83	3.80	6.77	0.73	3.75
3	13.88	10.82	2.98	3.13	1.53	3.05
4	13.08	10.22	1.92	5.93	1.06	2.22
5	17.98	19.87	1.63	4.05	0.45	1.77
6	13.60	10.40	1.10	2.97	1.53	3.13
7	14.36	12.92	2.67	2.75	0.59	1.52
8	15.95	16.90	2.75	4.70	1.66	4.25
9	14.40	14.23	6.50	1.07	0.48	1.75
10	16.92	9.38	6.93	5.68	3.73	2.52
11	18.52	20.28	6.13	7.35	2.77	5.33
12	14.25	14.23	3.87	4.80	1.23	1.73
Mean $\pm$ SD						
	15.98 $\pm$ 2.98	13.51 $\pm$ 3.93	3.82 $\pm$ 2.10	4.41 $\pm$ 1.82	1.43 $\pm$ 1.01	3.11 $\pm$ 1.53

### 3.3 Thoracoabdominal aortic dissection in CT angiography

Aortic aneurysms are life-threatening disorders that increase the risks of aortic dissection or rupture with fatal outcomes [118]. Surgical or interventional therapies that anatomically replace the diseased aortic segments are the only treatments proven to prevent catastrophic aortic events. Within this disease entity, thoracoabdominal aortic dissection is the most extensive and challenging pathology; it requires the replacement of the diseased aorta including the downstream thoracic and abdominal segments, along with the reconstruction of the visceral arteries (celiac and superior mesenteric artery), bilateral renal arteries and several segmental arteries (intercostal and lumbar arteries) that supply blood to the spinal cord [119]. To perform this extensive surgical procedure, extracorporeal circulation, as well as selective perfusion to visceral and renal arteries are mandatory, both of which increase the invasiveness and level of surgical stress. Open surgical repair of thoracoabdominal aorta is

well known as the most difficult and challenging surgical procedure, and operative outcomes remain reportedly poor, even by the world-leading expert groups, and the rates of surgical mortality, major stroke, and paraplegia are 9.5%, 11.6% , and 13.9%, respectively [119]. Various efforts have been made to reduce such related risks in thoracoabdominal aorta surgery, including the use of the four-branched aortic graft for more efficient revascularizations of aortic branching arteries through the aid of commercially available products. In addition to this technique, the use of an eight-branched aortic graft—so called “octopod graft technique,” has also been introduced to enable efficient revascularization of the spinal cord feeding arteries, which are known to be pivotal in preventing paraplegia (Figure 3-12) [120]. The octopod technique involves constructing a pre-sewn multi-branched aortic graft before surgery through an image-based technique (IBT); it entails grafting branches for the intercostal and lumbar arteries (spinal cord suppliers) on commercially available four-branched grafts considering the anatomical relationship based on the preoperative CT images because the anatomical location of these vessels significantly vary among patients [119, 121-123].

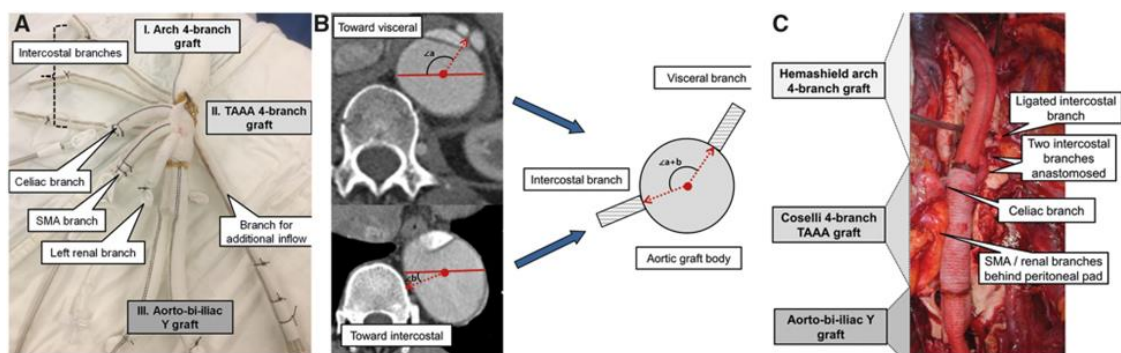


Figure 3-12. (A) The octopod thoracoabdominal aortic aneurysm (TAAA) aortic graft. (B) Representative computed tomographic images at the visceral and intercostal level. (C) Intraoperative findings of the octopod TAAA graft [120].

However, this conventional image-based approach has several shortcomings with respect to the precise positioning of the branching grafts because the accuracy depends on the constructor, usually, the operating surgeon. To overcome this limitation, we developed a

patient-specific graft reconstruction guide [124, 125] and introduced an automated segmentation as the first step.

### *Procedure*

The overall procedure, as shown in Figure 3-13, involves initially manually segmenting the aorta and vessels composed of the aorta and the celiac, mesenteric, renal, and intercostal arteries based on CT angiography. This is followed by pre-processing and augmentation, which includes normalization, cropping, and resampling, for data learning. The models used for training include UNETR and SwinUNETR of MONAI and 2D U-Net, 3D U-Net, 2D-3D U-Net ensemble, and cascade 3D U-Net of nnU-Net. If additional datasets are available, the best model from the several trained models is used to predict the segmentation of the added CT images. AL-corrected segmentation is performed based on this prediction to increase the amount of ground truth data. The process is then repeated starting from pre-processing and augmentation using the original and added datasets. If there are no more additional datasets to add, the results obtained from the repeated training are evaluated and analyzed.

### *Dataset*

A total of 47 subjects with Crawford types II or III were enrolled in Asan Medical Center (AMC) between January 2017 and February 2020. All of the participants underwent CT angiography with a slice thickness of 1.0–5.0 mm, a field of view (FOV) of 512 X 512 X z-axis, and a pixel size of less than 1.0 mm. All of the participants underwent open surgical repair, which required to reconstruct a patient-specific graft to replace the existing aorta. The intercostal arteries that needed to be reconstructed were chosen from those located between the thoracic-8 and lumbar-2 levels, while the main aortic graft reconstruction ranged from the left subclavian artery to the infra-renal abdominal or bilateral common artery.

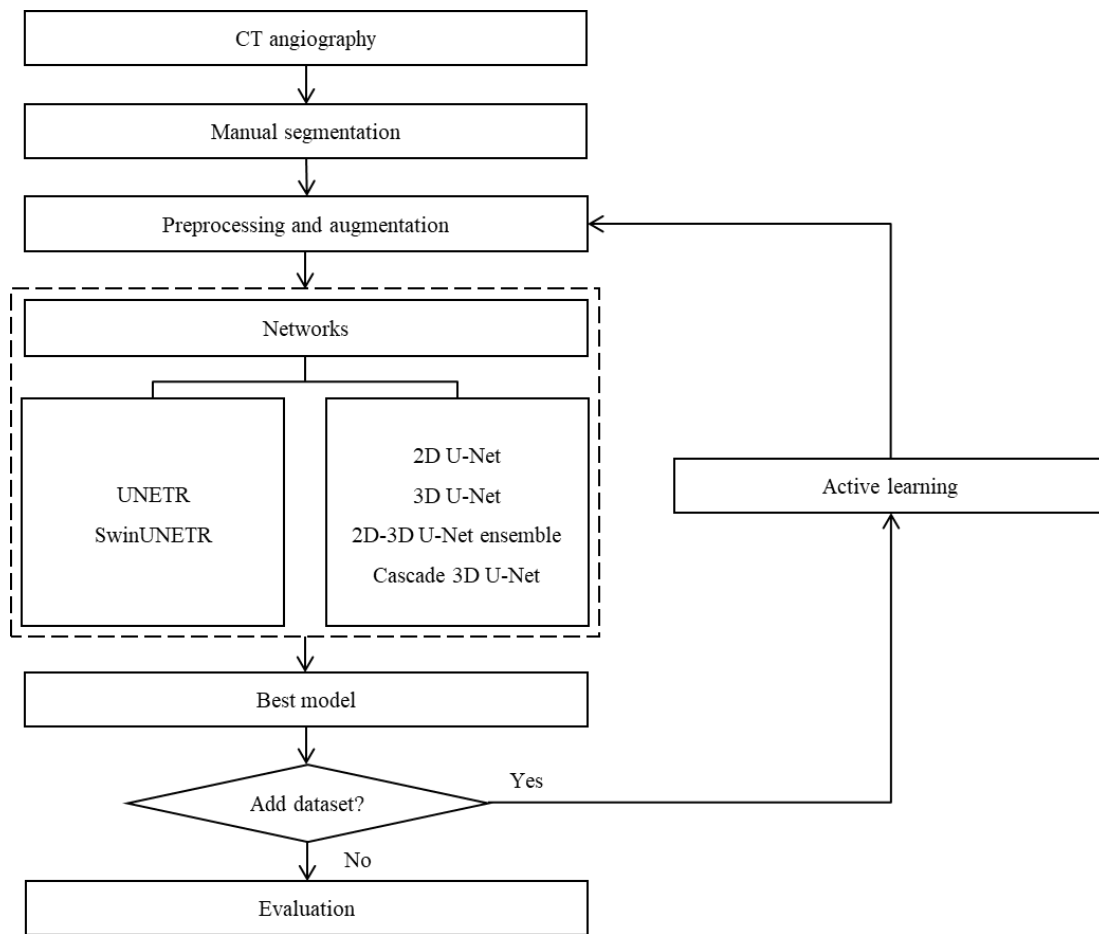


Figure 3-13. Overall flow of thoracoabdominal aortic dissection and abdominal aortic aneurysm for smart labeling with human in the loop in CT angiography.

#### *Manually initial and AL-corrected segmentation*

To perform the initial segmentation, the FOV of the native aorta was positioned using a technique called "*Thresholding*" (Figure 3-2 (A)), and a seed point was selected with 6-connectivity using "*region growing*" (Figure 3-2 (B)). Internal filling was carried out using "*Dilation and Erosion*" under "*Morphology Operations*" to fill the area outside the set hounsfield units (HU) of the native aorta (Figure 3-2 (C)). For segmental arteries with small areas, aneurysms with a small amount of injected contrast medium, and dissection of blood vessel walls, manual segmentation was achieved using the "*Edit Mask*" function (Figure 3-2 (D)). This function was also used to remove any incorrect areas. The method for AL-corrected segmentation involved using the techniques of the initial segmentation to generate predicted binary masks containing the metadata of the original CT image. These masks were



overlaid onto the CT images and manually edited to segment ground truth.

### *Pre-processing*

The raw data was subjected to pre-processing, which involved carrying out the following procedures: (1) normalization, (2) resampling, and (3) augmentation. The z-score normalization was performed to adjust the contrast on CT images, and it was clipped to a value between 0 and 1 for all features as shown in Eq. (5) [126]

$$x_{new} = \frac{x_i - \mu}{\sigma} \quad (5)$$

where  $x_i$ ,  $x_{new}$ ,  $\mu$ , and  $\sigma$  are the original, new images, mean, and standard deviation (SD), respectively. The resampling was performed by resizing the FOV to 256 X 256 X z-axis mm and applying a spacing of 2.0 X 2.0 X 2.0 mm to standardize the spatial properties of the images. MONAI-based augmentation included removal for irrelevant regions such as empty space (foreground), random cropping of 3D patches of 96 X 96 X 96 mm from the input image, random shift intensity, random flip for x-, y-, and z-axes, and 90° random rotation. Augmentation applied to nnU-Net was similar to that of MONAI, including random cropping, random flip and rotation, and random shift intensity, with additional elastic deformation and Gaussian noise.

### *Active learning (AL)*

We divided our 47 subjects into three stages for AL, and the distribution of data for training, validation, and testing for each stage is shown in Figure 3-14. During stage 1, we manually delineated ground truths for initial training, validation, and testing using 15 (11, 2, 2) subjects with two subclasses of the aorta and vessels. For the next stage, ground truths for new data were prepared by manually correcting the results from prediction, referred to as AL-corrected segmentation. In stage 2, we reused the 30 subjects from the previous stage for training with the addition of new data. The results of CNN segmentation for the new data were manually amended for the next stage, as in stage 1. Finally, in stage 3, we used all 47

subjects for training, and the results from all the aforementioned stages were used to evaluate accuracy.

#### *Networks and experimental settings*

The segmentation network utilized a basic U-Net architecture, consisting of an encoder and a decoder. The encoder, composed of convolutional and max pooling layers, down-samples the input image to generate a low-resolution feature map. On the other hand, the decoder up-samples the image to produce an output image of the same size as the input image. The encoder and decoder are connected by skip connections that concatenate the feature maps. The training was performed using a NVIDIA TITAN RTX graphics processing unit (GPU) with 24,220 MiB memory, and the Keras 2.3.0 and Tensorflow 1.15.0 backend were utilized for the training module.

#### *Evaluation*

The accuracy of the predicted label compared to the actual ground truth was assessed using two metrics: the DSC and the 95% HD [127]. The DSC measures the degree of overlap between two volumes, with a range of values from 0 to 1. A value of 0 means that there is no overlap between the volumes, while a value of 1 indicates a complete overlap between the volumes. The calculation of DSC was done using Eq. (2). The 95% HD is a metric that is computed using distances and is expressed in Eq. (4). The 95% HD is a variation of the maximum HD metric. However, it addresses the issue of outliers by taking the 95th percentile of the distances instead of the maximum value. This approach ensures that the metric is not disproportionately affected by a small number of extremely large distances. Furthermore, a stress test was conducted to determine the optimal dataset size for each class.

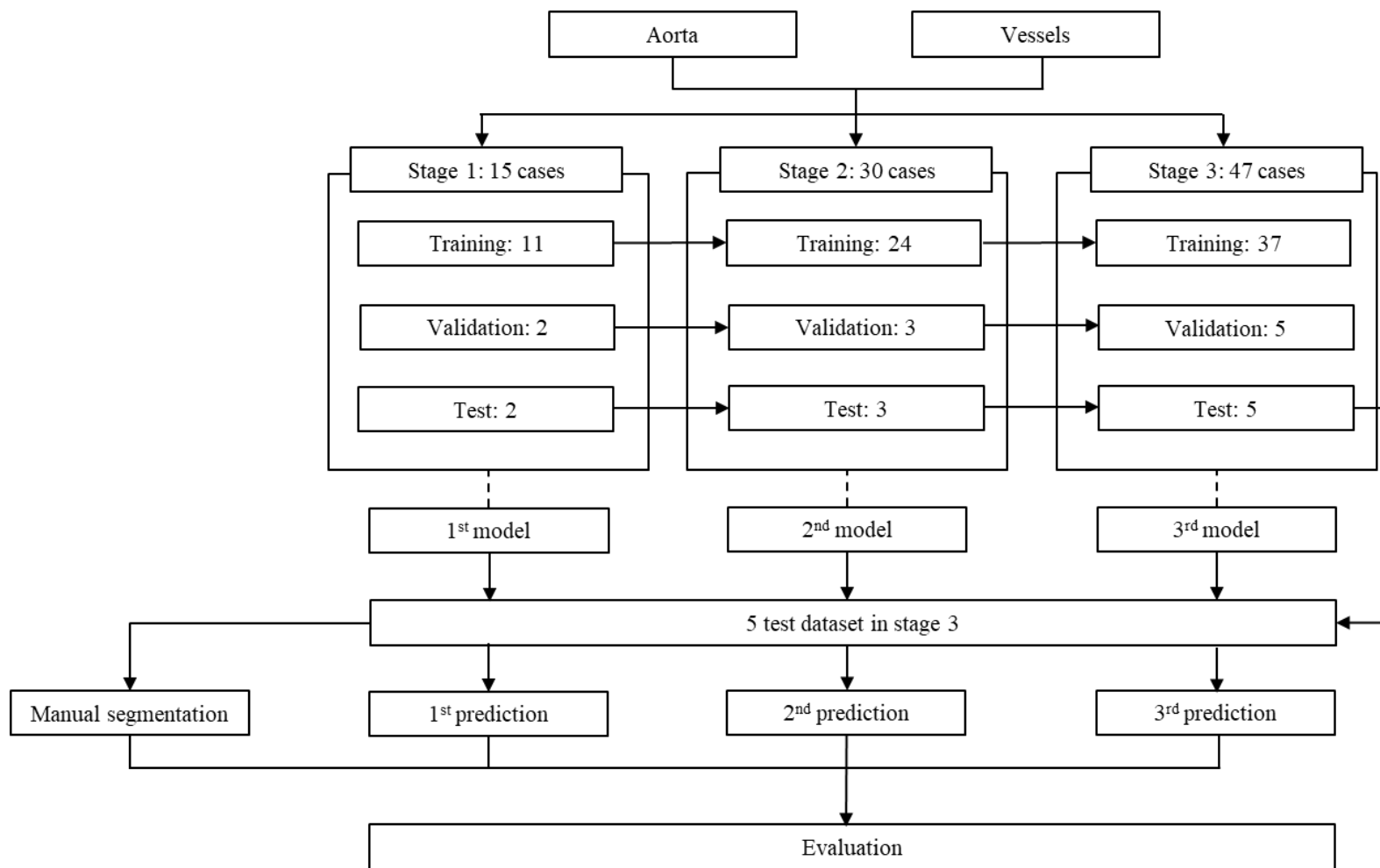


Figure 3-14. Data distribution for thoracoabdominal aortic dissection in each stage for active learning (AL).

## Results

Table 3-6 presents the DSC for each of the two subclasses in each of the three stages for the different networks. The average DSC scores for the two subclasses tended to improve or remain consistent as the stage increased (i.e., as the number of patient data increased), indicating higher or similar performance. The cascade 3D U-Net in Stage 3 achieved the highest accuracy for aorta with  $0.952 \pm 0.008$  and the vessels were  $0.723 \pm 0.008$  in SwinUNETR.

Table 3-6. Dice similarity coefficient for abdominal aortic dissection with UNETR and SwinUNETR of MONAI and 2D U-Net, 3D U-Net, 2D-3D U-Net ensemble, and cascade 3D U-Net of nnU-Net.

Metric	Networks	Classes	Stage 1	Stage 2	Stage 3	
DSC	MONAI	UNETR	Aorta	$0.883 \pm 0.048$	$0.908 \pm 0.025$	$0.898 \pm 0.042$
			Vessels	$0.478 \pm 0.098$	$0.666 \pm 0.098$	$0.609 \pm 0.103$
		SwinUNETR	Aorta	$0.876 \pm 0.034$	$0.920 \pm 0.034$	$0.928 \pm 0.030$
			Vessels	$0.549 \pm 0.126$	$0.683 \pm 0.118$	$0.723 \pm 0.083$
	2D U-Net	Aorta	Aorta	$0.858 \pm 0.165$	$0.869 \pm 0.133$	$0.881 \pm 0.131$
			Vessels	$0.488 \pm 0.122$	$0.555 \pm 0.057$	$0.567 \pm 0.043$
		3D U-Net	Aorta	$0.946 \pm 0.012$	$0.948 \pm 0.012$	$0.951 \pm 0.005$
			Vessels	$0.591 \pm 0.034$	$0.617 \pm 0.057$	$0.615 \pm 0.070$
	2D - 3D U-Net ensemble	Aorta	Aorta	$0.881 \pm 0.137$	$0.938 \pm 0.014$	$0.945 \pm 0.010$
			Vessels	$0.552 \pm 0.066$	$0.608 \pm 0.028$	$0.609 \pm 0.064$
		Cascade 3D U-Net	Aorta	$0.946 \pm 0.012$	$0.931 \pm 0.018$	$0.952 \pm 0.008$
			Vessels	$0.573 \pm 0.025$	$0.608 \pm 0.051$	$0.621 \pm 0.063$

The evaluation of HD is presented in Table 3-7 and the HD values generally showed higher or comparable performance as the stage increased (i.e., as the number of patient data increased). Aorta and vessels achieved the best performance with  $1.859 \pm 0.475$  mm and  $13.707 \pm 7.073$  mm in 3D U-Net of nnU-Net, respectively (Table 3-7).

Table 3-7. 95% Hausdorff distance for thoracoabdominal aortic dissection with UNETR and SwinUNETR of MONAI and 2D U-Net, 3D U-Net, 2D-3D U-Net ensemble, and cascade 3D U-Net of nnU-Net.

Metric	Networks	Classes	Stage 1	Stage 2	Stage 3
MONAI	UNETR	Aorta	6.79 ± 4.08	4.53 ± 1.96	16.33 ± 25.98
		Vessels	16.05 ± 5.47	15.06 ± 6.54	14.88 ± 6.11
	SwinUNETR	Aorta	4.83 ± 1.95	4.09 ± 2.48	3.28 ± 1.67
		Vessels	30.63 ± 10.68	15.04 ± 5.78	14.46 ± 5.23
HD95	2D U-Net	Aorta	44.45 ± 91.48	43.92 ± 89.97	43.29 ± 90.51
		Vessels	15.23 ± 7.18	13.33 ± 2.75	15.05 ± 6.92
	3D U-Net	Aorta	2.23 ± 0.89	2.23 ± 0.89	1.85 ± 0.48
		Vessels	13.13 ± 4.22	12.64 ± 3.99	13.42 ± 7.07
nnU-Net	2D - 3D U-Net ensemble	Aorta	43.14 ± 90.49	2.79 ± 1.02	2.24 ± 0.69
		Vessels	13.63 ± 4.66	13.43 ± 3.96	13.93 ± 7.02
	Cascade 3D U-Net	Aorta	2.37 ± 1.00	3.54 ± 1.68	2.04 ± 0.73
		Vessels	14.40 ± 3.83	14.43 ± 6.96	15.59 ± 11.13

Through the stress test, it was found that the aorta dataset had reached saturation in stage 2 of SwinUNETR, as the difference in DSC was the range of 0.023 to 0.067 between stage 1 with 15 cases and stage 2 with 30 cases and the range of 0.001 to 0.015 between stage 2 and 3 in SwinUNETR, which was a smaller range than vessels. The difference in DSC for vessels between stage 1 and 2 and between stage 2 and 3 ranges from 0.111 to 0.168 and from 0.000 to 0.008, indicating that more datasets are needed to improve performance beyond stage 3 (Table 3-6). The spent time between manual and AL-corrected segmentation for best model (SwinUNETR) reduced  $24.74 \pm 2.33$  min and  $20.85 \pm 4.19$  min, respectively and were statistically significant difference ( $p < 0.05$ ) (Table 3-8).

Table 3-8. The segmentation time for manual and correction using SwinUNETR in thoracoabdominal aortic dissection.

Time	Manual segmentation		AL-corrected segmentation		P
	Aorta	Vessels	Aorta	Vessels	
1	26.53	51.26	5.42	28.68	
2	31.57	53.73	6.22	31.47	
3	29.92	53.43	7.70	33.93	-
4	37.02	39.63	8.12	26.12	
5	34.38	52.40	11.28	26.00	
Mean $\pm$ SD	31.88 $\pm$ 4.04	50.09 $\pm$ 5.93	7.75 $\pm$ 2.26	29.24 $\pm$ 3.45	< 0.05

### 3.4 Abdominal aortic aneurysm in abdominal CT

Abdominal aortic aneurysms (AAA) are an abnormal and degenerative condition where the abdominal region of the aorta becomes pathologically dilated. An AAA is clinically defined when the aortic diameter is more than 50% of the healthy adjacent aorta. If the disease is untreated, AAAs will progressively dilate and eventually rupture, which can result in death. Management of AAAs includes screening, diagnosis, regular surveillance, and timely surgical intervention either through open surgical repair or endovascular stent grafting [128, 129]. There are two important reasons for the need for various measurements of AAA: 1) to diagnose AAA and predict its growth, and 2) to select commercially available endografts that are appropriate for the patient's anatomical size to prevent complication such as endoleak and reintervention after endovascular aneurysm repair (EVAR). First, vascular and endovascular surgeons consider methods for predicting AAA growth to be a research priority [130]. Accurately predicting AAA growth in patients can lead to optimization of surveillance intervals and better timing of surgery. Many studies have emphasized the feasibility of using physiological and biochemical measurements obtained from patients for predicting AAA growth [131-134]. As AAAs enlarge, various geometrical changes occur, such as altered aortic tortuosity and increased aneurysmal asymmetry [135]. Some of these

changes result in a unique non-uniform distribution of wall stress, which can either promote AAA growth deceleration or increase the risk of rupture [136, 137]. Accurately sizing aortic endografts has become increasingly recognized as crucial for achieving optimal early and late outcomes following EVAR of AAA. Inadequate oversizing has been emphasized as a significant risk factor for type I endoleaks [138]. Endograft manufacturers typically recommend an oversize of 10% to 20% greater than the minor axis of the aortic neck, which translates to an endograft that is 3 to 5 mm larger than the adventitia-to-adventitia measurement of the minor-axis aortic neck diameter. However, in certain cases, greater amounts of oversizing have been used for various reasons, such as the belief that larger oversizing could be helpful for treating difficult aortic neck anatomy [139]. The poor interobserver reproducibility of measurements that are considered to be linked to the risk of rupture is a concern. For instance, in 87% of comparisons, the maximum cross-sectional diameter was found to be outside the clinically accepted range of 65 mm of diameter measurement variation [140]. The variability in measurements is likely due to inadequate reporting standards regarding the aortic axis, plane of measurement, and caliper placement. This variability is especially important in a clinical setting because the number of patients who are considered for AAA repair based on a diameter threshold can range from 5% to 24% depending on the radiologist [140]. To address these limitations, we have developed a script-based automated measurement system using a 3D model. In the first phase, we have created an automated segmentation system for AAA.

### *Procedure*

The entire procedure is shown in Figure 3-13 and is similar to the procedure in section 3.3. The initially manually segmentation involved the aorta, thrombus, calcification, and vessels composed of lumbar artery and interior mesenteric artery based on CT angiography. After pre-processing and augmenting the available datasets, various models including UNETR, SwinUNETR, 2D U-Net, 3D U-Net, 2D-3D U-Net ensemble, and cascade 3D U-Net are used for training. If additional datasets are available, the best performing model is used to predict the segmentation of these new CT images, and the AL-corrected segmentation is used to increase the amount of ground truth data. The process of pre-processing, augmentation,

and training is repeated with both the original and added datasets until no more additional datasets are available. Finally, the results obtained from the repeated training are evaluated and analyzed.

### *Dataset*

A total of 300 subjects with AAA were enrolled in AMC between March 2007 and December 2016. All of the participants underwent pre-operative CT angiography with a slice thickness of 2.5 – 5.0 mm, a FOV of 512 X 512 X z-axis, and a pixel size of 0.5781–0.9258 mm. All the participants underwent the EVAR, which inserted the endograft.

### *Manually initial and AL-corrected segmentation*

The initial segmentation was performed by positioning the FOV of the native aorta using "Thresholding" (Figure 3-2 (A)) and selecting a seed point with 6-connectivity using "Region growing" (Figure 3-2 (B)). Internal filling was done using "Dilation and Erosion" under "Morphology Operations" to fill the area outside the HU of the native aorta (Figure 3-2 (C)). For small segmental arteries, aneurysms with a small amount of injected contrast medium, and dissection of blood vessel walls, manual segmentation was done using the "Edit Mask" function (Figure 3-2 (D)). This function was also used to remove any incorrect areas. The AL-corrected segmentation involved using the same techniques as the initial segmentation to generate predicted binary masks with the original CT image metadata. These masks were overlaid onto the CT images and manually edited to create the ground truth segmentation.

### *Pre-processing*

The raw data underwent pre-processing, which involved normalization, resampling, and augmentation. The z-score normalization method was used to adjust the contrast on CT images, and it was clipped to a value between 0 and 1 for all features, as shown in Eq. (1) [126]. To standardize the spatial properties of the images, the FOV was resized to 512 X 512 X z-axis mm and a spacing of 1.0 X 1.0 X 3.0 mm was applied. Both MONAI and nnU-Net frameworks applied similar augmentation techniques, including removal of irrelevant regions, random cropping of 3D patches of 96 X 96 X 96 mm, random intensity shifting,



random flipping for x-, y-, and z-axes, and 90° random rotation. The nnU-Net framework additionally included elastic deformation and Gaussian noise in its augmentation process.

#### *Active learning (AL)*

We divided our 300 subjects into 5 stages for AL, and the distribution of data for training, validation, and testing for each stage is shown in Figure 3-15. During stage 1, we manually delineated ground truths for initial training, validation, and testing using 60 subjects with four subclasses of the aorta, thrombus, calcification, and vessels (48, 6, 6). For the next stage, ground truths for new data were prepared by manually correcting the results from CNN segmentation, referred to as AL-corrected segmentation. In stage 2, we reused the 120 subjects from the previous stage for training with the addition of new data. The results of CNN segmentation for the new data were manually amended for the next stage, as in stage 1. Using the same approach, Stages 3 and 4 are carried out in a similar manner, and finally, in stage 5, we used all 300 subjects for training, and the results from all the aforementioned stages were used to evaluate accuracy.

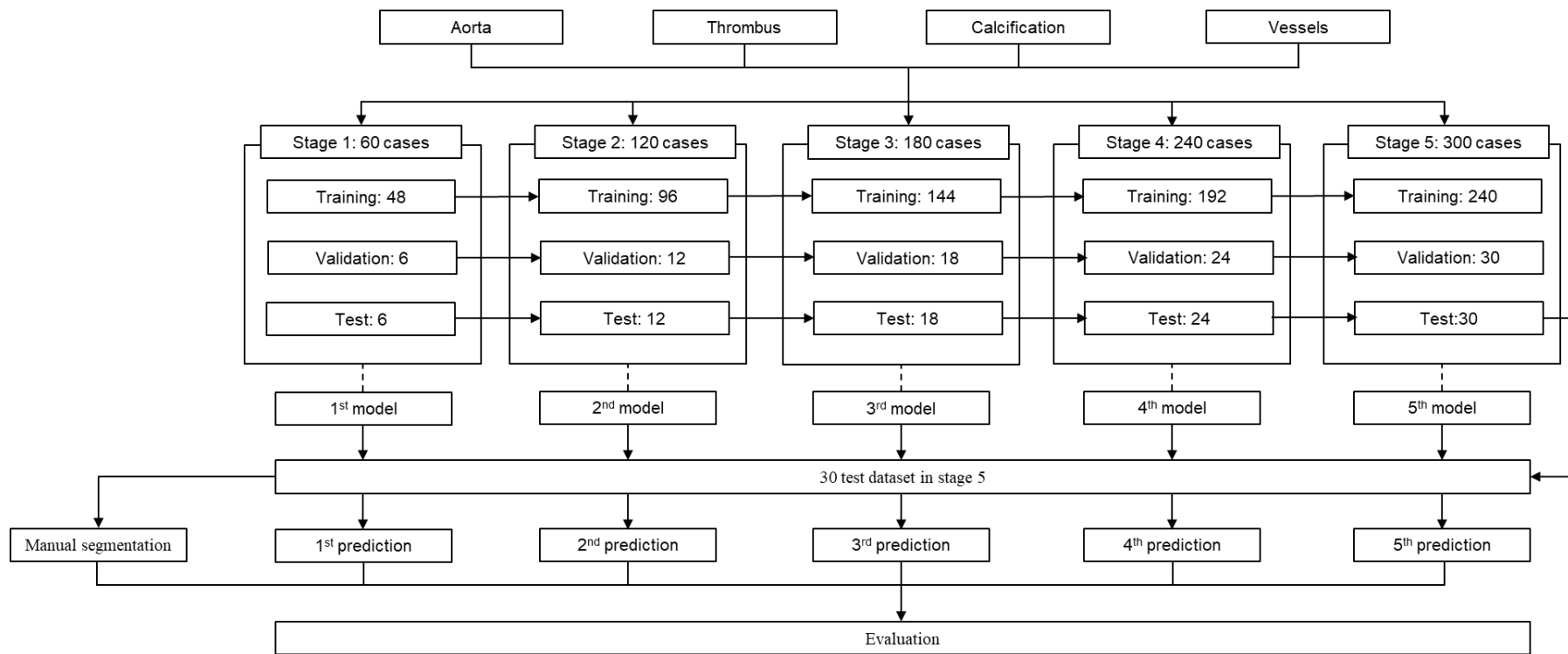


Figure 3-15. Data distribution in each stage for active learning (AL) for abdominal aortic aneurysm.

### *Networks and experimental settings*

The segmentation network employed a simple U-Net architecture, which consisted of an encoder and a decoder. The encoder included convolutional and max pooling layers that down-sampled the input image to generate a low-resolution feature map. The decoder then up-sampled the image to produce an output image with the same dimensions as the input image. The encoder and decoder were connected using skip connections that concatenated the feature maps. Training was carried out on a NVIDIA TITAN RTX GPU with 24,220 MiB memory, utilizing the Keras 2.3.0 and Tensorflow 1.15.0 backend for the training module.

### *Evaluation*

The accuracy of the predicted label compared to the actual ground truth was assessed using two metrics: the DSC and the 95% HD [127]. The DSC measures the degree of overlap between two volumes, with a range of values from 0 to 1. A value of 0 means that there is no overlap between the volumes, while a value of 1 indicates a complete overlap between the volumes. The calculation of DSC was done using Eq. (2). The 95% HD is a metric that is computed using distances and is expressed in Eq. (4). The 95% HD is a variation of the maximum HD metric. However, it addresses the issue of outliers by taking the 95th percentile of the distances instead of the maximum value. This approach ensures that the metric is not disproportionately affected by a small number of extremely large distances. Furthermore, a stress test was conducted to determine the optimal dataset size for each class

### *Results*

Table 3-9 presents the DSC for each of the four subclasses in each of the five stages for the different networks. The average DSC scores for the four subclasses tended to improve or remain consistent as the stage increased (i.e., as the number of patient data increased), indicating higher or similar performance. The nnU-Net outperformed UNETR and SwinUNETR in all stages, and at Stage 5, 2D-3D U-Net ensemble achieved the highest accuracy for aorta and calcification with  $0.928 \pm 0.026$  and  $0.702 \pm 0.226$ , respectively. For cascade 3D U-Net, thrombus achieved the best performance with a score of  $0.782 \pm 0.170$ , while vessels showed the highest accuracy with a score of  $0.481 \pm 0.155$  with 3D U-Net. The

evaluation of HD95 is presented in Table 3-10, and similar to DSC, the HD values generally showed higher or comparable performance as the stage increased (i.e., as the number of patient data increased). Aorta achieved the best performance with  $2.307 \pm 1.42$  mm in 2D-3D U-Net ensemble, while calcification achieved the highest accuracy with  $12.39 \pm 16.62$  mm in 3D U-Net. In contrast to DSC, UNETR showed better performance for thrombus and vessels with scores of  $7.46 \pm 6.12$  and  $11.61 \pm 12.58$  mm, respectively (Table 3-10). Through the stress test, it was found that the aorta dataset had reached saturation in stage 1 of 3D U-Net, as the difference in DSC between Stage 1 with 60 cases and Stage 5 with 300 cases was the range of -0.037 to 0.072 in 3D U-Net, which was a smaller range than other subclasses. For thrombus, the range of differences in DSC between each stage and the previous stage were -0.062 to 0.071, -0.093 to 0.071, -0.019 to 0.071, and -0.316 to 0.119 and for vessels, the range of errors were -0.356 to 0.407, -0.408 to 0.381, -0.247 to 0.236, and -0.267 to 0.347, respectively. Thrombus and vessels exhibited relatively large errors between each stage, and to achieve better performance, more datasets need to be added even after stage 5 using 300 cases. Calcification showed a large range of errors from -0.289 to 0.205, -0.322 to 0.311, and -0.115 to 0.305 until stage 4. However, the error range between stage 4 and 5 was relatively small, ranging from -0.316 to 0.119, indicating that the dataset was saturated at stage 4 using 240 cases. The spent time between manual and AL-corrected segmentation for best model (3D U-Net) reduced  $9.51 \pm 1.02$ ,  $2.09 \pm 1.06$ ,  $1.07 \pm 1.10$ , and  $1.07 \pm 0.97$  min, respectively and were statistically significant difference ( $p < 0.001$ ) (Table 3-11).

Table 3-9. Dice similarity coefficient for abdominal aortic aneurysm with UNETR and SwinUNETR of MONAI and 2D U-Net, 3D U-Net, 2D-3D U-Net ensemble, and cascade 3D U-Net of nnU-Net.

Metric	Networks	Classes	Stage 1	Stage 2	Stage 3	Stage 4	Stage 5	
DSC	MONAI	UNETR	Aorta	$0.890 \pm 0.052$	$0.896 \pm 0.042$	$0.906 \pm 0.039$	$0.910 \pm 0.037$	$0.913 \pm 0.035$
			Thrombus	$0.620 \pm 0.226$	$0.665 \pm 0.235$	$0.676 \pm 0.234$	$0.697 \pm 0.229$	$0.717 \pm 0.195$
			Calcification	$0.584 \pm 0.179$	$0.645 \pm 0.147$	$0.633 \pm 0.182$	$0.664 \pm 0.144$	$0.650 \pm 0.153$
			Vessels	$0.198 \pm 0.150$	$0.312 \pm 0.145$	$0.320 \pm 0.149$	$0.325 \pm 0.143$	$0.343 \pm 0.140$
		SwinUNETR	Aorta	$0.895 \pm 0.050$	$0.904 \pm 0.044$	$0.906 \pm 0.043$	$0.916 \pm 0.039$	$0.920 \pm 0.036$
			Thrombus	$0.660 \pm 0.228$	$0.647 \pm 0.234$	$0.678 \pm 0.235$	$0.710 \pm 0.249$	$0.736 \pm 0.199$
			Calcification	$0.611 \pm 0.114$	$0.612 \pm 0.180$	$0.622 \pm 0.168$	$0.660 \pm 0.157$	$0.669 \pm 0.143$
			Vessels	$0.240 \pm 0.157$	$0.314 \pm 0.159$	$0.358 \pm 0.140$	$0.368 \pm 0.147$	$0.364 \pm 0.149$
	2D U-Net	Aorta	$0.899 \pm 0.035$	$0.902 \pm 0.038$	$0.911 \pm 0.036$	$0.919 \pm 0.027$	$0.922 \pm 0.027$	
		Thrombus	$0.710 \pm 0.206$	$0.699 \pm 0.260$	$0.744 \pm 0.200$	$0.752 \pm 0.227$	$0.750 \pm 0.223$	
		Calcification	$0.593 \pm 0.214$	$0.605 \pm 0.138$	$0.670 \pm 0.230$	$0.693 \pm 0.230$	$0.687 \pm 0.230$	
		Vessels	$0.319 \pm 0.142$	$0.294 \pm 0.143$	$0.394 \pm 0.185$	$0.395 \pm 0.196$	$0.430 \pm 0.186$	
		3D U-Net	Aorta	$0.914 \pm 0.035$	$0.913 \pm 0.037$	$0.909 \pm 0.039$	$0.918 \pm 0.038$	$0.926 \pm 0.027$
			Thrombus	$0.733 \pm 0.229$	$0.737 \pm 0.228$	$0.746 \pm 0.228$	$0.758 \pm 0.230$	$0.779 \pm 0.191$
			Calcification	$0.674 \pm 0.218$	$0.602 \pm 0.161$	$0.665 \pm 0.237$	$0.703 \pm 0.199$	$0.702 \pm 0.210$
			Vessels	$0.310 \pm 0.147$	$0.374 \pm 0.168$	$0.437 \pm 0.206$	$0.441 \pm 0.191$	$0.481 \pm 0.156$
	nnU-Net	Aorta	$0.911 \pm 0.032$	$0.910 \pm 0.039$	$0.913 \pm 0.035$	$0.922 \pm 0.029$	$0.928 \pm 0.026$	
		2D - 3D U-Net ensemble	Thrombus	$0.732 \pm 0.202$	$0.730 \pm 0.239$	$0.762 \pm 0.193$	$0.764 \pm 0.226$	$0.769 \pm 0.215$
			Calcification	$0.643 \pm 0.222$	$0.636 \pm 0.133$	$0.690 \pm 0.233$	$0.708 \pm 0.224$	$0.702 \pm 0.226$
			Vessels	$0.320 \pm 0.151$	$0.345 \pm 0.161$	$0.411 \pm 0.203$	$0.425 \pm 0.195$	$0.453 \pm 0.185$
Cascade 3D U-Net	Aorta	$0.914 \pm 0.034$	$0.916 \pm 0.035$	$0.916 \pm 0.035$	$0.919 \pm 0.033$	$0.926 \pm 0.028$		
	Thrombus	$0.746 \pm 0.189$	$0.748 \pm 0.227$	$0.775 \pm 0.178$	$0.756 \pm 0.230$	$0.782 \pm 0.170$		
	Calcification	$0.600 \pm 0.228$	$0.680 \pm 0.219$	$0.674 \pm 0.226$	$0.710 \pm 0.216$	$0.652 \pm 0.244$		
	Vessels	$0.354 \pm 0.142$	$0.420 \pm 0.165$	$0.444 \pm 0.156$	$0.469 \pm 0.189$	$0.473 \pm 0.171$		

Table 3-10. 95% Hausdorff distance for abdominal aortic aneurysm with UNETR and SwinUNETR of MONAI and 2D U-Net, 3D U-Net, 2D-3D U-Net ensemble, and cascade 3D U-Net of nnU-Net.

Metric	Networks	Classes	Stage 1	Stage 2	Stage 3	Stage 4	Stage 5	
HD95	MONAI	UNETR	Aorta	6.66 ± 7.70	4.07 ± 5.61	3.95 ± 5.29	3.48 ± 5.00	3.77 ± 5.97
			Thrombus	12.41 ± 17.78	12.24 ± 17.79	12.66 ± 18.28	10.30 ± 9.28	7.33 ± 6.16
			Calcification	29.77 ± 12.51	21.61 ± 8.02	19.59 ± 7.68	20.11 ± 8.02	20.13 ± 7.29
			Vessels	14.88 ± 12.68	11.45 ± 14.10	12.92 ± 15.65	12.90 ± 14.90	11.57 ± 12.54
	SwinUNETR	Aorta	5.22 ± 8.61	3.913 ± 6.84	4.35 ± 5.73	2.83 ± 5.06	2.41 ± 3.84	
		Thrombus	10.39 ± 11.19	12.30 ± 11.32	15.03 ± 16.39	11.51 ± 13.29	8.96 ± 9.43	
		Calcification	22.90 ± 10.73	25.23 ± 12.62	17.49 ± 5.34	17.73 ± 6.73	17.09 ± 8.12	
		Vessels	13.53 ± 13.98	12.24 ± 12.49	16.27 ± 25.15	12.07 ± 12.54	12.47 ± 14.62	
	2D U-Net	Aorta	5.32 ± 7.97	3.110 ± 2.163	2.744 ± 1.51	2.70 ± 1.95	3.15 ± 3.70	
		Thrombus	14.20 ± 12.95	15.48 ± 20.30	15.89 ± 26.02	14.79 ± 21.56	14.27 ± 18.34	
		Calcification	22.30 ± 18.64	15.82 ± 13.96	14.21 ± 18.80	14.33 ± 18.92	14.20 ± 18.83	
		Vessels	38.90 ± 21.55	24.98 ± 11.26	36.48 ± 21.39	38.53 ± 23.86	32.30 ± 19.25	
	3D U-Net	Aorta	2.77 ± 2.28	2.00 ± 1.28	3.72 ± 5.75	3.30 ± 5.72	2.89 ± 2.76	
		Thrombus	17.28 ± 21.89	12.74 ± 16.38	18.85 ± 22.96	17.59 ± 26.29	12.3 ± 17.02	
		Calcification	13.24 ± 17.02	13.14 ± 13.38	23.78 ± 33.36	12.46 ± 15.02	12.39 ± 16.62	
		Vessels	46.72 ± 24.23	19.95 ± 11.21	24.65 ± 16.44	25.70 ± 16.72	23.38 ± 16.20	
2D - 3D U-Net ensemble	Aorta	3.10 ± 2.55	2.22 ± 1.54	2.47 ± 1.41	2.18 ± 1.26	2.297 ± 1.42		
	Thrombus	14.20 ± 13.55	14.19 ± 20.18	15.31 ± 21.84	16.04 ± 23.10	14.05 ± 18.41		
	Calcification	15.64 ± 18.42	13.20 ± 13.85	14.55 ± 18.51	13.60 ± 19.09	13.25 ± 18.66		
	Vessels	45.65 ± 25.27	28.29 ± 20.94	35.35 ± 25.07	36.10 ± 30.47	33.24 ± 26.08		
Cascade 3D U-Net	Aorta	2.55 ± 1.45	2.41 ± 1.35	2.60 ± 1.72	2.487 ± 1.71	2.69 ± 2.47		
	Thrombus	13.55 ± 14.10	18.76 ± 23.43	13.81 ± 18.05	17.50 ± 25.00	11.62 ± 13.02		
	Calcification	32.74 ± 42.83	15.99 ± 18.83	16.95 ± 25.19	12.01 ± 17.71	59.69 ± 67.15		
	Vessels	31.45 ± 17.31	35.84 ± 20.64	23.82 ± 14.93	17.65 ± 12.17	20.62 ± 11.93		

Table 3-11. The segmentation time for manual and correction using 3D U-Net of nnU-Net in abdominal aortic aneurysm.

Time	Manual				nnU-Net (Best model)				P
	Aorta	Thrombus	Calcification	Vessels	Aorta	Thrombus	Calcification	Vessels	
1	23.43	7.20	6.93	5.38	12.58	4.43	3.75	4.73	
2	20.95	7.55	5.70	6.63	12.10	3.32	3.82	5.38	
3	22.43	7.78	6.52	6.20	13.33	5.12	4.40	4.83	
4	21.30	6.68	5.17	5.72	11.57	4.37	4.72	4.80	
5	22.72	5.87	5.47	6.35	13.12	4.50	5.78	4.53	
6	23.85	6.42	4.52	5.15	12.33	3.68	4.77	4.53	-
7	22.25	6.55	5.27	5.03	13.05	4.32	4.73	5.52	
8	21.45	5.47	6.00	5.48	13.63	4.57	3.98	5.82	
9	21.23	5.32	5.53	6.42	11.42	4.87	5.08	4.10	
10	20.85	5.40	5.57	7.33	12.22	4.20	4.95	4.73	
Mean ± SD	22.05 ± 1.06	6.42 ± 0.90	5.67 ± 0.69	5.97 ± 0.74	12.53 ± 0.74	4.34 ± 0.52	4.60 ± 0.62	4.90 ± 0.51	< 0.001

## **4 Semi-automated design and measurement with application programming interface (API) of computer aided design (CAD)**

### **4.1 Aortic graft reconstruction guides in thoracoabdominal aortic dissection**

Regarding the automation of segmentation using DL, the octopod technique has been proposed for reconstructing grafts in cases of thoracoabdominal aortic dissection. The traditional approach, which relies on images, has drawbacks when it comes to precisely positioning the branching grafts. This is because it is typically dependent on the skill of the operating surgeon. To overcome this limitation, we developed a patient-specific graft reconstruction guide [124, 125] and introduced an automated CAD modeling as the second step.

#### *Procedure*

The process for this retrospective study is illustrated in Figure 4-1. The native aorta was segmented using thoracoabdominal CT angiography and divided into two types of patient-specific graft reconstruction guides. These included visualizing and marking guides created using STL format, which were generated using both conventional and automatic modeling methods. The accuracy and CAD modeling time of both the conventional and automatic modeling methods were compared and evaluated to assess the effectiveness of the automated modeling approach.



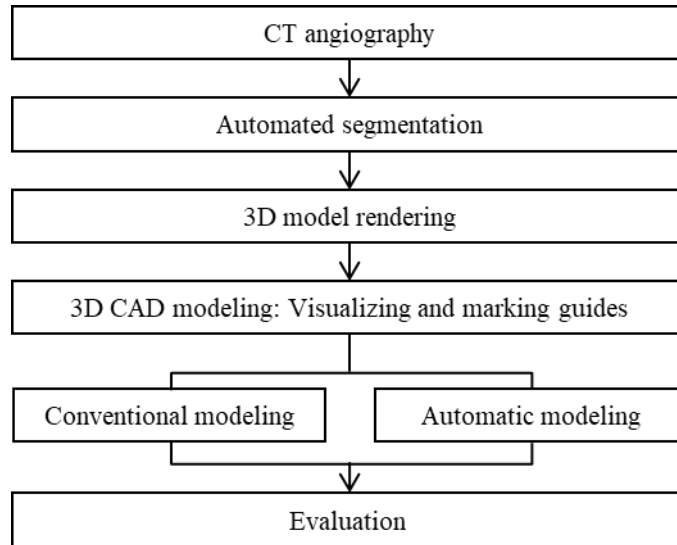


Figure 4-1. Overall procedure for the evaluation of two types of patient-specific graft reconstruction guides consisting of visualizing and marking guides for aortic dissection and comparison between conventional and automatic modeling methods.

#### *Dataset*

The CT images used in the study were acquired from a total of 10 patients who had been diagnosed with either six Crawford extent II or four Crawford extent III thoracoabdominal aortic dissection and were admitted to AMC between June 2018 and February 2020. Of the 10 patients, nine were male and one was female, with an average age of  $41.10 \pm 14.01$  years (ranging from 22 to 65 years). All of the patients underwent CT angiography scans (Siemens SOMATOM series; Siemens AG, Munich, Germany) with a tube voltage range of 70–120 kVp and a slice thickness of 0.6 – 3.0 mm. The graft reconstruction was performed on the main aorta, which extended from the left subclavian artery to the infrarenal abdominal aorta, as well as the bilateral common iliac artery and segmental arteries located between the thoracic-8 and lumbar-4 levels. The patient information, including their respective segmental arteries, is presented in Table 4-1.

Table 4-1. Ten patients' profiles for thoracoabdominal aortic dissection, including classification, level of segmental arteries, and range of graft reconstruction. Note. T, thoracic; L, lumbar; Rs, right side; Ls, left side; CIA, common iliac artery; LSA, left subclavian artery; IMA, inferior mesenteric artery; RA, renal artery.

Patients No.	Age	Classification (Crawford extent)	Level of segmental arteries			Range of graft reconstruction
			Side	T	L	
1	37	II	Rs	11, 12	-	T-11 to bilateral CIA
			Ls	11		
2	46	II	Rs	11, 12	-	LSA to bilateral CIA
			Ls			
3	33	II	Rs	8, 9	-	LSA to IMA
			Ls			
4	22	II	Rs	10, 11, 12	-	LSA to RA
			Ls			
5	65	III	Rs	10	-	T-10 to bilateral CIA
			Ls	11		
6	51	III	Rs	10, 11	1	LSA to bilateral CIA
			Ls	10	1	
7	57	III	Rs	10, 12	-	LSA to RA
			Ls	9, 10, 12		
8	22	II	Rs	9, 10, 12	1, 4	T-9 to bilateral CIA
			Ls	11, 12	1	
9	38	III	Rs	7, 8, 10, 11, 12	1, 3	T-7 to bilateral CIA
			Ls	7, 8, 9, 10, 11, 12	-	
10	40	II	Rs	8, 10, 12	2, 3, 4	LSA to bilateral CIA
			Ls	8, 11	3, 4	

#### *Conventional CAD modelling method*

There were two different types of guides used for patient-specific graft reconstruction. The first type was a visualizing guide that provided a realistic representation of the aortic graft, showing the main aortic body and major blood vessels including segmental arteries. The second type was a marking guide that replaced the vessels in the visualizing guide with protruding marking regions that could be detected by touch. The patient's native aorta was

automatically segmented using CT angiography images (Figure 4-2 (A)). In traditional CAD modeling, a centerline (represented by a black line) was generated for the main and vascular graft using the "*Create Center Line*" function. This process involved using predetermined parameters such as a segment length of 0.30 mm and an accuracy detail of 1.00 mm from the 3D model of the patient's aorta. The centerline included the major blood vessels and segmental arteries, both thoracic and lumbar. The segment length referred to the length of each individual section of the center line. Meanwhile, the accuracy detail was a measure of the precision of the center line, with lower values indicating higher accuracy. The "*Smooth Curve*" function was then used on the center line of the main graft, with predefined parameters that included a 0.7 factor controlling the strength of smoothing and 1000 iterations to achieve the desired level of smoothness. The process of smoothing was also applied to the smoothing algorithm represented by the green line (Figure 4-2(A)). In addition, the center lines of the vascular grafts were established with a similar smoothing factor and a lower number of iterations, specifically 50 iterations as indicated by the blue line (Figure 4-2 (B)). To create the main graft, the "*Sweep*" function was utilized. This involved connecting the center line and a sketch plane to that of the main graft. A new sketch plane was created using the "*New Sketch*" function, and a circle with a diameter ranging from 22.0 to 30.0 mm was drawn on it using the "*Create Circle*" function. The diameter of the circle was determined by the surgeons. Similarly, the vascular grafts that were required for the reconstruction were created with a fixed size of 8 mm (Figure 4-2 (C)). To create one part of the visualizing guide, the main graft was combined with the vascular grafts using the "*Boolean Union*" function (Figure 4-2 (D), right). In the marking guide, the main graft was modified by protruding corresponding surfaces between the main and vascular grafts to detect the position of the visceral and segmental arteries. This was achieved using the "*Move Surface*" function with specific parameters such as automatic directions per surface, a distance of 2.00 mm, and a solid shape. The automatic directions were indicated to the direction of movement, which was normal to each surface (Figure 4-2 (D), left). The visualizing and marking guides were implemented by internally emptying using the "*Hollow*" function with specific parameters. The inside of the hollow type was chosen, with a distance of 5.00 mm and the smallest detail of 0.30 mm, determined empirically. The

hollow type selected was an existing surface assumed to have been constructed either inside or outside. Furthermore, the distance of the hollow type was specified to determine the thickness of the parts, while the smallest detail referred to the size of the triangles on the newly generated surfaces. Two virtual planes that defined the extent of thoracoabdominal aortic dissection were established based on medical images. To trim the two types of patient-specific graft reconstruction guides, the "Cut" function was utilized (Figure 4-2 (E)). After the completion of the main part, the remaining unwanted noise shells were eliminated using the "Filter Small Shells" function. The parameters for this function were determined empirically, with a 90% area and volume threshold. All shells with areas and volumes smaller than the main part were eliminated using relative values. Finally, the visualizing and marking guides underwent a smoothing process using the "Smooth" function, with the strength of the smoothing determined by an empirically determined factor of 0.7. The modeling process was then finalized with a thorough inspection of the parts (Figure 4-2 (F)).

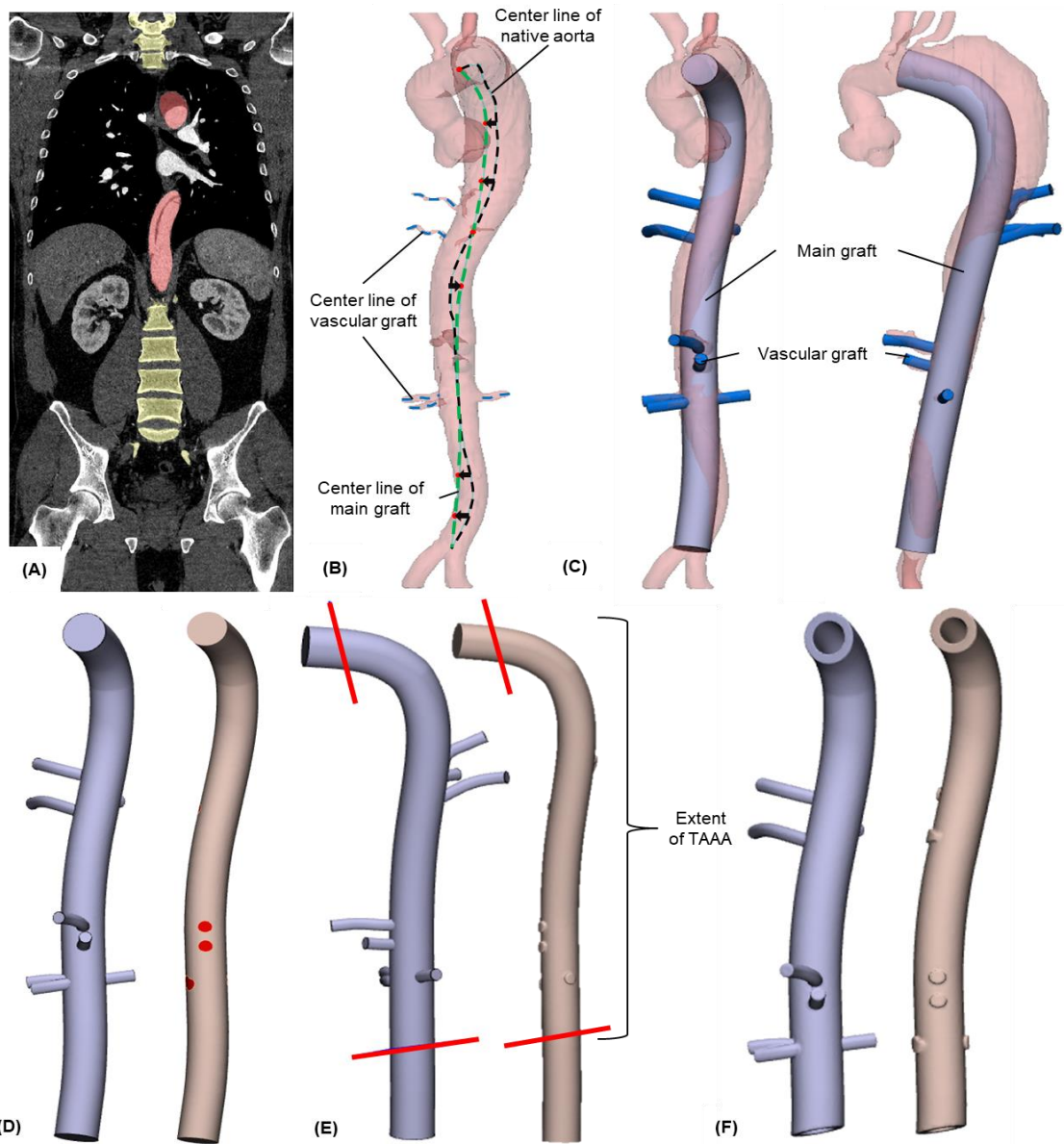


Figure 4-2. The conventional modeling method for patient-specific visualizing and marking guides. (A) Automated segmentation of thoracoabdominal aorta, including major blood vessels in the CT angiography images. (B) The extracting center line of the native aorta (black line) and the smoothed center line of the main (green line) and vascular grafts (blue line). (C) Designing the main and vascular grafts. (D, left) Combination of the main and vascular grafts for the visualizing guide and (D, right) the protrusion toward the corresponding surfaces between the main and vascular grafts. (E) Creation of two virtual planes to determine the extent of the thoracoabdominal aortic dissection and trimming of the model. (F, left) Completion of visualizing and (F, right) marking guides.

### *Automated modeling programming*

The automatic guide modeling program for designing the visualizing and marking guides was developed using Python coding and API (Algorithm 4-1). The program required four inputs: the number of center lines for the main and vascular grafts, the diameter of the aorta, the type of graft reconstruction guide, and the save path for two virtual planes that determined the extent of the thoracoabdominal aortic dissection. The part inspection step in the module defined as a new function that included the "*Filter Small Shells*", "*Adaptive Remesh*", and "*Auto Fix*" functions (Algorithm 4-2). Without filtering unnecessary noise shells before part fix, the process would take an infinite or long time. Furthermore, irregularly sized triangle structures could result in low accuracy if remesh was not applied. To enhance modeling performance, the software was executed on a system with an NVIDIA GTX 1080 Ti GPU, an Intel Core i7-6700 central processing unit with a clock speed of 3.40 GHz, 32 GB of memory, and a 64-bit Windows 10 operating system. To run and debug the program efficiently, PyCharm, an external integrated development environment, was employed.

Algorithm 4-1. Automated modeling method for the visualizing guide and marking guide.

---

**Input:** Number of center line for the main and vascular grafts (N), Diameter of aorta (D), Type of graft reconstruction guide (T),  
Save path of two virtual plane to determine the extent of the thoracoabdominal aortic dissection (S)

**Output:** Visualizing guide or Marking guide

Set native aorta model with center line for the main and vascular grafts  
Find the center line of the main and vascular grafts

**For**  $i \leftarrow 0$  to  $N-1$

**If** the center line of the main and vascular grafts is the longest  
Apply “*Curve smooth*” function with smooth 0.7 factor and 1000 iterations  
Create the sketch with circle of D  
Perform the “*Sweep*” function with center line and sketch  
Print “Establishment of main graft”

**Else**  
    Apply “*Curve smooth*” function with smooth 0.7 factor and 50 iterations  
    Create the sketch with a circle with a diameter of 8 mm  
    Perform the “*Sweep*” function with the center line and sketch  
    Print “Establishment of vascular graft”

**End if**

**End for**

**If**  $T ==$  Visualizing guide  
Combine the main graft and vascular graft using the “*Union*” function  
Print “Visualizing guide”

**Else**  
Find the corresponding surfaces between the main graft and vascular graft  
Add the corresponding, protruding surfaces with a distance of 2.0 mm and a solid shape using the “*Move surface*” function  
Print “Marking guide”

**End if**  
Add internal emptying using the “*Hollow*” function with the distance of 5.00 mm and smallest detail of 0.30 mm  
Import S  
Trim the graft reconstruction guide into two planes using the “*Cut*” function  
Find the volume of the cutting parts  
**If** the volume is the largest  
    Perform the “*smooth*” function with 0.7 factor

**Apply the part inspections (Algorithm 2)**

**Else**  
    Remove the parts using the “*Filter Small Shells*” function with 90% area and volume threshold

---

Algorithm 4-2. The module for part inspection.

---

**Function:** Part inspection

**Input:** Incomplete model

**Output:** Fixed model

Remove the unnecessary noise shells using the “*Filter Small Shells*” function with 15% area and volume threshold

Arrange irregular meshes using the “*Adaptive remesh*” function with a triangle length of 2.0 mm

Fix the incomplete model using the “*Auto Fix*” function

**return** Fixed model

---

### *Evaluation*

To evaluate the performance of the automatic modelling method for the visualizing and marking guides, its accuracy and modelling time were compared with those of the conventional modelling method. The accuracy was evaluated by calculating the absolute mean differences between the two methods using HD based on points with a difference map using Eq. 3. The statistical significance of the differences between the two methods was determined using the Wilcoxon signed-rank test.

### *Results*

Table 4-2 summarizes the results of the comparison between the conventional and automatic modeling methods. The table 4-2 shows the absolute mean differences between the two methods and the number of corresponding points belonging to the smallest distance determined by HD for each patient's visualizing and marking guides. The results indicate that the absolute mean differences between the conventional and automated methods were  $6.05 \pm 4.86 \mu\text{m}$  for the visualizing guide and  $5.51 \pm 4.85 \mu\text{m}$  for the marking guide. The number of corresponding points for the smallest distance was 82,459 and 57,029 points for the visualizing and marking guides, respectively.



Table 4-2. Hausdorff average distance of corresponding points between conventional and automated modeling methods for each patient with visualizing and marking guides. Note: CP, corresponding point.

Patients No.	Visualizing guide			Marking guide		
	Distance ( $\mu\text{m}$ )	Max ( $\mu\text{m}$ )	# of CPs	Distance ( $\mu\text{m}$ )	Max ( $\mu\text{m}$ )	# of CPs
1	$5.74 \pm 4.66$	45.29	5,997	$5.27 \pm 4.30$	48.15	5,367
2	$5.41 \pm 4.31$	46.97	10,112	$5.08 \pm 4.00$	41.85	6,787
3	$5.60 \pm 4.47$	46.13	8,278	$5.28 \pm 4.50$	47.58	6,129
4	$6.05 \pm 4.92$	44.58	7,751	$6.15 \pm 5.35$	47.03	5,919
5	$5.90 \pm 4.75$	43.61	7,998	$5.22 \pm 4.32$	36.00	4,686
6	$5.96 \pm 4.81$	40.78	6,576	$5.25 \pm 4.58$	44.83	3,905
7	$6.10 \pm 5.27$	42.98	4,643	$5.76 \pm 5.03$	39.39	3,322
8	$5.89 \pm 4.83$	50.10	8,497	$5.36 \pm 4.62$	41.81	5,433
9	$6.57 \pm 4.99$	41.26	11,989	$6.49 \pm 6.26$	170.83	6,953
10	$5.63 \pm 4.69$	48.21	10,618	$5.22 \pm 4.78$	162.09	7,629

Figure 4-3 shows a comparison of color maps between the conventional and automatic models, along with the absolute mean difference calculated using Hausdorff average distance.

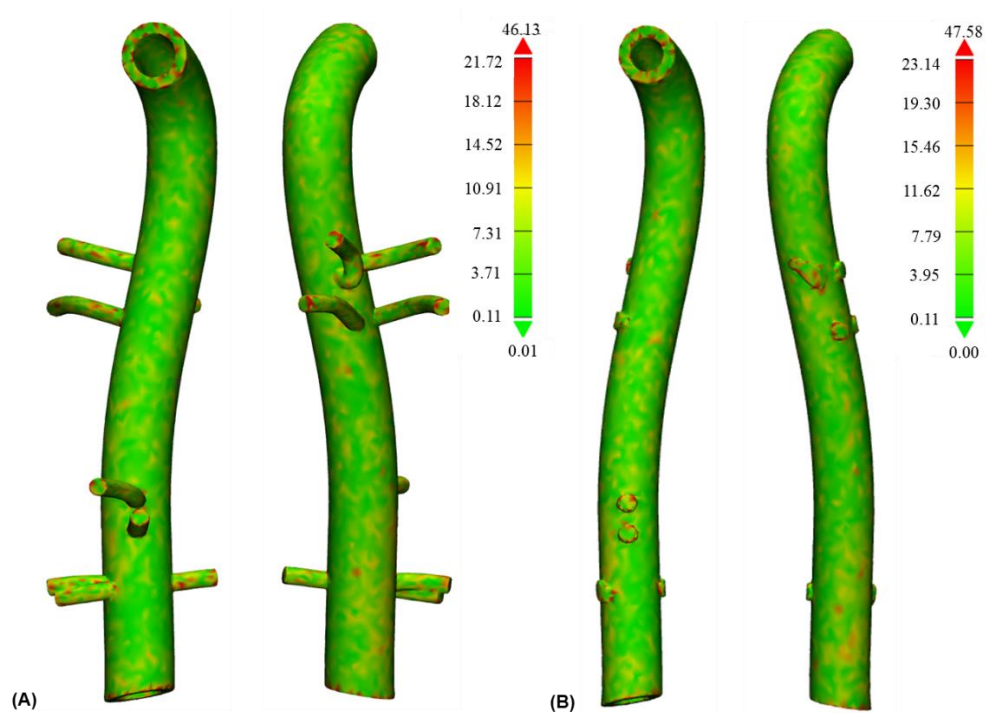


Figure 4-3. Comparison of the aligned difference map is shown with the absolute mean differences in the areas between conventional and automated modeling methods with (A) visualizing and (B) marking guides.

The automated modeling method significantly reduced the modeling time for both the visualizing and marking guides. The visualizing guide was modeled in  $26.70 \pm 5.55$  min, which was thirty times faster than the conventional method ( $p < 0.001$ ), and the marking guide was modeled in  $31.32 \pm 5.85$  min, which was forty times faster ( $p < 0.001$ ). The automatic modeling time ranged from 20.72 min to 43.33 min (Table 4-3).





Table 4-3. Modeling time for conventional and automated modeling methods with two types of patient-specific graft reconstruction guides.

Patients No.	Visualizing guide(min)		Marking guide (min)		P
	Conventional modeling	Automated modeling	Conventional modeling	Automated modeling	
1	21.48	0.93	29.87	0.72	
2	23.03	0.98	27.02	0.82	
3	22.50	0.85	25.53	0.80	
4	21.57	0.72	29.57	0.72	
5	32.13	1.72	28.13	0.85	
6	21.52	0.60	28.60	0.58	-
7	27.18	0.60	33.82	0.58	
8	30.98	0.87	35.42	0.95	
9	38.97	1.07	44.50	1.15	
10	30.98	1.08	38.75	0.87	
Mean ± SD	27.63 ± 5.70	0.92 ± 0.31	32.11 ± 5.95	0.80 ± 0.17	<0.001

## 4.2 Landmark measurement in abdominal aortic aneurysm

There are two significant reasons why it is essential to measure the clinically defined landmarks of AAA. Firstly, to monitor and follow up the growth of AAA over time. Secondly, to choose the appropriate commercially available endografts that fit the patient's anatomical size to avoid complications like endoleak and reintervention after EVAR (Table 4-4). The inconsistency in AAA measurements can be attributed to insufficient guidelines for reporting standards regarding the aortic axis, measurement plane, and placement of calipers. This variability becomes particularly significant in a clinical setting because the number of patients who qualify for AAA repair based on a specific diameter threshold can vary widely, ranging from 5% to 24%, depending on the radiologist [140]. In order to address these limitations, we utilized DL in section 3.2 to automate the segmentation process and leveraged the resulting 3D model created through rendering to introduce automated CAD measurements using a script-based approach with an API.

Table 4-4 Manufacturer’s guideline of patient selection for EVAR [141] .

Parameters	Neck angle	Neck diameter	Neck length	CIA diameter	CIA length	Femoral artery diameter
 AneuRx	$\leq 45^\circ$	18 – 25.5 mm	$\geq 15$ mm	10 – 21 mm	$\geq 25$ mm	$\geq 8$ mm
 Talent	$\leq 60^\circ$	13 – 32 mm	$\geq 10$ mm	8 – 22 mm	$\geq 15$ mm	$\geq 8$ mm
 Zenith	$\leq 60^\circ$	18 – 28 mm	$\geq 15$ mm	7.5 – 20 mm	$\geq 10$ mm	$\geq 8$ mm
 Excluder	$\leq 60^\circ$	19 – 29 mm	$\geq 15$ mm	8 – 18.5 mm	$\geq 10$ mm	$\geq 8$ mm

### Procedure

In this retrospective study, the process was illustrated in Figure 4-1, where aortic pathologies were segmented using CT angiography. We performed automated measurements using a script-based approach that utilized clinically defined landmarks on the 3D model obtained through rendering. The accuracy of the automated measurements was compared to the conventional manual measurement method by medical doctors using CT images. In addition, we evaluated the efficiency of the automated measurements.

### Dataset

The pre-operative CT images from a total of 96 patients who had been diagnosed with AAA and underwent EVAR were enrolled in AMC between March 2007 and March 2021.

Of the 96 patients, 88 were male and 8 were female, with an average age of  $70.10 \pm 7.26$  years (ranging from 51 to 88 years). CT angiography scans were performed on all patients using a tube voltage range of 120 kVp, pixel size of 0.5781 – 0.8164 mm, and a slice thickness of 2.5 – 5.0 mm.

*landmark*

To select commercially available endografts that are appropriate for a patient's anatomical size and prevent complications such as endoleak after EVAR, 7 landmarks were defined as follows: 1) aortic neck diameter, 2) aortic aneurysm diameter, 3) right iliac artery diameter, 4) left iliac artery diameter, 5) aortic neck length, 6) common iliac artery tortuosity, and 7) aortic neck angulation. These landmarks were chosen to predict the growth of AAA and to ensure appropriate selection of endografts. (Figure 4-4)

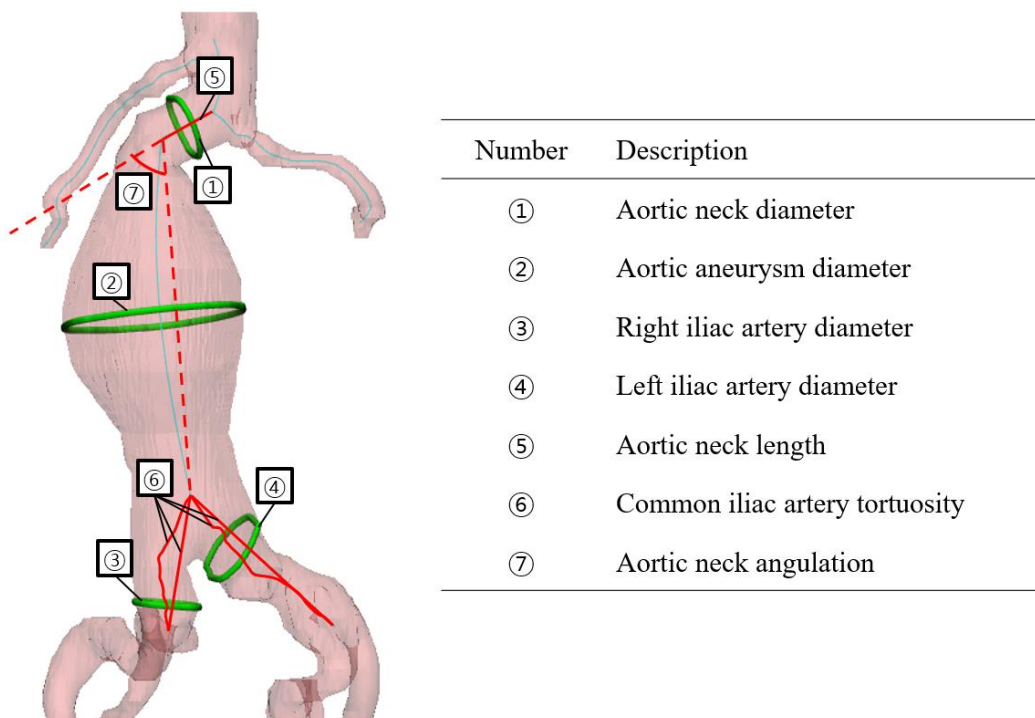


Figure 4-4. The clinical defined measurement landmarks for AAA models.

### *Conventional image-based measurement*

The diameters and lengths of the proximal aortic neck, aortic aneurysm and both common iliac arteries, which are morphological characteristics of the aneurysm, were measured using digital calipers on a picture archiving and communication system (PACS) workstation. The maximum aortic diameters were measured on axial view and the lengths were measured on either sagittal or coronal images. The digital goniometer was used to determine the infrarenal neck angulation, which was measured in degrees (Figure 4-5).

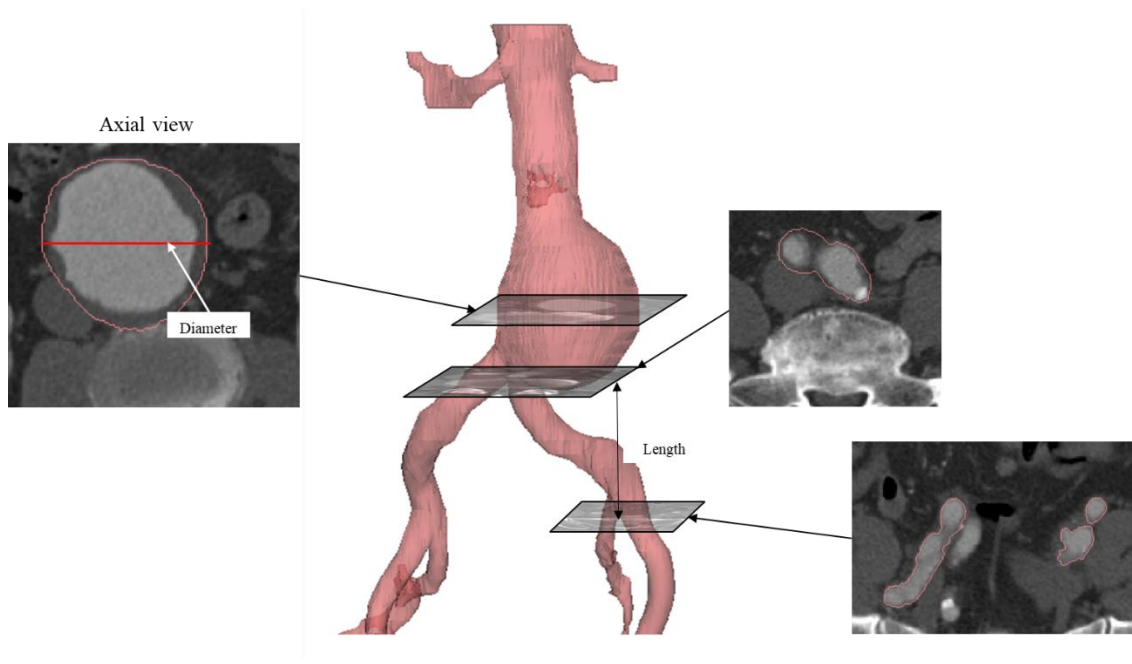


Figure 4-5. Conventional image-based measurement.

### *Automated modeling programming*

For automated measurements in AAA, two modules were developed, which were used as the basis for most of the landmark measurements. Module 1 involved dividing the generated centerline into numerous points and determining the direction between each point and its next point, creating planes based on the number of points. The planes were intersected with the AAA model, and the curve with the maximum length among the generated curves was selected (Algorithm 4-3). Automated measurement of aortic neck diameter involves inputting an AAA model and the aortic neck centerline into Module 1. In Module 1, the mid-point and next point are identified, and a plane is generated based on the origin and direction, in order

to find the curve that intersects with the AAA model. By dividing the generated maximum curve into numerous points and calculating the distance between each point, the maximum distance can be obtained, which provides the output for the aortic neck diameter.

Algorithm 4-3. The module for finding the maximum curve.

---

**Input:** Aortic model with thrombus (A), Centerline of aortic model (C)  
**Output:** The maximum curve  
Set A with C  
Find the C of A  
Find the number of points for C (N)  
**For**  $i \leftarrow 0$  to N-1:  
    Create the  $i$ -line between  $i$  and  $i+1$  points  
    Make the  $i$ -plane using  $i$ -point and direction of the  $i$ -line  
    Design the  $i$ -intersection curve with  $i$ -plane and A  
    **If** intersection curve  $> 1$ :  
        **For**  $j \leftarrow$  intersection curve:  
            Append the lengths of the  $j$  intersection curves  
            Save the index of maximum length for the intersection curves  
            Find the intersection curve for index  
        Append the length of  $i$ -intersection curve  
    Save the index of maximum curve for the intersection curves  
    Find the intersection curve for index

---

Measurement of the aortic aneurysm diameter can be performed automatically by inputting the AAA model and the aortic aneurysm centerline into modules 1. In addition, the automated measurement values for the right and left iliac arteries require the plane starting points of each iliac artery. To obtain the 3D model of the iliac artery, the AAA model is cut based on the plane of the right or left side, and then the measurement is performed with modules 1. Automated measurement of the aortic neck length can be performed by selecting the aortic neck centerline from among the centerlines. The common iliac artery tortuosity is calculated by measuring the length of the AAA model and the right or left iliac artery centerline, and determining the distance between two points based on the starting and ending points of the centerline, along with a ratio. Finally, the aortic neck angulation can be calculated by determining the angle between two lines based on the starting and ending points of the centerlines of the aortic neck and aortic aneurysm (Algorithm 4-4).

Algorithm 4-4. The algorithms for the automatic measurement of the aortic neck diameter, aortic aneurysm diameter, the common iliac artery diameter, aortic neck length, the tortuosity of common iliac artery, and aortic neck angulation.

---

**Input:** Aortic model with thrombus (A), Aortic neck centerline (ANC), Aortic aneurysm centerline (AAC), Centerline of right iliac artery (CRIA) and left iliac artery (CLIA), Plane of right iliac artery (PRIA) and left iliac artery (PLIA)

**Output:** aortic neck diameter, aortic aneurysm diameter, right iliac artery diameter or left iliac artery diameter, aortic neck length, the common iliac artery tortuosity, aortic neck angulation

Set A, ANC, AAC, CRIA, CLIA, PRIA, and PLIA

**For**  $i \leftarrow$  Landmark

**If**  $i ==$  “aortic neck diameter”

Find the ANC of A and the number of mid-point and next point of ANC

Create the line between two points and the mid-plane using mid-point and direction of the line

Design the intersection curve with mid-plane and A

Calculating the maximum distance between two points

Print the maximum of the aortic neck diameter

**Else if**  $i ==$  “aortic aneurysm diameter”

Find the AAC of A and the number of points for ANC (N)

Apply algorithm 4-3

Calculating the maximum distance between two points

Print the maximum of the aortic aneurysm diameter

**Else if**  $i ==$  “right iliac artery diameter” or “left iliac artery diameter”

Cut A using PRIA or PLIA

Find the iliac artery model (IAM) with the maximum volume for the cut A models

Find the number of points for CRIA or CLIA (N)

Apply algorithm 4-3

Calculating the maximum distance between two points

Print the maximum of the right iliac artery diameter or left iliac artery diameter

**Else if**  $i ==$  “aortic neck length”

Print the length of the aortic neck

**Else if**  $i ==$  “the common iliac artery tortuosity”

Find the curve length of CRIA or CLIA and the start and end point of CRIA or CLIA

Create the line between two points

Find the line length of CRIA or CLIA

Calculate the ratio of line and curve length

Print the ratio for the line length and curve length in CRIA or CLIA

**Else**  $i ==$  “aortic neck angulation”

Make the start and end point of ANC and AAC

Create the line between start and end points of ANC and ACC

Print aortic neck angulation between two lines

---



### *Evaluation*

In order to assess the efficacy of the automated measurement method for 7 landmarks, its accuracy was compared to that of the conventional measurement method, which is performed by medical doctors. The accuracy of the two methods was evaluated by determining the differences between them, and this evaluation was conducted using Bland-Altman analysis. In addition, due to the inputs manually generated, there may be human variation in the aortic neck diameter, aortic neck length, right and left tortuosity including curve length, line length, and ratio. We randomly selected 10 cases from the 96 cases and had three researchers measure them to evaluate the inter-measurer correlation.

### *Results*

Table 4-5 provides a summary of the comparison between the conventional and automated measurement methods for the aortic neck diameter, aortic aneurysm, right iliac artery, left iliac artery diameter, aortic neck length, and the tortuosity of the right and left iliac arteries including curve length, line length, and ratio.

Table 4-5. The differences between manual and automatic measurements for the aortic neck diameter, aortic aneurysm, right iliac artery, left iliac artery diameter, aortic neck length, the tortuosity of right and left iliac artery including curve, line length, and ration between two lengths.

Landmark		Conventional measurement	Automated measurement	Difference
Aortic neck diameter (mm)		23.41 ± 3.25	24.60 ± 4.21	-1.19 ± 3.92
Aortic aneurysm diameter (mm)		55.99 ± 10.02	55.76 ± 10.10	0.23 ± 4.00
Right iliac artery diameter (mm)		18.76 ± 6.10	20.90 ± 5.57	-2.14 ± 4.37
Left iliac artery diameter (mm)		16.96 ± 5.61	19.76 ± 5.34	-2.80 ± 4.09
Aortic neck length (mm)		33.06 ± 13.50	35.71 ± 15.98	-2.65 ± 11.88
Tortuosity of right iliac artery	Curve length (mm)	46.99 ± 12.40	56.93 ± 17.76	-9.95 ± 12.81
	Line length (mm)	42.41 ± 11.62	49.49 ± 13.98	-7.08 ± 10.57
	Ratio	1.13 ± 0.24	1.14 ± 0.10	-0.01 ± 0.20
Tortuosity of left iliac artery	Curve length (mm)	52.27 ± 15.13	61.95 ± 17.64	-9.68 ± 10.96
	Line length (mm)	61.01 ± 17.64	53.65 ± 13.88	8.30 ± 7.78
	Ratio	0.86 ± 0.17	1.15 ± 0.15	-0.29 ± 0.22
Angulation	< 60°	86	89	-
	> 60°	10	7	-

Bland–Altman analysis, the arithmetic means and SD of the differences between the conventional and automated measurement were  $-1.19 \pm 3.92$  mm (limits of agreement (LoA):  $-8.88$  to  $6.50$  mm) for the aortic neck (Figure 4-6 (A)) and  $0.23 \pm 4.00$  mm (LoA:  $-7.61$  to  $8.06$  mm) for the aortic aneurysm diameter (Figure 4-6 (B)). The arithmetic mean and SD of the differences for the right iliac artery diameter, the left iliac artery diameter, and the aortic neck length was  $-2.13 \pm 4.37$  mm (LoA:  $-10.70$  to  $6.43$  mm),  $-1.50 \pm 8.60$  mm (LoA:  $-18.35$  to  $15.36$  mm),  $-2.80 \pm 4.09$  mm (LoA:  $-10.82$  to  $5.22$  mm) , and  $-2.65 \pm 11.88$  mm (LoA:  $-25.94$  to  $20.64$  mm) (Figure 4-7 (A-C)), respectively. The arithmetic means and SD of the differences for the curve length, the line length, and the tortuosity ratio

for right iliac artery was  $130.62 \pm 22.82$  mm (LoA: 85.89 to 175.35 mm),  $86.23 \pm 18.76$  mm (LoA: 49.45 to 123.00 mm), and  $0.25 \pm 0.15$  mm (LoA:  $-0.05$  to  $0.54$  mm) (Figure 4-8 (A-C)), respectively. The arithmetic mean and SD of the differences for the curve length, the line length, and the tortuosity ratio for left iliac artery  $122.32 \pm 22.69$  mm (LoA: 77.85 to 166.79 mm),  $81.01 \pm 17.95$  mm (LoA: 45.82 to 116.19 mm), and  $0.22 \pm 0.17$  mm (LoA:  $-0.10$  to  $0.55$  mm) (Figure 4-9 (A-C)), respectively.

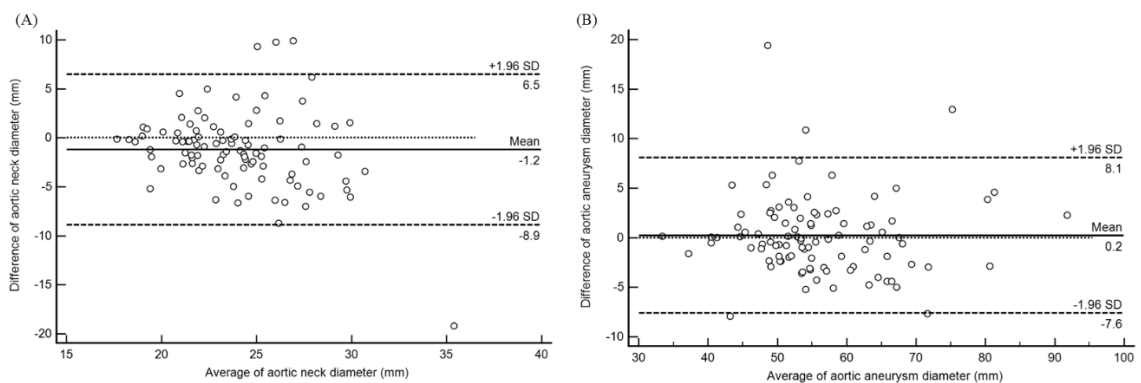


Figure 4-6. Bland–Altman plot indicating the distribution of the differences between manual and automatic method, divided by (A) the aortic neck diameter and (B) the aortic aneurysm diameter.

Figure 4-7. Bland–Altman plot indicating the distribution of the differences between manual and automatic method, divided by (A) the right iliac artery diameter, (B) the left iliac artery diameter, and (C) the aortic neck length.

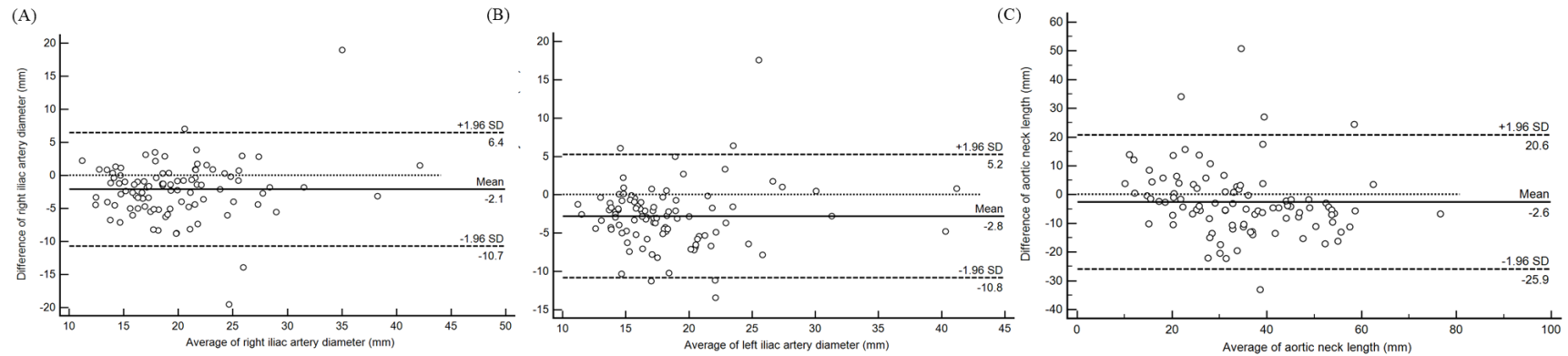


Figure 4-8. Bland–Altman plot indicating the distribution of the differences between manual and automated method, divided by (I) the curve length, (J) the line length, and (K) the tortuosity ratio for left iliac artery.

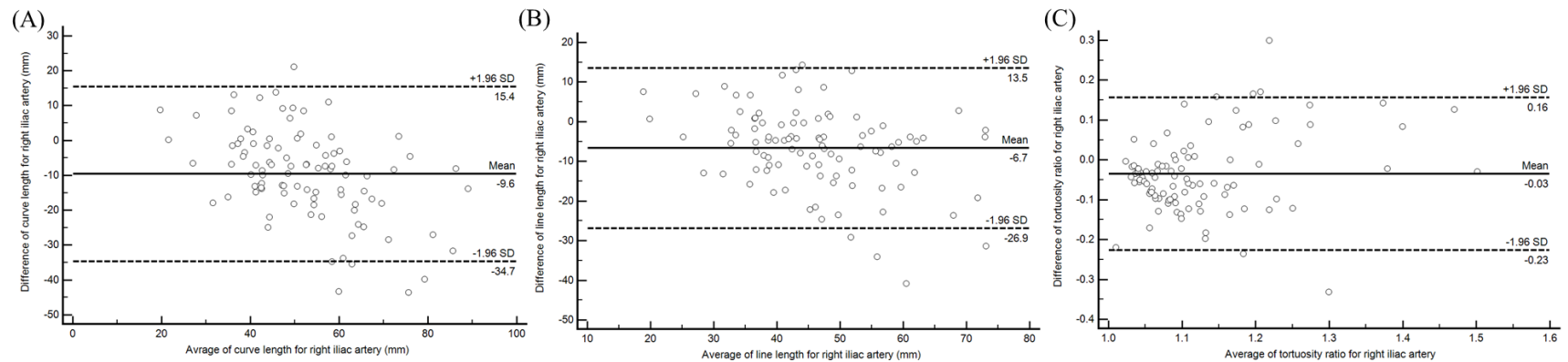
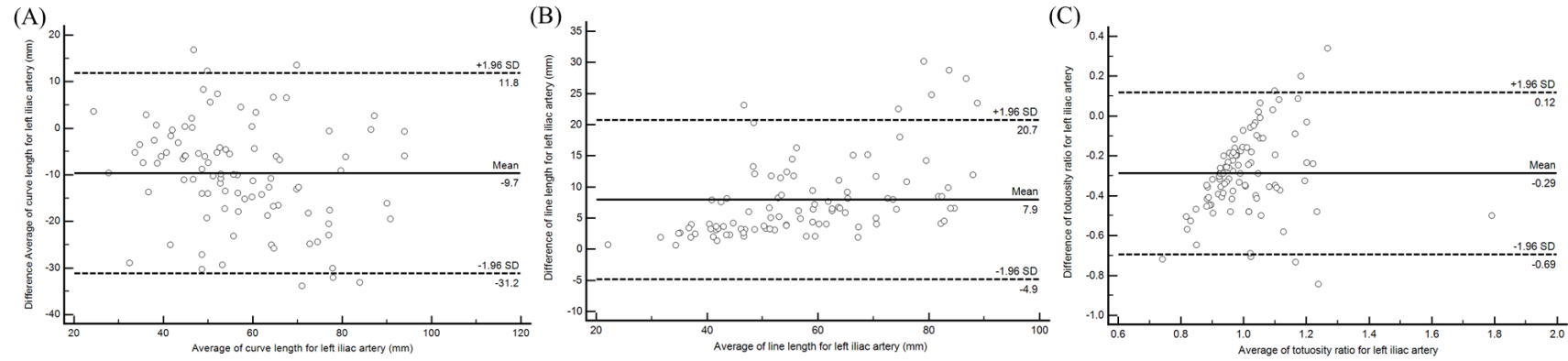


Figure 4-9. Bland–Altman plot indicating the distribution of the differences between manual and automatic method, divided by (A) the curve length, (B) the line length, and (C) the tortuosity ratio for left iliac artery.



## **5 Utilization of patient-specific guides fabricated using 3D printing from viewpoint of clinical application**

### **5.1 3D printed surgical guides in thoracoabdominal aortic dissection**

The octopod technique is a proposed method to reconstruct grafts in cases of thoracoabdominal aortic dissection using 2D images. However, the accuracy of this image-based approach is limited in terms of the precise placement of branching grafts, as it relies on the expertise of the operating surgeon who constructs it. This means there may be variations in accuracy depending on the individual surgeon. To address the accuracy limitation of the octopod technique in constructing branching grafts, a 3DP-based reconstruction method has been introduced. This approach allows for a more precise and accurate construction of the aorta and its branching vessels, improving the overall accuracy of the reconstruction process [58]. Two new techniques have been developed using patient-specific 3D printed graft reconstruction guides. The first technique is called the model-based technique (MBT), which involves the use of a realistic-shaped graft model containing the main aortic body and its branching vessels. This technique allows for the manual positioning of the branching grafts on the artificial aortic graft using the visualizing guide. The second technique is called the guide-based technique (GBT), which uses marking guides to substitute the branching vessels in the visualizing guide with slightly protruding marking points. We used to the automated segmentation and design to fabricate the visualizing and marking guide with 3DP. In section, the accuracy and marking time efficiency of three techniques were evaluated in the context of proper positioning of aortic branching vessels. These techniques included the conventional IBT, the MBT, and the GBT. A designed graft model (DGM) was used as the gold standard for comparison purposes.

#### *Procedure*

The process for implementing the two graft guide techniques, MBT and GBT, is shown in Figure 5-1. The visualizing and marking guides were fabricated by segmenting CT images, designing and modeling, and exporting them to the STL format. These models were then

printed using CJP and SLA technology. Following printing, the models underwent post-processing and ethylene oxide gas sterilization. The MBT and GBT techniques were used for graft reconstruction in a clinical setting, and their accuracy and time requirements were compared to the conventional IBT technique. The performance of all three techniques (IBT, MBT, and GBT) was evaluated in terms of their accuracy and time requirements.

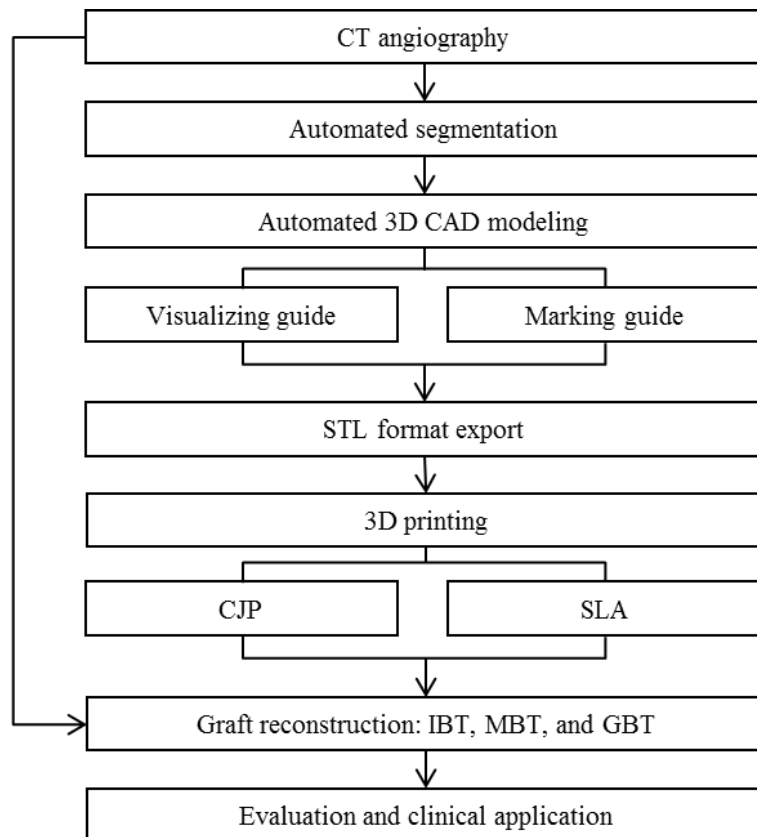


Figure 5-1. Overall process of graft reconstruction with the conventional IBT, MBT, and GBT.

#### *Dataset*

The study used imaging and clinical data from 15 patients who had been diagnosed with Crawford extent II or III thoracoabdominal aortic dissection and had undergone open surgical aortic repair using 3DP technologies at the AMC between January 2017 and February 2020. Specifically, the study focused on reconstructing segmental arteries located between the thoracic-8 and lumbar-2 levels, and reconstructing the main stem aortic graft

from the left subclavian artery to either the infra-renal abdominal aorta or to the bilateral common iliac artery. Table 5-1 provides detailed information on the characteristics of each subject included in the study. All subjects underwent CT angiography using Siemens SOMATOM series equipment, with a slice thickness of 0.6 – 3.0 mm and 70 – 120 kVp.

Table 5-1 Individual profiles of the subject patients including classification, level of segmental artery, and range of replacement. Note. T, thoracic; L, lumbar; Rs, right side; Ls, left side; LSA, left subclavian artery; IMA, inferior mesenteric artery; CIA, common iliac artery; RA, renal artery.

Patients No	Age	Classification (Extent)	Level of segmental arteries			Range of graft reconstruction
			Direction	T	L	
1	36	II	Rs	10	-	LSA to IMA
			Ls	9, 10		
2	57	II	Rs	8, 10	-	LSA to CIA
			Ls	12		
3	48	II	Rs	9, 10, 11, 12	-	LSA to RA
			Ls			
4	40	I	Rs	9, 11	-	LSA to IMA
			Ls	9, 10		
5	37	II	Rs	11, 12	-	T-9 to CIA
			Ls	11		
6	46	III	Rs	11, 12	-	LSA to CIA
			Ls			
7	33	II	Rs	8, 9	-	LSA to IMA
			Ls			
8	22	II	Rs	10, 11, 12	-	LSA to RA
			Ls			
9	65	III	Rs	10	-	T- 10 to CIA
			Ls	11		
10	51	III	Rs	10, 11	1	LSA to CIA
			Ls	10	1	
11	69	II	Rs	8, 11, 12	-	LSA to CIA
			Ls	11		
12	57	IV	Rs	10, 12	-	LSA to CA
			Ls	9, 10, 12		
13	22	II	Rs	9, 10, 12	1, 4	T- 9 to CIA
			Ls	11, 12	1	
14	38	III	Rs	7, 8, 10, 11, 12	1, 3	T-7 to CIA
			Ls	7, 8, 9, 10, 11, 12	7, 8, 9, 10, 11, 12	
15	40	II	Rs	8, 10, 12	2, 3, 4	LSA to CIA
			Ls	8, 11	3, 4	



### *Conventional image-based technique (IBT)*

The conventional IBT technique proposed by Park et al. [120] involves several steps. First, in the axial view of the CT images, the location of the visceral and segmental arteries is identified. Second, the angle between the visceral and segmental arteries is evaluated by drawing a horizontal line and a virtual diverging line of the branch from the central spot of the aorta on each axial slice of CT images at the visceral and segmental levels, and measuring the angle between them at each level. Third, based on the location of the visceral artery, the height of the corresponding segmental artery is determined and marked on the main aortic graft using the measured angle. Finally, these steps are repeated for each segmental artery that needs to be reconstructed.

### *Development of visualizing and marking guides*

During the manual segmentation process of the native aorta, the important branching vessels such as the celiac artery, superior mesenteric artery, renal artery, bilateral common iliac artery, and segmental arteries were identified and included (Figure 5-2(A)). Once the 3D rendering of the segmented aorta was completed, the CAD modelling software was used to extract the centreline of the aorta. The centreline was then adjusted to match the shape of the spine, which was also included in the segmentation (Figure 5-2(B)). To create an aortic graft that matches the desired diameter between 24 – 30 mm, a virtual model of the aorta was designed. The side-branches were combined into a single model with a diameter of 8.0 mm. To improve the accuracy and efficiency of constructing the aortic graft, two type of graft reconstruction guides were developed: (1) The visualizing guide was designed as a realistic-shaped graft model containing the main aortic body and its branching vessels, to enable manual positioning of the branching grafts on the artificial aortic graft (Figure 5-2(C-left)); (2) In the marking guide, the branching vessels in the visualizing guide were replaced by slightly protruding marking points (2.0 mm), to ensure that their positions were designed such as to be identifiable by tactile sense when wrapped by the aortic graft, instead of depending solely on visual mimicking (Figure 5-2(C-right)). The DGM was validated by operating surgeons, following which it was exported as STL files.

### *3DP technology*

To create the visualizing guide, a CJP was used along with VisiJet PXL Core powder, VisiJet PXL clear binder, and color bonding materials. The resulting phantom is shown in Figure 5-2(D-left). The marking guide, which is meant for temporary mucosal contact, was printed using a SLA with Dental LT resin (Figure 5-2(D-right)). To fabricate the graft reconstruction guides, specific parameters were used for each printer. For the CJP, the layer thickness was set to 0.10 mm, the FOV was  $254 \times 381 \times 203$  mm, and the X-Y plane resolution was  $300 \times 450$  DPI. For the SLA, the layer thickness was also set to 0.10 mm, while the FOV was  $145 \times 145 \times 145$ , and the X-Y resolution was approximately 0.15 mm. The precise X-Y resolution of the SLA was not initially defined, Formlabs Inc. experimented with different specimens to determine it. The laser used had a spot size of 140  $\mu\text{m}$  and a power of 250 mW.

### *Graft reconstruction method using MBT and GBT*

During real surgical operations, the grafts were sewn in advance by the operating surgeon with the patient while they were under anaesthesia. The surgeon used either the MBT or GBT to pre-sew the grafts, and then they were used to replace the diseased section of the thoracoabdominal aorta during the surgery (Figure 5-2(E)). After the surgery, CT images were taken to confirm the configuration of the replaced aorta (Figure 5-2(F)). The steps involved in the patient-specific graft reconstruction guides using MBT and GBT are shown in Figure 5-3. During the patient-specific graft reconstruction using MBT, the main graft body's shape was replicated while being supervised by the visualizing guide (Figure 5-3(A)). The segmental vessels' locations were also marked on the main graft body, using the celiac artery origin as a reference point (Figure 5-3(B)). In the case of GBT, the marking guide was placed into the aortic graft and aligned in reference to the origin of the visceral arteries (Figure 5-3(C)). The positions of the segmental arteries were then identified using the tactile sense by feeling the protruding markers and marked on the graft surface (Figure 5-3(D)). After performing either MBT or GBT, the mark is cut out with medical scissors and the segmental grafts were attached by running sutures (Figure 5-3(E)).

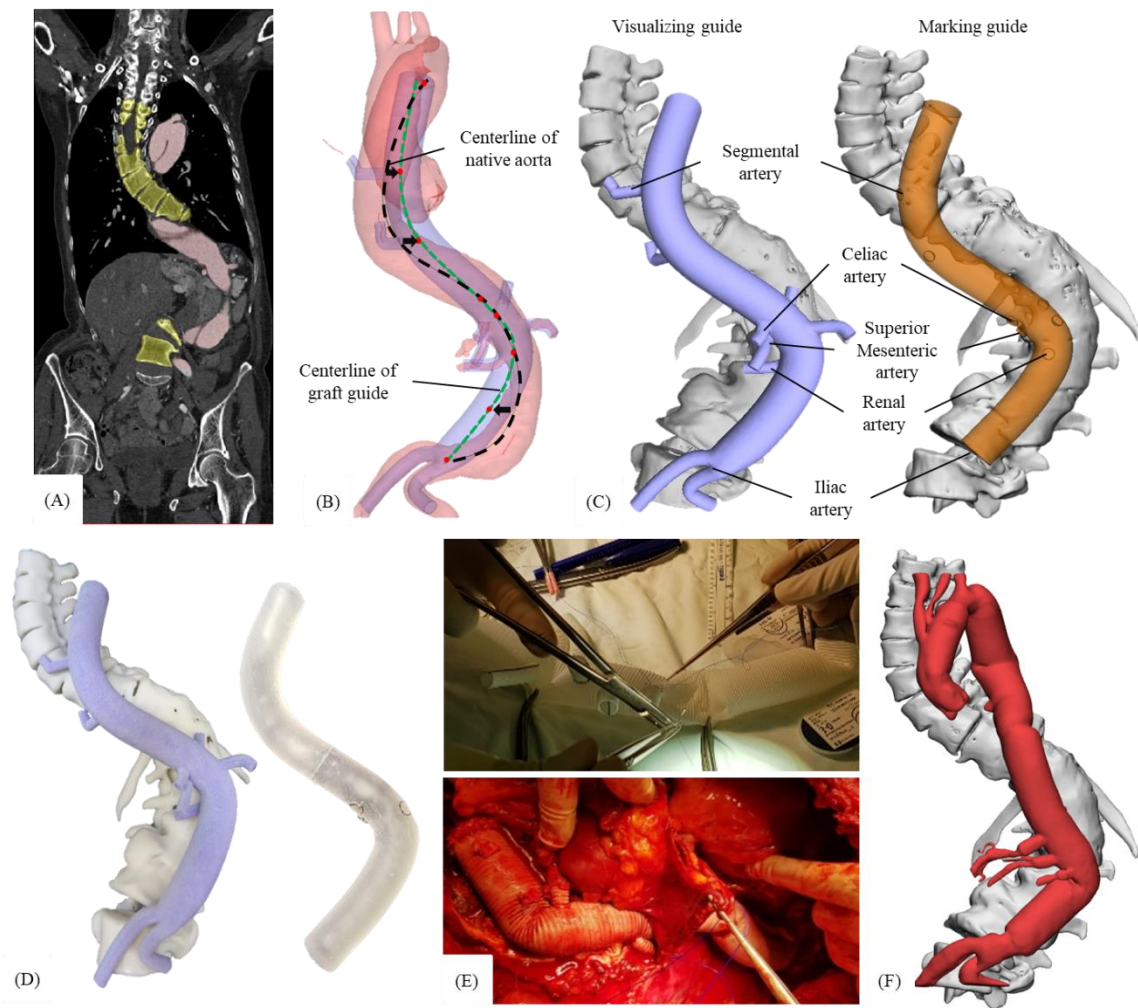
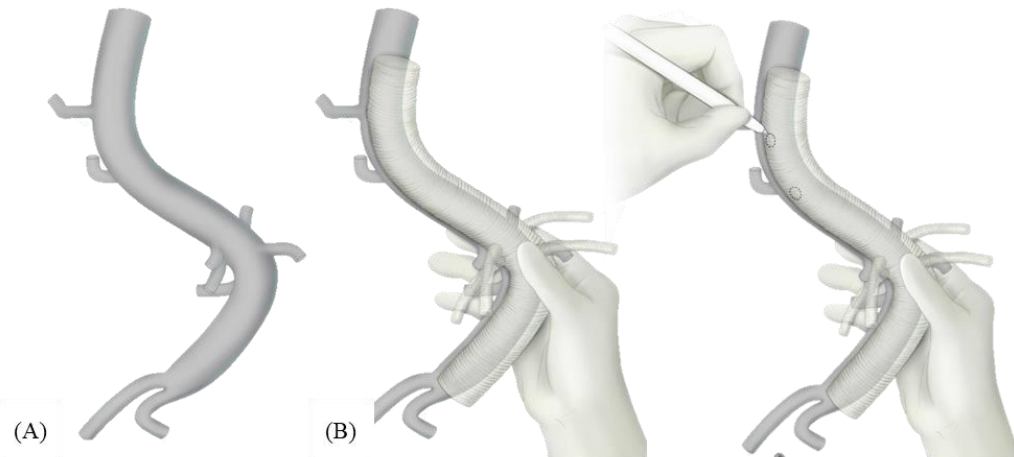


Figure 5-2. Two types of patient-specific graft reconstruction guide application for open repair of thoracoabdominal aortic dissection. (A) CT angiography images and segmentation of diseased aorta and spine. (B) The modeling the centreline of graft based on that of a native aorta. (C) 3D modeling of the visualizing and marking guides. (D) 3D-printed visualizing guide and marking guide; (E) graft reconstruction and clinical application in operating room. (F) The 3D model of postoperative graft.

Model-based technique (MBT)



Guide-based technique (GBT)

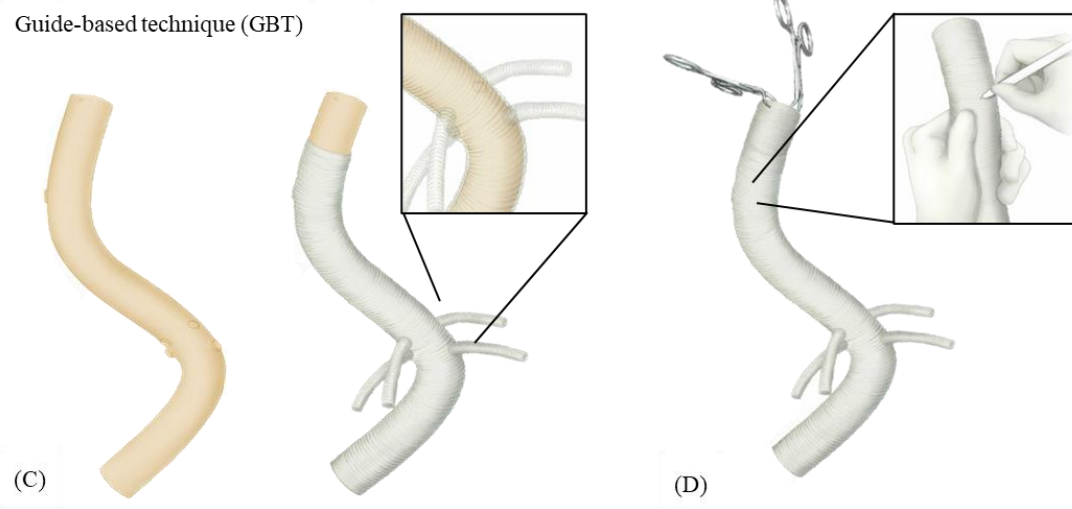


Figure 5-3. Patient-specific graft reconstruction process with MBT and GBT in operating room.

### *Survey*

To evaluate the effectiveness of the proposed techniques, a survey was conducted among three cardiothoracic surgeons who had experience with graft reconstruction using three different techniques: IBT, MBT, and GBT. The survey questionnaire was written to in-house by collecting feedback on anatomical understanding, usefulness, satisfaction, surgical outcomes, and recommendations from a clinical perspective. The survey was conducted among certified cardiothoracic surgeons who had between 3 to 10 years of experience. The questionnaire items were categorised as follows: (1) the level of contribution to understanding the anatomic structure (four questions); (2) usefulness for graft reconstruction (three questions); (3) satisfaction level for graft reconstruction (two questions); and (4) benefits of the use of 3DP technologies to surgical outcomes (two questions); and (5) recommendability of 3DP for thoracoabdominal aorta surgery to other surgeons (two questions). The responses to the survey questions were measured on a five-point scale, where the scores were recorded as follows: 1 = strong disagreement, 2 = disagreement, 3 = neutral, 4 = agreement, and 5 = strong agreement.

### *Evaluation and statistical analysis*

In a retrospective study, the accuracy and time required for marking of vessels were measured and analyzed between conventional IBT, MBT, and GBT techniques and DGM-based technique. The study involved three researchers performing the experiments on 15 patients, using mimic aortic grafts to carry out the experiments. The time required for marking of vessels, excluding cutting out, was assessed for each technique. To evaluate the accuracy of the graft reconstruction techniques, the positions of the segmental arteries were marked on the grafts using IBT, MBT and GBT (Figure 5-4(A)). The grafts were then unfolded using scissors (Figure 5-4(B)). The diagonal line, height, and angle between the celiac artery and the marked segmental arteries were measured (Figure 5-4(C)).

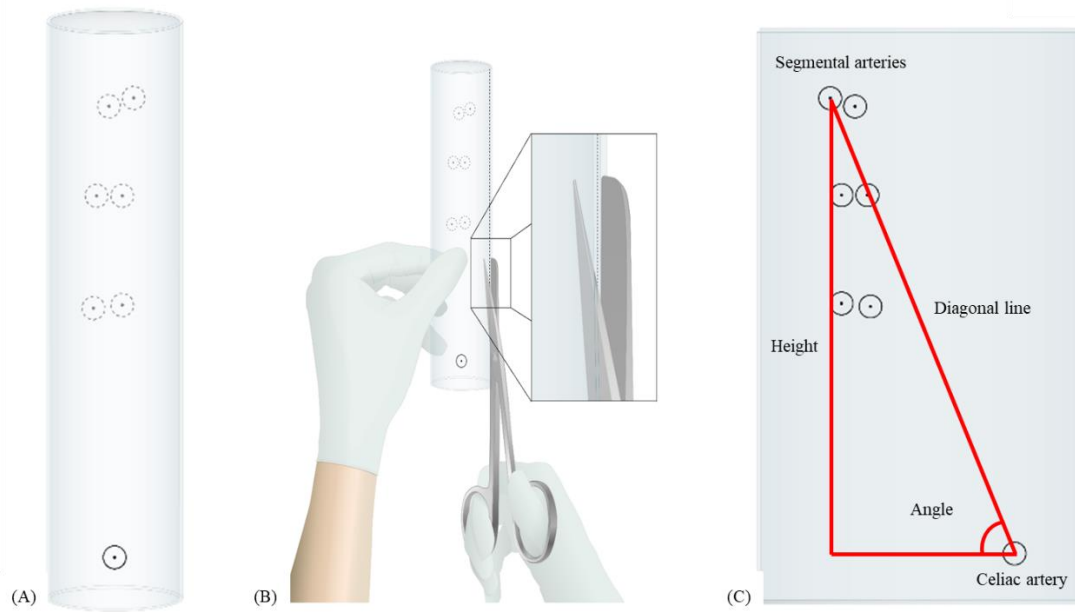


Figure 5-4. Guide to evaluating the accuracy of three techniques-IBT, MBT, and GBT; (A) Locating celiac artery and segmental arteries marked on graft. (b) Spreading the graft using scissors. (c) Measuring the length, height, and angle between celiac artery and segmental arteries.

The Bland-Altman analysis was utilized to compare and identify the differences, LoA, biases, and outliers in the diagonal line, height, and angles of the DGM and three techniques - IBT, MBT, and GBT [142]. The paired t-test was used to assess differences in measurements and marking time between the DGM and three techniques, IBT, MBT, and GBT. Correlation coefficients ( $r$ ) were also calculated to compare the DGM and the three techniques, and the correlation analyses showed statistically significant differences, based on an independent group of the same sample size. The researchers performed an Intra correlation coefficient (ICC) analysis on the IBT, MBT, and GBT experiments to confirm the correlations among them. In addition, the survey results on the IBT and the MBT or GBT were analyzed using the Wilcoxon signed rank test. All of the statistical analyses were conducted.

## Results

Table 5-2 presents the measurement of the diagonal line, height, and angle from the celiac artery to the segmental arteries for the DGM, whose design was validated by surgeons, conventional IBT, MBT, and GBT. The average time required to mark the vessel fenestrations (excluding cutting) using these three techniques for 15 patients was shown in Table 5-2. The MBT and GBT techniques showed a reduction in marking time by 17.6 and 15.5 minutes, respectively, compared to the traditional IBT technique.

Table 5-2. Measurements and time requirements of graft reconstruction using DGM, IBT, MBT, and GBT. Note. DGM, digital graft model; IBT, image-based technique; MBT, model-based technique; GBT, graft-based technique.

Measurements	DGM		IBT		MBT		GBT	
	Mean ± SD	Mean ± SD	P	Mean ± SD	P	Mean ± SD	P	
Diagonal line (mm)	82.19 ± 37.18	91.38 ± 42.38	<0.001	83.87 ± 33.85	<0.05	83.19 ± 33.27	0.053	
Height (mm)	70.20 ± 43.99	79.46 ± 50.42	<0.001	71.70 ± 41.77	<0.05	68.41 ± 41.91	<0.001	
Angle (°)	47.38 ± 18.67	57.14 ± 23.21	<0.001	56.28 ± 22.31	<0.001	53.77 ± 22.52	<0.001	
Time (min)	-	18.43 ± 9.60		0.80 ± 0.25		2.88 ± 0.83	<0.001	

According to the Bland–Altman analysis, the arithmetic mean and SD of the differences between the DGM and conventional IBT were  $-9.19 \pm 16.47$  mm (LoA:  $-41.47$  to  $23.08$  mm) for the diagonal line,  $-9.25 \pm 16.84$  mm (LoA:  $-42.26$  to  $23.76$  mm) for the height, and  $-9.76^\circ \pm 10.05^\circ$  (LoA:  $-29.47^\circ$  to  $9.95^\circ$ ) for the angle (Figure 5-5 (A-C)), respectively; the differences between the DGM and MBT was  $-1.67 \pm 8.11$  mm (LoA:  $-17.56$  to  $14.21$  mm) for the diagonal line,  $-1.50 \pm 8.60$  mm (LoA:  $-18.35$  to  $15.36$  mm) for the height, and  $-8.89^\circ \pm 10.93^\circ$  (LoA:  $-30.31^\circ$  to  $12.52^\circ$ ) for the angle (Figure 5-5 (D-F)), respectively. The arithmetic difference values for the diagonal line, height, and angle between the DGM and GBT were  $-1.00 \pm 7.27$  mm (LoA:  $-15.25$  to  $13.24$  mm),  $1.79 \pm 4.93$  mm (LoA:  $-7.86$  to

11.45 mm), and  $-6.39^\circ \pm 10.29^\circ$  (LoA:  $-26.55^\circ$  to  $13.78^\circ$ ) (Figure 5-5 (G-I)), respectively. There were statistically significant differences in all the measurements taken for the IBT, MBT, and GBT techniques, except for the diagonal line in the GBT.

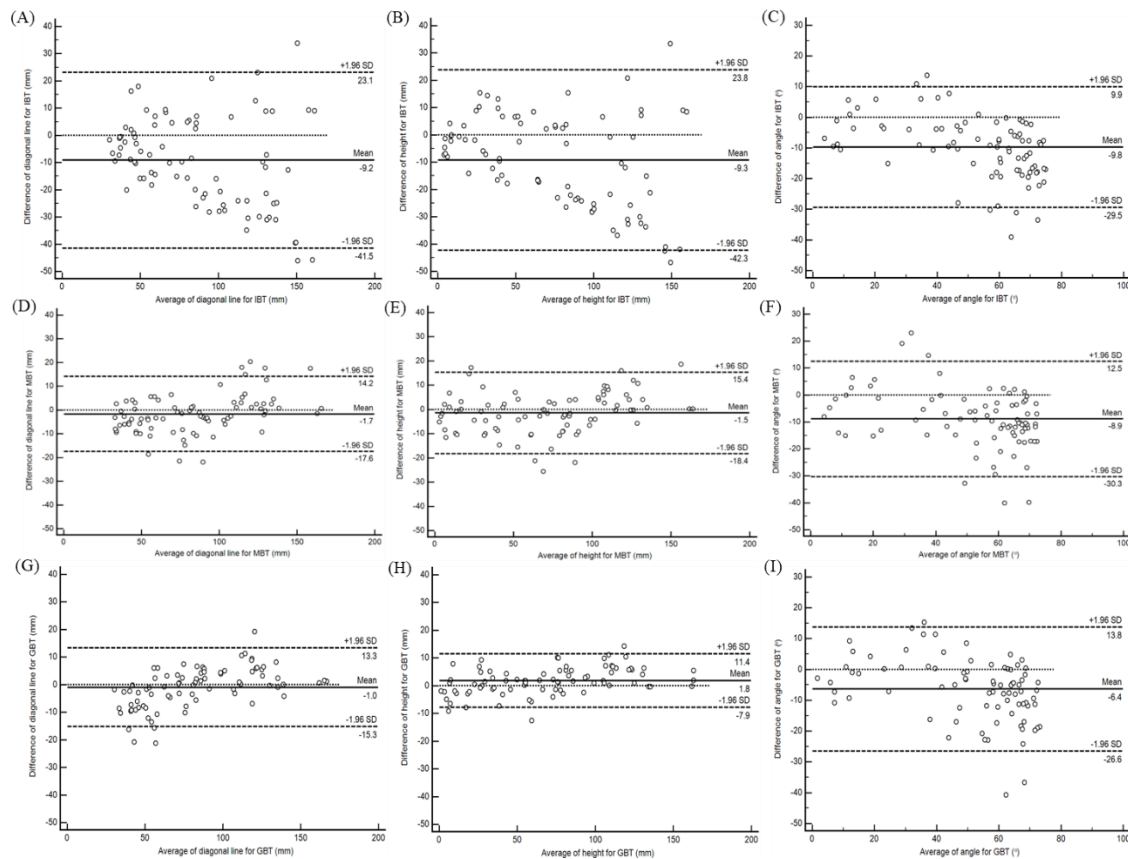


Figure 5-5. Bland–Altman plot indicating the distribution of the differences between DGM and IBT, divided by (A) diagonal line, (B) height and (C) angle; between the DGM and MBT, divided by (D) diagonal line, (E) height, (F) angle; and between the DGM and GBT, divided by (G) diagonal line, (H) height, and (I) angle.

Table 5-3 shows the comparison results of correlation coefficients among three techniques (IBT, MBT, and GBT) and researchers, based on the diagonal length, height, and angle of the DGM. All the correlation coefficients indicated strong correlation with statistical significance. Furthermore, the ICC among three independent researchers demonstrated a high level of agreement, with a score of 0.986 for the conventional IBT and MBT techniques, and 0.995 for the GBT technique.



Table 5-3. Correlation coefficient between DGM and three techniques for diagonal length, height, and angle. Note. r12, correlation coefficient for DGM and IBT; r13, correlation coefficient for DGM and MBT; r14, correlation coefficient for DGM and GBT.

Comparing correlation coefficient		Diagonal line		Height		Angle	
		r12	P	r13	P	r14	P
DGM	IBT	0.905	<0.001	0.933	<0.001	0.884	<0.001
	MBT	0.959	<0.001	0.970	<0.001	0.858	<0.001
	GBT	0.980	<0.001	0.993	<0.001	0.875	<0.001

Table 5-4 displays the scores obtained from a survey questionnaire that evaluated the effectiveness of graft reconstruction guides in thoracoabdominal aortic repair. The survey asked participants to rate three different guides (IBT, MBT, and GBT) across several categories, including understanding, usefulness, satisfaction, surgical outcome, and recommendability for use by other surgeons. According to the survey results presented in the text, the average score obtained with MBT and GBT graft reconstruction guides was  $59.33 \pm 0.58$  out of 65, which is significantly higher than the score obtained with the conventional IBT guide, which was only 20.67. In addition, For the contribution to understanding the anatomic structure, 58.3% of the answers indicated strong agreement, 25%, agreement, and 8.33%, neutral and disagreement for the MBT and GBT, whereas for the conventional IBT, 25% of the answers indicated neutral, 41.7%, disagreement, and 33.3%, strong disagreement. Under the usefulness for graft reconstruction, 88.9% of the answers indicated strong agreement and 11.11%, agreement, in the MBT and GBT, whereas 22.2% indicated disagreement and 77.8%, strong disagreement in the conventional IBT. Finally, for the MBT and GBT, satisfactoriness of graft reconstruction, surgical outcomes, and recommendability to other surgeons was 88.33%, 66.67%, and 16.67% of strong agreement, and 16.67%, 33.33%, and 83.33% of agreement, respectively, and, in the conventional IBT, 50% of disagreement and strong agreement were identified. Generally, the MBT and GBT scored higher than the conventional IBT with statistical significance.

Table 5-4. Retrospective survey in relation to understanding, usefulness, satisfaction, surgical outcome, and recommendability for use in other applications for IBT without 3D printing technique and MBT and GBT with 3D printing technique.

Classification	IBT (without 3DP)	MBT and GBT (with 3DP)	<i>P</i>
Understanding the anatomic structure	1.92 ± 0.79	4.33 ± 0.98	<0.01
Usefulness for graft reconstruction	1.22 ± 0.44	4.88 ± 0.33	<0.01
Satisfaction for graft reconstruction	1.50 ± 0.55	4.83 ± 0.41	<0.05
Surgical outcomes	1.50 ± 0.55	4.67 ± 0.52	<0.05
Recommendations for other applications	1.67 ± 0.52	4.17 ± 0.41	<0.05

## 6 Discussion

Most medical devices are developed or tailored to fit common diseases or adults, leaving a significant unmet clinical demand for pediatric surgery, rare and complex cases, and surgeries that are difficult to standardize. 3DP technology can address these issues in medical applications. In order to apply 3DP in medicine, essential processes are required such as medical image acquisition, segmentation, 3D modeling, and measurement. However, these repetitive manual tasks are tedious, labor-intensive, time-consuming, and lack of consistency. In the typical workflow, it usually takes about a week from medical image acquisition to the fabrication of patient-specific guides or simulators using 3DP, which poses a significant time limitation for applying 3DP technology to emergency patients. To address these challenges, it is essential to develop automated workflows that incorporate advanced segmentation techniques using AL, along with API of CAD for design and measurement. Moreover, it is important to demonstrate the efficacy and efficiency of 3DP technology in clinical applications. The automated method and 3DP application in medicine offer several advantages: 1) it significantly reduces repetitive and labor-intensive manual workflow; 2) it alleviates time-consuming process; 3) it can be easily led to maintenance of consistency in semi-automated workflow and researchers; 4) it enables apply various application in medical fields. In this paper, we classified the necessary steps for implementing semi-automated workflows and 3DP technology for clinical applications as follows: 1) Automated and enhanced segmentation using semantic segmentation with AL, 2) Automated design and measurement with API of CAD, 3) Utilization of patient-specific guides fabricated using 3DP from viewpoint of clinical application.

Firstly, several experiments were conducted on Kidney CT with RCC, Dental CBCT, thoracoabdominal CT angiography, and abdominal CT angiography for automated segmentation using AL. AL is introduced to optimize the labeling dataset with stress testing by dividing the small amount of data and reducing labeling time and annotation effort for a large amount of data with smart labeling. Furthermore, manual segmentation can lead to variations in human labels due to inter- and intra-human variability. AL frameworks can mitigate this uncertainty by improving collaboration with the DL algorithm, thus increasing accuracy [28-35]. In addition, a systematic stress test can determine the minimum number of training data required to achieve clinically acceptable accuracy. We have distinguished several distinctive features for each study. In the kidney study, a total of 50 datasets consisted of artery, vein, ureter, parenchyma, and RCC were utilized and divided into 3 stages. Stage 1 employed datasets containing RCC, while Stage 2 and 3 included both RCC and normal

kidneys. The cascaded 3D U-Net model was employed with high-resolution images (slice thickness of 0.70 - 1.00 mm). In the condyle study, a total of 234 datasets were utilized and divided into 5 stages. Stages 1, 2, and 3 consisted exclusively of datasets from KUMC, while Stages 4 and 5 included data from both KUMC and AMC. The networks were 3D U-Net and cascaded 3D U-Net. The thoracoabdominal aortic dissection study utilized a dataset of 47 high-resolution images, focusing on the segmentation of aorta and vessels. The dataset was divided into three stages, employing UNETR, SwinUNET, and nnU-Net models. In the abdominal aortic aneurysm, a dataset of 300 low-resolution CT images was utilized for the segmentation of aorta, thrombus, calcification, and vessels. The dataset was divided into 5 stages, and the UNETR, SwinUNET, and nnU-Net models were employed for the AL (Table 6-1).

Table 6-1. The summary of each task

Tasks	Kidney	Mandibular condyle	Thoracoabdominal aortic dissection	Abdominal aortic aneurysm
Stage	3*	5***	3	5
Total dataset	50**	234****	47	300
Classes	Artery, Vein, Ureter, parenchyma, RCC	Mandibular condyle	Aorta, Vessels	Aorta, Thrombus, Calcification, Vessels
Preprocessing	Min-max normalization, kidney cropping	Min-max normalization, condyle cropping	Min-max normalization	Min-max normalization
Augmentation	Random rotation, flipping, resizing	Random rotation, flipping, resizing	Random rotation, flipping, resizing	Random rotation, flipping, resizing
Slice thickness	0.70 – 1.00 mm	0.30 mm	1.0 – 5.0 mm	2.5 – 5.0 mm
Network	Cascade 3D U-Net	3D U-Net, Cascade 3D U-Net	UNETR, SwinUNETR, nnU-Net	UNETR, SwinUNETR, nnU-Net
Institute	AMC	AMC, KUMC	AMC	AMC

Note: \*Stage 1 with RCC kidney and Stage 2-3 with normal and RCC kidney, \*\* 30 RCC and 20 Normal kidney \*\*\* Stage 1-3 with KUMC and Stage 4-5 with AMC and KUMC, \*\*\*\*72 AMC and 162 KUMC dataset; KUMC, Korea university medical center; AMC, Asan medical center; RCC, Renal cell carcinoma.

In normal and RCC kidney segmentation of kidney CT, the segmentation network demonstrated an increase in accuracy across the stages and its overall performance was comparable to other advanced segmentation networks. Parenchyma, which has the largest volume and relatively consistent anatomy in the kidney, was the most accurately segmented ROI. On the other hand, RCC, which has high variation in size and location and a relatively small dataset, had the lowest average and high SD among the multi-classes. Although RCC was not segmented precisely, the segmentation of the surrounding parenchyma was helpful in identifying the region where RCC was located. Vessels and ureter entering the parenchyma, as well as RCC, were thin and complex structures that posed challenges for segmentation. Despite the low mean DSC score, the segmentation in the arterial phase was useful in identifying their location (Figure 6-1). The manual segmentation and segmentation AL-corrected by the CNN took approximately 150 and 73 minutes, respectively, which is a reduction of more than 50% in time. Moreover, using AL, the AL-corrected segmentation helped to decrease the effort required for generating new ground truths. Modifying the CNN segmentation was found to be more efficient and timesaving, as well as less prone to variability, compared to manual annotation.

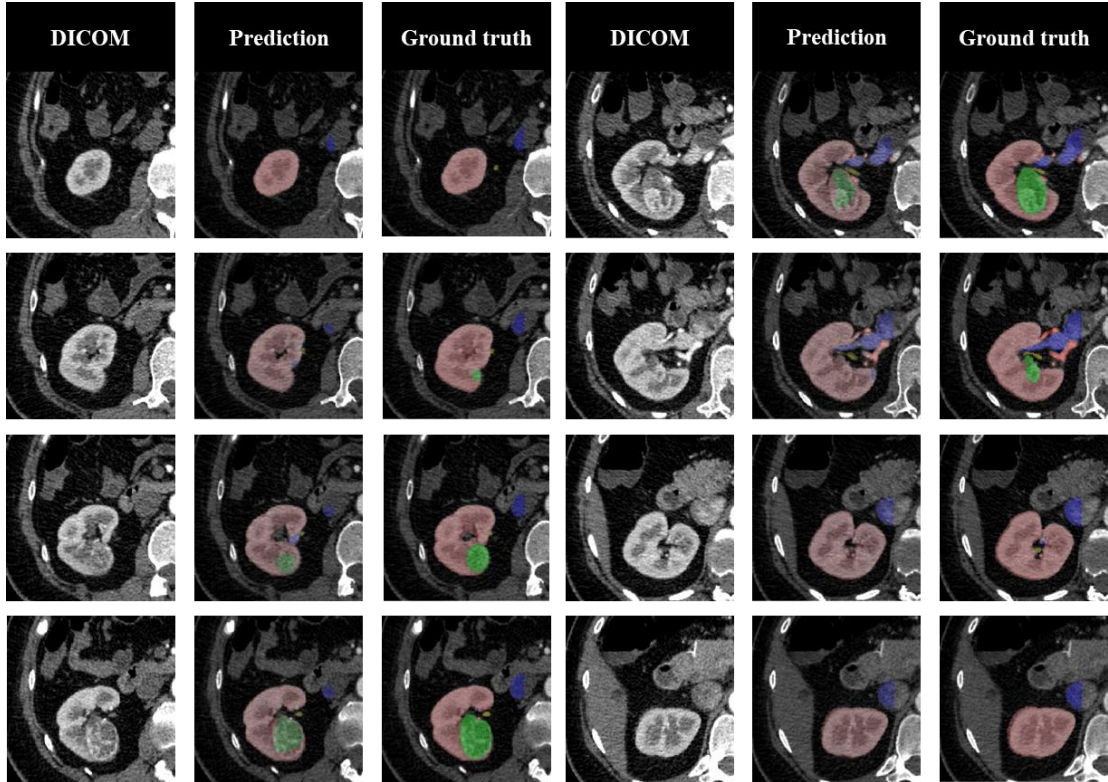


Figure 6-1. A case for cascaded 3D U-Net (A) images, (B) prediction, and (C) ground truth in kidney CT

In mandibular condyle segmentation of dental CBCT, we investigated the effectiveness of a cascade 3D U-Net model, which is a semi-automated segmentation model for mandibular condyle, and found that it had higher accuracy compared to a basic 3D U-Net architecture. The mandibular condyles were segmented using the 3D U-Net, and then the images were cropped to include a margin around the condylar head. The cascade 3D U-Net architecture was utilized to further improve the segmentation performance. The cascade 3D U-Net showed better performance than the basic 3D U-Net in all stages of test datasets, with a higher mean DSC. This suggests that the inclusion of ROI detection prior to segmentation improves the performance of the cascade model. In fact, even with a smaller dataset of 80 samples in stage I, the cascade 3D U-Net showed higher accuracy to stage III, which used 162 samples and the basic 3D U-Net (Table 3-4). In some cases, the basic 3D U-Net model showed better segmentation accuracy than the cascade 3D U-Net, and Overall HD was superior to basic 3D U-Net than cascade 3D U-Net. This could be attributed to the fact that the basic 3D U-Net was trained on full images with adjacent anatomical structures, while the cascade model was trained only on cropped images of the condylar head. As a result, the cascade model may have difficulty distinguishing adjacent structures like the maxilla and temporal bone, which could lead to noise (Figure 6-2 (A)). In addition, unlike basic 3D U-Nets, Cascade 3D U-Nets tend to be under-segmented compared to the ground truth (Figure 6-2 (B) and Table 3-14 (D)). The use of basic 3D U-Net and cascade 3D U-Net significantly reduced the segmentation time by 10.62 min and 12.45 min, respectively, compared to manual segmentation. The stress test conducted on both basic and cascade 3D U-Net models indicated that as the dataset size increased, the segmentation accuracy also improved (Table 3-4). In addition, in stage 1, 2, and 3 trained on a dataset from one institution (KUMC), a relatively low DSC was observed when testing on a dataset from another institution (AMC). However, in stage 4 and 5, which used datasets from both institutions, it was observed that the DSC dramatically increased (Table 6-2).

Table 6-2. Dice similarity coefficient for each institution with each stage of mandibular condyles with a basic 3D U-Net and cascade 3D U-Net in CBCT. Note: AMC, Asan Medical Center; KUMC, Korea University Medical Center

Institution	Model	Stage 1	Stage 2	Stage 3	Stage 4	Stage 5
AMC	Basic 3D U-Net	$0.750 \pm 0.090$	$0.731 \pm 0.094$	$0.819 \pm 0.053$	$0.908 \pm 0.015$	$0.913 \pm 0.020$
	Cascaded 3D U-Net	$0.859 \pm 0.048$	$0.855 \pm 0.044$	$0.881 \pm 0.031$	$0.914 \pm 0.027$	$0.914 \pm 0.024$
KUMC	Basic 3D U-Net	$0.888 \pm 0.027$	$0.919 \pm 0.039$	$0.915 \pm 0.030$	$0.920 \pm 0.032$	$0.925 \pm 0.022$
	Cascaded 3D U-Net	$0.924 \pm 0.025$	$0.936 \pm 0.022$	$0.935 \pm 0.026$	$0.936 \pm 0.025$	$0.938 \pm 0.019$



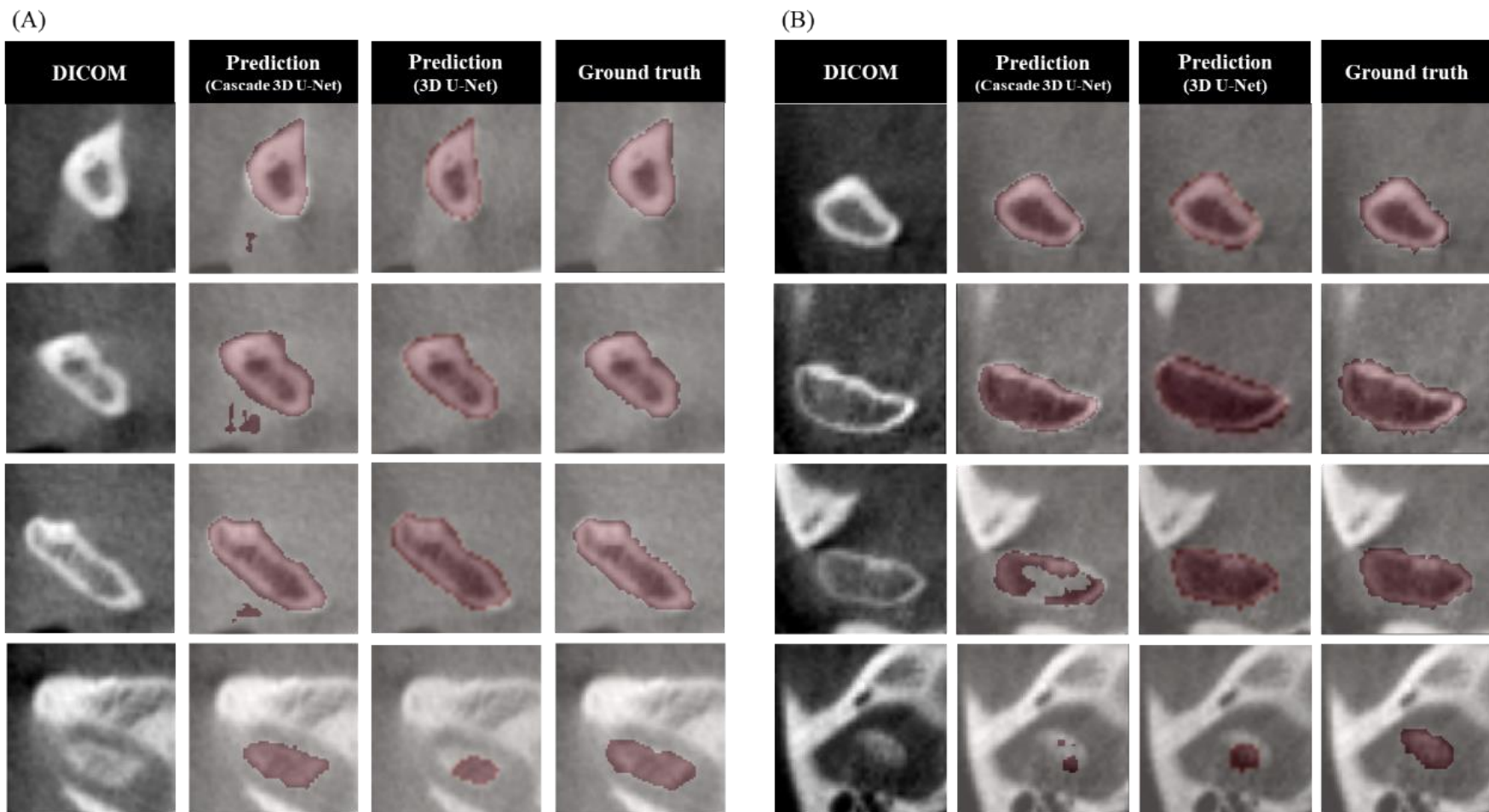


Figure 6-2. The errors for prediction of cascade 3D U-net including (A) noise and (B) under segmentation.

In thoracoabdominal aortic dissection on CT angiography, we compared the accuracy of various DL models for multi-class segmentation at different stages, including UNETR and SwinUNETR of MONAI and 2D U-Net, 3D U-Net, 2D-3D U-Net ensemble, and cascade 3D U-Net of nnU-Net. The average DSC scores for the two subclasses tended to improve or remain consistent as the stage increased (i.e., as the number of patient data increased), indicating higher or similar performance. The aorta with cascade 3D U-Net and vessels with SwinUNETR in Stage 3 achieved the highest accuracy among various networks. The average HD is shown in the best performance with 3D U-Net. Through the stress test, it was found that the aorta dataset had reached saturation in stage 2 of SwinUNETR and the vessels need more dataset to improve performance beyond stage 3 (Table 3-6). The reason for segmenting the aorta and vessels separately is that when these relatively large and small areas are trained with a single label, the numerically evaluated metrics such as DSC or HD may appear excellent, but we found that the actual important vessel segmentation is almost not performed. In all stages, the performance of aorta segmentation was superior to vessels segmentation, which showed significantly lower accuracy. Compared to the relatively large area of the aorta, vessels have complex structures, are distributed in various areas, and have a thickness of less than 1 mm, making it difficult to predict vessels accurately due to confusion with other thin vessels around them, especially those that are not intercostal arteries (Figure 6-3). The segmentation time using 3D U-Net in the final stage, which showed the best performance, was reduced by about 4 times to 24.39 min in the aorta and by about 1.5 times to 19.46 min in the vessel compared to the manual segmentation time.

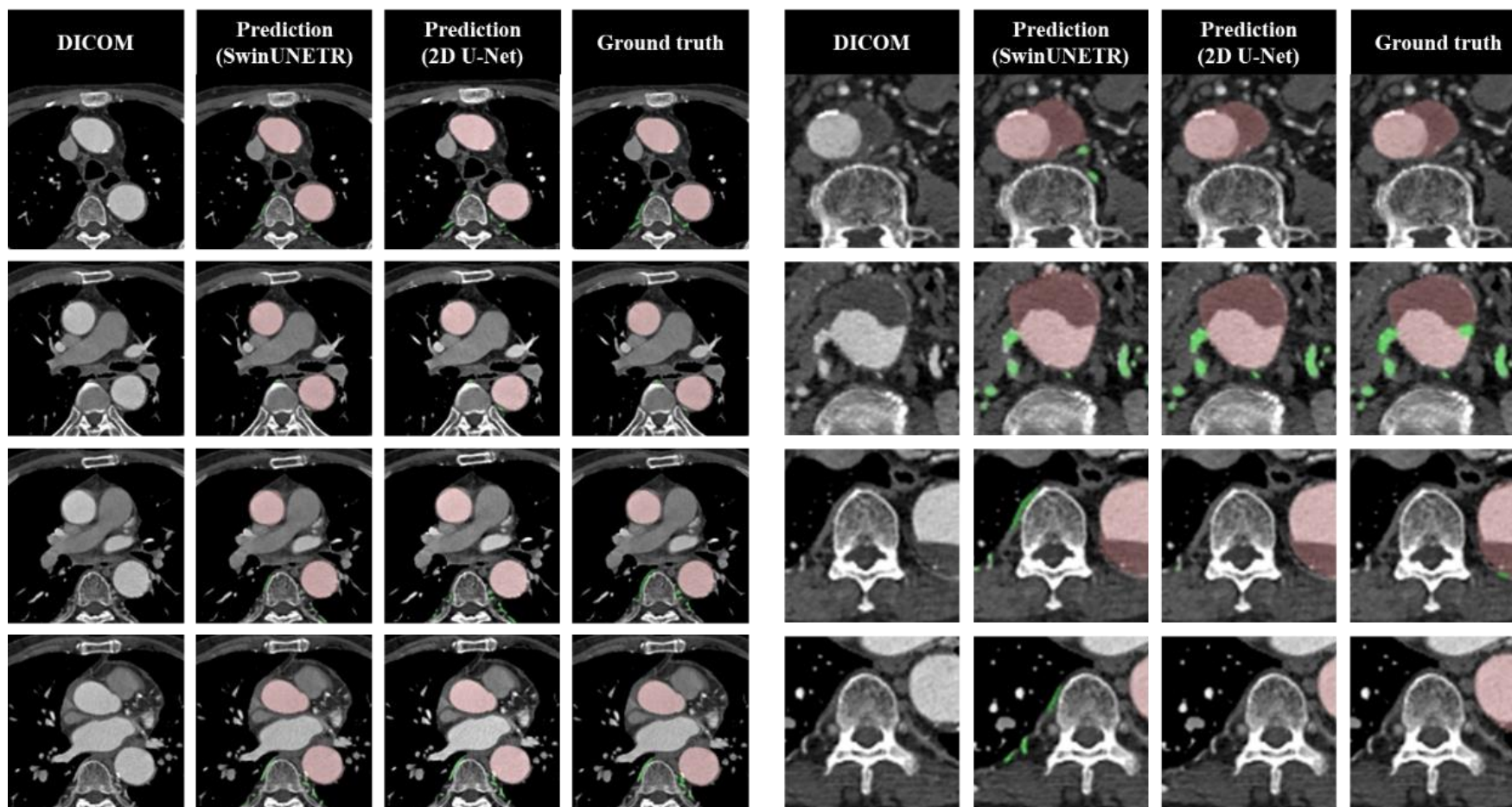


Figure 6-3. Best case for SwinUNETR with images, prediction (SwinUNETR and 2D U-Net), and ground truth in thoracoabdominal aortic dissection.

In abdominal aortic aneurysm, we compared the accuracy of various models, including UNETR and SwinUNETR of MONAI and 2D U-Net, 3D U-Net, 2D-3D U-Net ensemble, and cascade 3D U-Net of nnU-Net for each stage. Table 3-9 presents the DSC for each of the four subclasses in each of the five stages for the various networks. The average DSC scores for the four subclasses tended to improve or remain consistent as the stage increased (i.e., as the number of patient data increased), indicating higher or similar performance. The nnU-Net outperformed UNETR and SwinUNETR in all stages, and at stage 5, 2D-3D U-Net ensemble achieved the highest accuracy for aorta and calcification, respectively. For cascade 3D U-Net, thrombus achieved the best performance, while vessels showed the highest accuracy with 3D U-Net. The evaluation of HD is presented in Table 3-10, and similar to DSC, the HD values generally showed higher or comparable performance as the stage increased (i.e., as the number of patient data increased). Aorta achieved the best performance in 2D-3D U-Net ensemble, while calcification achieved the highest accuracy in 3D U-Net. In contrast to DSC, UNETR showed better performance for thrombus and vessels, respectively. Due to the usage of CT images with contrast-enhanced blood vessels, Aorta exhibited the best performance compared to other subclasses, while thrombus and calcification, particularly vessels, showed relatively poor performance. The thrombus does not have contrast agent insertion, making it difficult to distinguish from surrounding tissues and organs. In addition, it has variations in different areas and sizes among patients. Calcification is small areas and randomly distributed on the aortic wall. Furthermore, vessels consisting of lumbar and inferior mesenteric artery with thin walls are challenging to identify in low-resolution images with a slice thickness of 3 mm (Figure 6-4). Through the stress test, it was found that the aorta dataset had reached saturation in stage 1 of 3D U-Net, as the difference in DSC between stage 1 with 60 cases and stage 5 with 300 cases was the range of -0.037 to 0.072 in 3D U-Net, which was a smaller range than other subclasses. On the other hand, for calcification, there was a tendency of increasing performance from stage 1 to 3, which plateaued from stage 4 onwards. Thrombus and vessels exhibited relatively large errors between each stage, and to achieve better performance, more datasets need to be added even after stage 5 using 300 cases. Mean time for manual segmentation was  $31.88 \pm 4.04$  and  $50.09 \pm 5.93$  min in aorta and vessels, respectively and mean time for segmentation using SwinUNETR was  $7.75 \pm 2.26$  min and  $29.24 \pm 3.45$  min, respectively. Although the performance in subclasses other than aorta was relatively poor, it was observed that the time for AL-corrected segmentation was reduced compared to manual segmentation because the location of each class could be indicated.



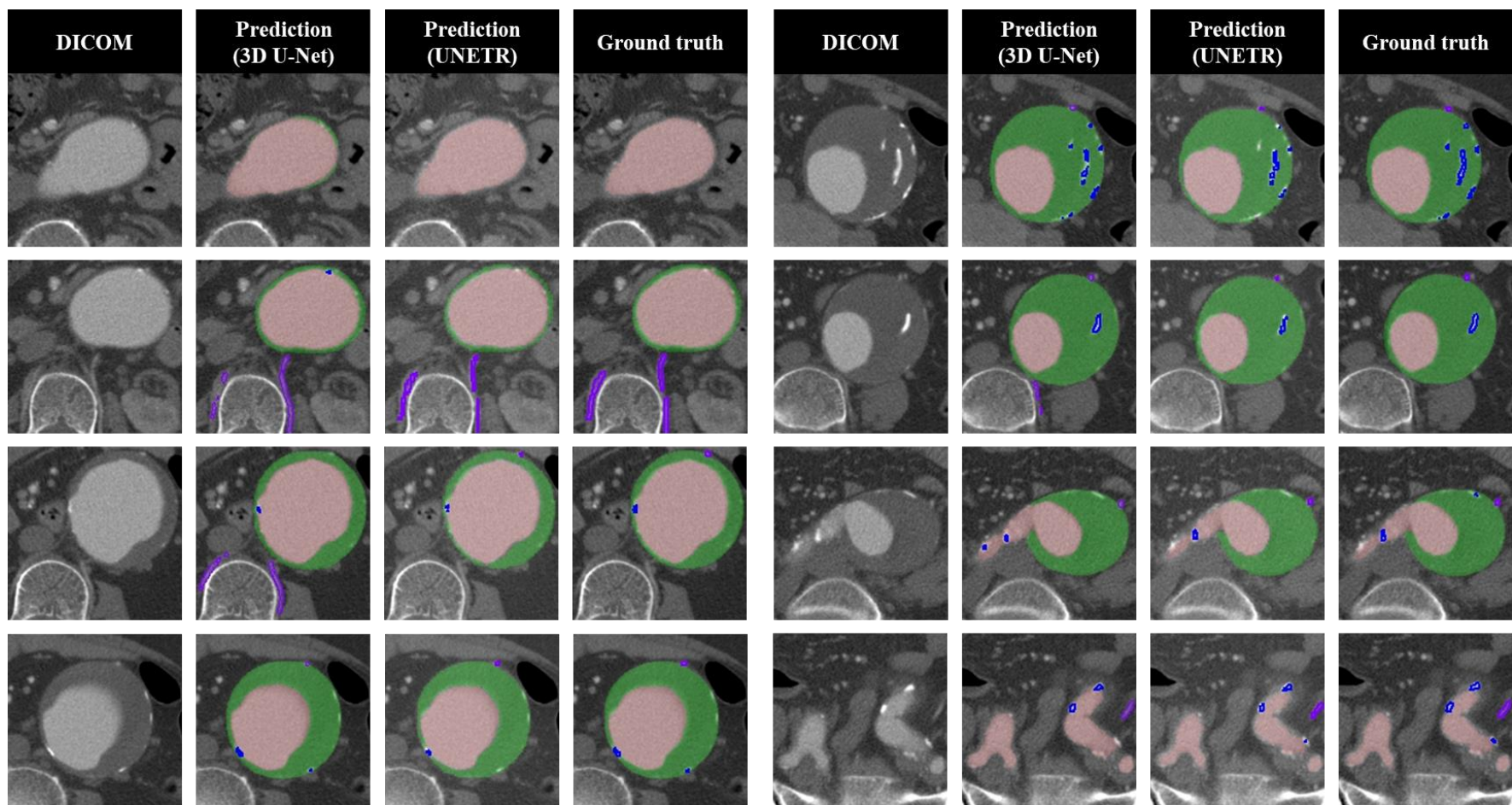


Figure 6-4. Best case for 3D U-Net with images, prediction (3D U-Net and UNETR), and ground truth

Based on the results of 4 studies in semi-automated segmentation, various analysis was conducted. It was observed that intra- and inter-observer variation occurs during manual segmentation and AL-corrected segmentation (Table 6-3). The difference between manual segmentation and AL-corrected segmentation, excluding calcification of observer 2, was shown within 2.00 mm and there was minimal differences between two observers in the all classes except for thrombus. The reason for inter-observer variation in thrombus is attributed to the difficulty in distinguishing between the area where blood is pooled and the region of the aortic wall in images with a slice thickness of 3.0 mm

Table 6-3 Intra- and inter-observer variation for 4 classes in abdominal aortic aneurysm.

	Difference	Aorta	Thrombus	Calcification	Vessels
Intra-observer variation	Observer 1	0.37	0.63	0.77	1.14
	Observer 2	0.36	0.56	2.36	1.15
Inter-observer variation	Manual segmentation	0.36	2.19	0.32	0.80
	AL-corrected segmentation	0.65	2.24	0.47	1.21

The networks demonstrated the best performance depending on the class in each study. Specifically, for the mandibular condyle, the cascade 3D U-Net outperformed the 3D U-Net at all stages, showing superior performance. In the case of the aorta in thoracoabdominal aortic dissection, both 3D U-Net and cascaded 3D U-Net demonstrated the best performance at all stages. However, for the vessels, the 3D U-Net exhibited the best performance in the stage 1, while SwinUNETR showed superior performance in the later stages. For abdominal aortic aneurysm, nnU-Net, which includes 3D U-Net, cascade 3D U-Net, and 2D-3D U-Net ensemble, demonstrated better performance than UNETR and SwinUNETR for all classes (Table 6-4).

Table 6-4. The best network for each stage and class in 4 studies

DSC	Classes	Stage 1	Stage 2	Stage 3	Stage 4	Stage 5
Kidney	Artery					
	Vein					
	Ureter		3D U-Net			-
	Parenchyma					
	RCC					
Mandibular condyle Condyle				Cascade 3D U-Net		
Thracoabdominal aortic dissection	Aorta	Cascade 3D U-Net	3D U-Net	Cascade 3D U-Net		
	Vessels	3D U-Net	SwinUNETR	SwinUNETR		
Abdominal aortic aneurysm	Aorta	Cascade 3D U-Net	Cascade 3D U-Net	Cascade 3D U-Net	2D-3D U-Net ensemble	2D-3D U-Net ensemble
	Thrombus	Cascade 3D U-Net	Cascade 3D U-Net	Cascade 3D U-Net	2D-3D U-Net ensemble	Cascade 3D U-Net
	Calcification	3D U-Net	Cascade 3D U-Net	2D-3D U-Net ensemble	Cascade 3D U-Net	2D-3D U-Net ensemble
	Vessels	Cascade 3D U-Net	Cascade 3D U-Net	Cascade 3D U-Net	Cascade 3D U-Net	3D U-Net

In addition, based on two aortic studies, we compared the differences between 2D and 3D approaches as well as high-resolution and low-resolution of CT images. The discrepancies in image dimensions showed that, except for vessels of stage 1, calcification of stage 2, and aorta and calcification of stage 3 in the abdominal aortic aneurysm, the 3D U-Net outperformed the 2D U-Net in all other classes. However, even when the 2D U-Net exhibited better performance, the discrepancy in DSC between the two networks was less than 1% (Table 6-5). In the comparison of high- and low-resolution CT images, we focused on the aorta and vessels in Stage 3 of thoracoabdominal aortic dissection using a dataset of 47 cases, as well as Stage 1 of abdominal aortic aneurysm using a dataset of 60 cases. The dataset for thoracoabdominal aortic dissection primarily consisted of high-resolution images with a slice thickness of 1.0 mm, while the dataset for abdominal aortic aneurysm predominantly comprised relatively low-resolution images with a slice thickness of 3.0 or 5.0 mm (Table 6-1). Comparing the results using 6 different networks, high-resolution images exhibited superior performance in all classes and networks, except for aorta when using the 2D U-Net. Particularly, for aorta, the difference of the DSC showed minimal errors ranging from -1.76% to 3.77%. However, for vessels, there was a substantial improvement in performance, with the difference ranging from 24.82% to 48.25% (Table 6-6). Therefore, vessels with a relatively smaller area and a high level of difficulty in labeling than aorta have a significant effect on image resolution.



Table 6-5. Comparison between 2D and 3D U-Net of nnU-Net in two aortic studies

Tasks	Stage	2D U-Net				3D U-Net			
		Aorta	Thrombus	Calcification	Vessels	Aorta	Thrombus	Calcification	Vessels
Thracoabdominal aortic dissection	1	0.857 ± 0.147			0.487 ± 0.109	0.945 ± 0.010			0.590 ± 0.030
	2	0.869 ± 0.119		-	0.554 ± 0.051	0.947 ± 0.010		-	0.616 ± 0.051
	3	0.880 ± 0.117			0.567 ± 0.038	0.951 ± 0.004			0.614 ± 0.062
Abdominal aortic aneurysm	1	0.898 ± 0.035	0.709 ± 0.206	0.593 ± 0.213	0.318 ± 0.141	0.913 ± 0.034	0.732 ± 0.229	0.678 ± 0.223	0.309 ± 0.146
	2	0.902 ± 0.038	0.698 ± 0.259	0.604 ± 0.137	0.294 ± 0.142	0.912 ± 0.037	0.737 ± 0.227	0.601 ± 0.161	0.374 ± 0.167
	3	0.910 ± 0.035	0.744 ± 0.200	0.670 ± 0.230	0.394 ± 0.185	0.909 ± 0.038	0.745 ± 0.227	0.665 ± 0.237	0.436 ± 0.206
	4	0.919 ± 0.026	0.752 ± 0.226	0.692 ± 0.230	0.394 ± 0.195	0.917 ± 0.038	0.758 ± 0.230	0.702 ± 0.198	0.441 ± 0.191
	5	0.922 ± 0.027	0.749 ± 0.223	0.686 ± 0.229	0.430 ± 0.186	0.926 ± 0.026	0.779 ± 0.190	0.702 ± 0.210	0.481 ± 0.154

Table 6-6. Comparison between high- and low-resolution with 6 networks in two aortic studies

Network	Classes	Thracoabdominal aortic dissection	Abdominal aortic aneurysm
UNETR	Aorta	$0.897 \pm 0.037$	$0.890 \pm 0.051$
	Vessels	$0.608 \pm 0.092$	$0.198 \pm 0.150$
SwinUNETR	Aorta	$0.927 \pm 0.027$	$0.895 \pm 0.050$
	Vessels	$0.722 \pm 0.073$	$0.240 \pm 0.156$
2D U-Net	Aorta	$0.880 \pm 0.117$	$0.898 \pm 0.035$
	Vessels	$0.567 \pm 0.038$	$0.318 \pm 0.141$
3D U-Net	Aorta	$0.951 \pm 0.004$	$0.913 \pm 0.034$
	Vessels	$0.614 \pm 0.062$	$0.309 \pm 0.146$
2D-3D U-Net ensemble	Aorta	$0.945 \pm 0.008$	$0.910 \pm 0.031$
	Vessels	$0.609 \pm 0.056$	$0.320 \pm 0.151$
Cascade 3D U-Net	Aorta	$0.951 \pm 0.007$	$0.914 \pm 0.033$
	Vessels	$0.621 \pm 0.063$	$0.363 \pm 0.141$

The second study conducted two experiments on automated 3D CAD modeling and measurement using a script-based API with Python, with data from thoracoabdominal aortic dissection and abdominal aortic aneurysm. In thoracoabdominal aortic dissection, we developed a semi-automated CAD modeling method for reconstructing grafts and compared its accuracy and modeling time with the conventional method. The semi-automated design requires manual inputs such as the creation and correction of center line for the main and vascular grafts, diameter of the main graft (ranging from 22–30 mm), type of graft reconstruction guide, and the extent of thoracoabdominal aortic dissection as determined by the surgeon. Centerline can be generated automatically, but it requires additional manual work such as removing unnecessary curves and performing smoothing to achieve an ideal centerline. Due to these additional tasks, the automation program does not include them. The conventional method and the automated method were compared, and the absolute mean differences were evaluated. The maximum difference was 50.10  $\mu\text{m}$  in the visualizing guide and 162.09  $\mu\text{m}$  in the marking guide (Table 4-2). The differences observed between the two modeling methods were attributed primarily to remeshing and smoothing of the triangles. Unlike parametric modeling based on 2D sketches, direct 3D modeling allows for greater flexibility in modifying the geometry and vector direction of the model, which can result in small deformations due to the edge length and number of iterations used for remeshing and mesh arrangement. On the other hand, the time of the automatic modeling for the visualizing guide was reduced to  $26.70 \pm 5.55$  min, more than approximately thirtyfold less than the conventional method. The marking guide was reduced to  $31.32 \pm 5.85$  min, about fortyfold less than the conventional method. Part inspection is closely related to modeling time as it can affect the throughput of unnecessary noise shells. If part inspection is not conducted, data processing for these shells may take a long time or continue indefinitely, resulting in longer modeling times. To address this issue, part inspection is performed to remove unnecessary noise shells, remesh uneven meshes, and auto-fix errors such as intersecting and overlapping triangles, inverted triangles, bad edges, and planar holes. We discovered that the absolute mean differences between the two modeling methods were relatively small, but the use of the automated modeling method dramatically reduced the modeling time compared to the conventional method. To improve the robustness of the evaluation, we added 5 patients for validation to confirm the accuracy and time spent. The accuracy for 5 patients for validation between conventional and automatic modeling was  $4.10 \pm 1.10$   $\mu\text{m}$  in the visualizing guide and  $3.59 \pm 1.90$   $\mu\text{m}$  in the marking guide, which is similar to the accuracies of 10 patients in the study (Table 6-7). In addition, the time spent for the 5 patients for

validation with the conventional and the automatic modeling methods were  $26.15 \pm 1.10$  min and  $1.33 \pm 0.5$  min for the visualizing guide, respectively, and  $30.52 \pm 3.17$  min and  $0.68 \pm 0.13$  min for the marking guide, respectively. The results dramatically reduced the time spent ( $P < 0.05$ ) (Table 6-8).

Table 6-7. Hausdorff average distance of 5 patients for validation between conventional and automated modeling methods with visualizing and marking guides. Note: CP, corresponding point.

Patients No.	Visualization guide			Marking guide		
	Distance ( $\mu\text{m}$ )	Max ( $\mu\text{m}$ )	# of CPs	Distance ( $\mu\text{m}$ )	Max ( $\mu\text{m}$ )	# of CPs
1	$5.10 \pm 3.03$	30.35	16,140	$6.44 \pm 3.07$	35.01	13,679
2	$3.53 \pm 3.14$	34.72	18,614	$3.34 \pm 2.37$	28.94	11,810
3	$4.17 \pm 3.50$	143.45	23,576	$2.74 \pm 2.46$	70.99	10,432
4	$5.14 \pm 3.36$	38.86	24,072	$2.56 \pm 2.43$	30.25	12,428
5	$2.55 \pm 2.37$	25.9	23,341	$2.62 \pm 2.33$	29.02	16,709

Table 6-8. Modeling time of 5 patients for validation with conventional and automated modeling methods consisted of two types of patient-specific graft reconstruction guides.

Patients No.	Visualizing guide(min)		Marking guide (min)	
	Conventional modeling method	Automated modeling method	Conventional modeling method	Automated modeling method
1	24.71	0.56	27.12	0.53
2	26.38	0.78	28.05	0.67
3	23.90	0.63	30.22	0.63
4	27.03	1.27	34.90	0.65
5	28.80	1.90	32.35	0.62

In AAA of CT angiography, we developed an automated CAD measurement method for clinically defined landmarks to select a commercially available graft stent that is suitable for patients with AAA growth and undergoing EVAR. The landmarks were classified into 7 categories based on the shape of the abdominal aorta: 1) aortic neck diameter, 2) aortic aneurysm diameter, 3) right iliac artery diameter, 4) left iliac artery diameter, 5) aortic neck length, 6) common iliac artery tortuosity, and 7) aortic neck angulation. In addition, we developed and applied module 1 (Algorithm 4-3) to obtain the maximum length of the curve by intersecting the plane with the aortic model, which is commonly used to measure each landmark and applied module 2 (Algorithm 4-4) to perform the measurement for landmarks. To perform all measurements, manual input data are required such as a 3D aortic model with thrombus, a centerline of the aortic model divided by the aortic neck, the aortic aneurysm, the right and left iliac artery, and a plane of the right and left iliac artery. By selecting the landmark, the desired automated measurement can be performed. The mean differences between manual and automated measurements showed a small range of errors from -2.80 mm to 0.23 mm for all measurements except for tortuosity of the iliac artery. However, tortuosity exhibited a relatively large range of errors from -9.80 mm to 8.30 mm in terms of both line and curve length on both sides. For the angulation between the centerline of the aortic neck and aneurysm, errors for 3 patients were observed in both manual and automated measurements when the angle was above or below 60 degrees (Table 4-5). The errors of a semi-automated measurement can be attributed to the variation in human input data obtained through the manual process of dividing the centerline, which is necessary for the automated measurement of aortic neck, aortic diameter, and left and right tortuosity involving curves and line lengths. To evaluate the human variation for input data, we conducted a correlation analysis among three researchers, which showed high agreement with 1.00 of ICC in all measurements, indicating the absence of human error for the automated measurements (Table 6-9). The causes of manual and automated measurement errors can be attributed to the fact that the conventional measurements were conducted based on 2D images, which differs from the 3D model-based approach. Specifically, the diameter measurements of the aortic neck, aneurysm, right and left iliac arteries were limited by the fact that the maximum diameter value was obtained by searching for the maximum diameter value among multiple slices in the axial view, and even if the slice with the maximum diameter value was identified, the shape of the aorta displayed in that slice appeared as an oval shape rather than a circular shape, making it difficult to obtain the major axis of the ellipse. Furthermore, the

tortuosity measured by the curve and line measurements and the aortic neck length was measured in the coronal view, which differs from the 3D model-based approach.

Table 6-9. Comparison of correlation between 3 researchers for in the aortic neck diameter, aortic neck length, right and left tortuosity including curve length, line length, and ratio.

Correlation		$r_{12}$	$p$	$r_{13}$	$p$	$r_{23}$	$p$
Aortic neck diameter		0.999	0.990	1.000	0.425	0.998	0.873
Aortic neck length		1.000	0.541	1.000	0.341	1.000	0.607
Rt.tortuosity	Curve length	1.000	0.539	1.000	0.539	1.000	*
	Line length	1.000	0.928	1.000	0.928	1.000	0.847
	Ratio	0.999	0.236	0.999	0.236	1.000	*
Lt.tortuosity	Curve length	1.000	0.195	1.000	0.195	1.000	*
	Line length	1.000	0.167	1.000	0.167	1.000	0.843
	Ratio	1.000	0.343	1.000	0.343	1.000	*

Note: \*All measurements are equal;  $r_{12}$ , correlation between researcher 1 and 2;  $r_{13}$ , correlation between researcher 1 and 3;  $r_{23}$ , correlation between researcher 2 and 3.

The third study aims to evaluate the accuracy and efficiency of patient-specific 3DP guides fabricated based on automated segmentation and modeling, and to clinically apply them. In thoracoabdominal aortic dissection of CT angiography, we developed two reconstruction techniques using 3D-printed patient-specific graft reconstruction guides. The first technique, called MBT, involved a visualizing guide based on a realistic-shaped graft model that included the main aortic body and its branching vessels. This allowed manual positioning of the branching grafts on the artificial aortic graft. The second technique, called GBT, utilized marking guides with slightly protruding marking points instead of the branching vessels in the visualizing guide. The surgical repair of Crawford extent II or III thoracoabdominal aortic dissection a challenging procedure associated with a high risk of mortality and complications. The traditional approach of utilizing a single patch to connect all the branches in the Crawford's island technique is no longer favored due to the potential risk of aneurysm formation in the remaining aortic island, especially in individuals with connective tissue disorders such as Marfan syndrome [118, 143-145]. The alternative approach is now favored in order to prevent the development of an aneurysm in the

reconstructed aorta [144, 146-148]. In cases where the branching arteries are widely separated, a graft with multiple branches may be necessary for successful treatment of the diseased aorta. However, the prevention of paraplegia is of utmost importance during the open surgical repair of thoracoabdominal aortic dissection, particularly in extent II and III, as it is a serious complication. The segmental arteries between thoracic-8 and lumbar-2 are crucial for protecting the spinal cord, and many institutions incorporate large intercostal arteries into their surgical approach to restore blood flow to the spinal cord [119, 149]. In order to address the risk of future patch aneurysms in patients undergoing open surgery for thoracoabdominal aortic dissection, we utilized personalized multi-branched aortic grafts that were fabricated using 3DP technology. This allowed for more precise reconstruction of the aorta during surgery and yielded favorable operative outcomes. In addition, we have implemented MBT and GBT techniques to further improve efficiency and accuracy. The aim of this retrospective study is to quantitatively evaluate the effectiveness of these techniques.

Park et al. [120] developed the octopod technique, which involves using an eight-branched aortic graft based on the IBT. However, performing the graft reconstruction using CT images while the patient is under anesthesia in the operating room can be difficult, as it hinders the ability to fully understand the patient's unique characteristics and limits the accuracy of the procedure. For example, the second patient's aortic anatomy was atypical due to severe scoliosis, which made it difficult to accurately mark the graft for replacement using conventional IBT based on CT scans. However, MBT and GBT techniques using visualizing and marking guides effectively overcame this anatomical challenge and shortened the graft marking time [58]. In our previous study, Rhee et al. [125] conducted a study on the use of 3DP guidance in open surgical repair of thoracoabdominal aortic dissection and aneurysm. Although the number of cases was small, the study found that patients who underwent 3DP had a shorter duration of cardiopulmonary bypass time, despite having more segmental arteries revascularized which typically requires longer bypass times. This suggests that 3DP may allow for more complete procedures with more segmental artery anastomoses, which can help prevent paraplegia and decrease bypass time. However, more research is needed due to the limited sample size and experience with 3DP guidance in this type of surgery.

We evaluated three techniques by conducting experiments using 135 mimic grafts ranging from the aortic arch to the iliac artery, with 15 patients, 3 researchers, and 3 techniques involved. These grafts were designed to mimic standard cylindrical model grafts, which can be a cost-effective alternative. The study compared the accuracy and time requirements of the DGM, conventional IBT, MBT, and GBT. The errors observed in the experiments were

categorized into marking errors with medical images, 3DP errors, and human errors. The conventional IBT technique had marking errors that were influenced by subjective measurements made from CT images. The direction of the segmental arteries was determined based on the horizontal line between the center points of the aorta and the segmental arteries, but for patients with aneurysms, the aorta appeared elliptical instead of circular in the axial view, which led to errors in determining the center point of the aorta and blood vessel (Figure 6-5) [21, 150].

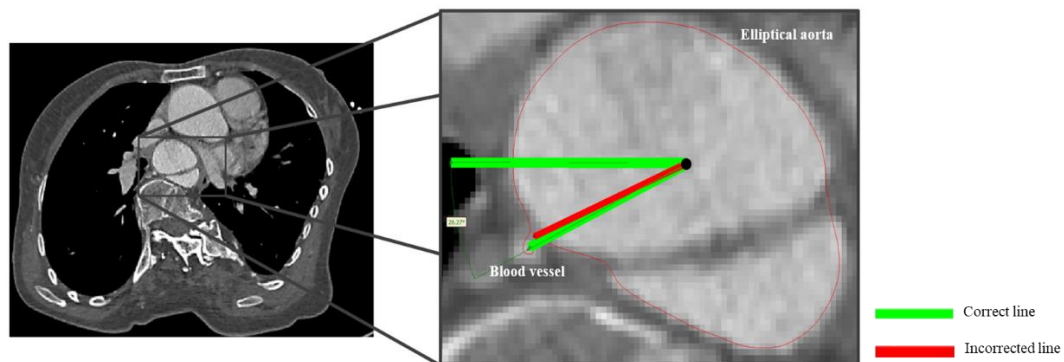


Figure 6-5. The subjective assessment and measurement error of elliptical aortic center and blood vessels in CT images. If a red line is selected instead of a green line, there is an error in angle measurement.

The differences of MBT and GBT arose from 3DP technologies errors, including machine and 3D printed model and guide errors. The errors in 3DP machines are influenced by various environmental factors, such as temperature, humidity, and vibration, as well as the materials, resolution, and duration of usage of the 3D printers. The errors in 3D printed models and guides are affected by factors like their size, shape, 3DP direction, and angle, as well as the post-processing methods used, such as support removal, ultraviolet polymerization, and surface smoothing [21, 48]. Furthermore, sterilization processes involving high temperatures, such as autoclave and steam sterilization, have the potential to cause deformation or distortion of the graft reconstruction guide [151]. To mitigate these issues, we have chosen to use ethylene oxide gas sterilization, which operates at a relatively lower temperature. Three techniques were identified as being susceptible to human errors. In experiments conducted by three researchers, errors arose when using a digital caliper and digital angle ruler to measure defined landmarks such as the diagonal line, height, and angle. In the Bland–Altman analysis, the conventional IBT showed wider ranges of differences in the measured diagonal line, height, and angles compared to the MBT and GBT. Specifically,



the ranges for the conventional IBT were -45.96 to 33.83 mm for the diagonal line, -46.70 to 33.34 mm for the height, and -39.05° to 13.05° for the angles. The differences among the diagonal line and height tended to fall in the negative or positive region as the distance between the segmental artery and celiac artery increased, and the differences between the angles tended to be mostly distributed in the negative region from zero. Outliers tended to appear in the IBT as the distances from the celiac artery from the segmental arteries increased in the diagonal line and height and occurred in patient with tortuous and swelling aneurysm aorta or scoliosis in the angle (Figure 5-5 (A)–(C)). For the MBT, the range of differences observed in the diagonal line, height, and angle measurements were -21.92 to 20.39 mm, -25.54 to 18.73 mm, and -39.97° to 23.04°, respectively. In the GBT, the corresponding ranges were -21.22 to 19.29 mm, -12.56 to 14.34 mm, and -40.61° to 15.31°, respectively (Table 5-2). The diagonal line and height measurements in both the MBT and GBT were predominantly distributed in the region of negative differences when the measured distance was smaller. Conversely, as the measured distance increased, the differences tended to be positive. The bias of the diagonal line and angles was more significant in the GBT, whereas the bias of the height measurement was greater in the MBT (Figure 5-5 (D)–(I)). Outliers observed in the MBT and GBT measurements had a more significant impact on the morphology of the aorta than on the distance between the segmental arteries. In addition, both the MBT and GBT methods resulted in a significant reduction in graft marking time, and the reduction in time was proportional to the number of segmental arteries (Figure 6-6).

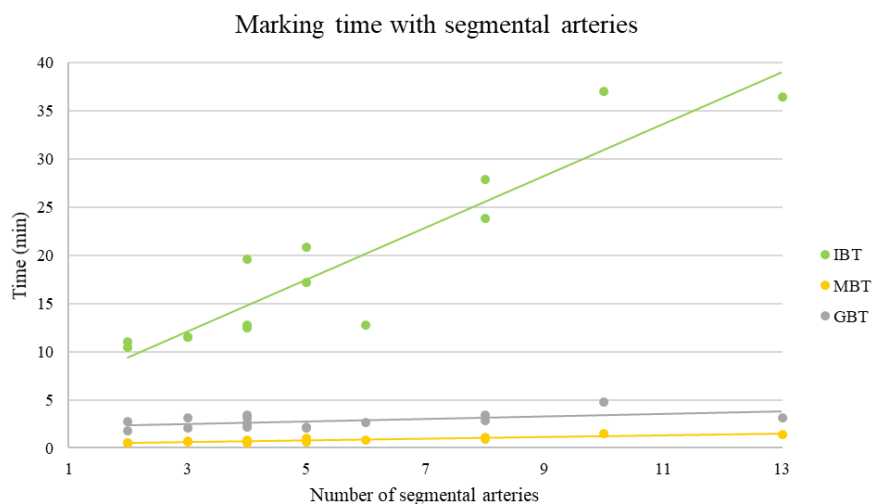


Figure 6-6. Making time according to the number of segmental arteries for IBT, MBT and GBT.

For example, the graft marking time required for the first patient, who had the smallest number of segmental arteries, was 10.5 minutes for the conventional IBT method, while it was reduced to 0.5 and 2.8 minutes with the MBT and GBT methods, respectively. For the fourteenth patient, who had 13 segmental arteries, the graft reconstruction time was 36.5 minutes for the IBT method, while it was reduced to 1.4 and 4.4 minutes with the MBT and GBT methods, respectively. On average, the MBT and GBT methods reduced the graft marking time by 17.4 and 15.5 minutes, respectively, representing a reduction of more than six times compared to the conventional IBT method (Figure 6-6). Despite the MBT being faster than the GBT for graft marking, the GBT showed higher accuracy. The correlation coefficient ( $r_{14}$ ) between the DGM and GBT was stronger for the diagonal line and height compared to the IBT ( $r_{12}$ ) and MBT ( $r_{13}$ ), while the angles had a similar level of correlation. This suggests that the GBT was the most similar to the DGM (Table 5-3). The ICC was used to assess the reproducibility of graft reconstruction among three researchers for the conventional IBT and the two new techniques. The results showed a high level of agreement for all techniques, with the GBT having an ICC of 0.995 and the IBT and MBT having an ICC of 0.986. After administering a questionnaire to three surgeons experienced in conventional IBT and the new techniques of MBT and GBT with 3DP, it was found that the latter two techniques with graft reconstruction guides were significantly more helpful to surgeons compared to conventional IBT.

There are several limitations and future studies for automated workflow. Firstly, the automated workflows were primarily based on small data, and trials involving multiple centers are necessary for validation. Secondly, it is crucial to reduce the various elements obtained through manual work such as correction of prediction and inputs of modeling. Thirdly, there is a need for the development and application of alternative technologies such as AR or VR to overcome the limitations of 3DP, including factors like printing time, cost, and equipment errors. In semi-automatic segmentation, the exploration of augmentation for each class in automated segmentation using deep learning, as well as optimization of parameters and development of more advanced networks, is necessary. Furthermore, deep learning was applied using only one CT phase from each study. However, it is known that there are organs that exhibit prominent features depending on the CT phase. Therefore, conducting training with multiple CT phases can enhance the accuracy for each class and improve the overall performance. In semi-automated design and measurement, the algorithm requires optimization for a wide of cases to enable a user-friendly and accessible approach without requiring specialized knowledge. In addition, abdominal aortic aneurysm was

measured in 300 patients as a retrospective study, but follow-up of patients after EVAR is needed for the graft stent determined after automated measurement in a future study. In developing the patient-specific guides fabricated using 3DP and clinical application, a more comprehensive solution is needed such as direct printing using bio-materials, which can be applied to surgery without graft reconstruction.

## **7 Conclusion**

In this paper, we developed an automated workflow that includes segmentation, 3D modeling, and measurement for the application of 3DP in medical field and demonstrated the usefulness and efficiency of 3DP technology for clinical applications. Firstly, the DL-based automated segmentation approach is developed using various networks such as 2D U-Net, 3D U-Net, cascade 3D U-Net, UNETR, and SwinUNETR with AL, which reduce labeling effort with smart labeling by dividing multiple stages and stress tests to determine an optimized dataset for training in kidney with RCC, mandibular condyle, thoracoabdominal aortic dissection, and abdominal aortic aneurysm. The preprocessing methods include intensity min-max normalization to rescale various ranges to a 0-1 range, resampling to resize different spatial resolutions to a common resolution, cropping to remove irrelevant regions such as background or empty space (foreground), padding to restore the removed areas to the original image size. Augmentation techniques include random rotation, random flip, random scaling, random elastic deformation, random noise, random Gaussian blur, and random gamma correction. Secondly, the automated 3D CAD modeling and measurement is developed with script-based API based on automated segmentation and compared with manual methods in thoracoabdominal aortic dissection and AAA. To perform design and measurement for patients with varying anatomical structures, we optimized and modularized the series of processes required for automated modeling in our approach. Finally, two graft reconstruction techniques, called MBT and GBT, were developed for open surgical repair of thoracoabdominal aortic dissection using patient-specific guides fabricated by SLA and CJP methods. The accuracy and efficiency of these techniques were confirmed through clinical application and compared to the conventional IBT method. We developed an automated method to minimize labor-intensive and time-consuming repetitive manual tasks and provided solutions to address the major challenges using 3DP technology. Furthermore, the development of such automated workflows not only enables the application of 3DP but also facilitates faster execution of physicians' diagnosis and treatment plans, anatomical

understanding of patients, and researchers' studies compared to conventional methods.

## References

1. Kim, G.B., et al., *Three-dimensional printing: basic principles and applications in medicine and radiology*. Korean journal of radiology, 2016. **17**(2): p. 182-197.
2. Mitsouras, D., et al., *Medical 3D printing for the radiologist*. Radiographics, 2015. **35**(7): p. 1965-1988.
3. Chen, J., et al., *Comparison of automatic and human segmentation of kidneys from CT images*. International Journal of Radiation Oncology, Biology, Physics, 2002. **54**(2): p. 82.
4. Dzung, L.P., X. Chenyang, and L.P. Jerry, *Current methods in medical image segmentation*. Annual review of biomedical engineering, 2000. **2**(1): p. 315-337.
5. Noble, J.A. and D. Boukerroui, *Ultrasound image segmentation: a survey*. IEEE Transactions on medical imaging, 2006. **25**(8): p. 987-1010.
6. Chen, X., et al., *Anatomy-regularized representation learning for cross-modality medical image segmentation*. IEEE transactions on medical imaging, 2020. **40**(1): p. 274-285.
7. Cai, L., J. Gao, and D. Zhao, *A review of the application of deep learning in medical image classification and segmentation*. Annals of translational medicine, 2020. **8**(11).
8. Doi, K., *Computer-aided diagnosis in medical imaging: historical review, current status and future potential*. Computerized medical imaging and graphics, 2007. **31**(4-5): p. 198-211.
9. Gao, J., et al., *Convolutional neural networks for computer-aided detection or diagnosis in medical image analysis: An overview*. Mathematical Biosciences and Engineering, 2019. **16**(6): p. 6536-6561.
10. Kubota, K., et al., *Medical image analysis: computer-aided diagnosis of gastric cancer invasion on endoscopic images*. Surgical endoscopy, 2012. **26**: p. 1485-1489.
11. Pham, D.L., C. Xu, and J.L. Prince, *Current methods in medical image segmentation*. Annual review of biomedical engineering, 2000. **2**(1): p. 315-337.
12. Withey, D.J. and Z.J. Koles. *Medical image segmentation: Methods and software*. in *2007 Joint Meeting of the 6th International Symposium on Noninvasive Functional Source Imaging of the Brain and Heart and the International Conference on Functional Biomedical Imaging*. 2007. IEEE.

13. Li, H., et al., *A novel PET tumor delineation method based on adaptive region-growing and dual-front active contours*. Medical physics, 2008. **35**(8): p. 3711-3721.
14. Farmaki, C., et al., *Spatially adaptive active contours: a semi-automatic tumor segmentation framework*. International journal of computer assisted radiology and surgery, 2010. **5**: p. 369-384.
15. Fritscher, K.D., et al., *Automatic segmentation of head and neck CT images for radiotherapy treatment planning using multiple atlases, statistical appearance models, and geodesic active contours*. Medical physics, 2014. **41**(5): p. 051910.
16. Chen, X., et al., *Medical image segmentation by combining graph cuts and oriented active appearance models*. IEEE transactions on image processing, 2012. **21**(4): p. 2035-2046.
17. Sjöberg, C. and A. Ahnesjö, *Multi-atlas based segmentation using probabilistic label fusion with adaptive weighting of image similarity measures*. Computer methods and programs in biomedicine, 2013. **110**(3): p. 308-319.
18. Gholipour, A., et al., *Multi-atlas multi-shape segmentation of fetal brain MRI for volumetric and morphometric analysis of ventriculomegaly*. NeuroImage, 2012. **60**(3): p. 1819-1831.
19. Wang, H., et al., *Multi-atlas segmentation with joint label fusion*. IEEE transactions on pattern analysis and machine intelligence, 2012. **35**(3): p. 611-623.
20. Sun, L., L. Zhang, and D. Zhang, *Multi-atlas based methods in brain MR image segmentation*. Chinese Medical Sciences Journal, 2019. **34**(2): p. 110-119.
21. Choi, J.-Y., et al., *Analysis of errors in medical rapid prototyping models*. International journal of oral and maxillofacial surgery, 2002. **31**(1): p. 23-32.
22. Tsagaan, B., et al. *An automated segmentation method of kidney using statistical information*. in *Medical Image Computing and Computer-Assisted Intervention—MICCAI 2002: 5th International Conference Tokyo, Japan, September 25–28, 2002 Proceedings, Part I 5*. 2002. Springer.
23. Hesamian, M.H., et al., *Deep learning techniques for medical image segmentation: achievements and challenges*. Journal of digital imaging, 2019. **32**: p. 582-596.
24. Zhao, Z.-Q., et al., *Object detection with deep learning: A review*. IEEE transactions on neural networks and learning systems, 2019. **30**(11): p. 3212-3232.
25. Long, J., E. Shelhamer, and T. Darrell. *Fully convolutional networks for semantic segmentation*. in *Proceedings of the IEEE conference on computer vision and pattern recognition*. 2015.

26. Chi, W., et al., *Deep learning-based medical image segmentation with limited labels*. *Physics in Medicine & Biology*, 2020. **65**(23): p. 235001.
27. Çiçek, Ö., et al. *3D U-Net: learning dense volumetric segmentation from sparse annotation*. in *Medical Image Computing and Computer-Assisted Intervention–MICCAI 2016: 19th International Conference, Athens, Greece, October 17-21, 2016, Proceedings, Part II 19*. 2016. Springer.
28. Wang, G., et al., *Interactive medical image segmentation using deep learning with image-specific fine tuning*. *IEEE transactions on medical imaging*, 2018. **37**(7): p. 1562-1573.
29. Yang, L., et al. *Suggestive annotation: A deep active learning framework for biomedical image segmentation*. in *Medical Image Computing and Computer Assisted Intervention– MICCAI 2017: 20th International Conference, Quebec City, QC, Canada, September 11-13, 2017, Proceedings, Part III 20*. 2017. Springer.
30. Wen, S., et al., *Comparison of different classifiers with active learning to support quality control in nucleus segmentation in pathology images*. *AMIA Summits on Translational Science Proceedings*, 2018. **2018**: p. 227.
31. Sourati, J., et al. *Active deep learning with fisher information for patch-wise semantic segmentation*. in *Deep Learning in Medical Image Analysis and Multimodal Learning for Clinical Decision Support: 4th International Workshop, DLMIA 2018, and 8th International Workshop, ML-CDS 2018, Held in Conjunction with MICCAI 2018, Granada, Spain, September 20, 2018, Proceedings*. 2018. Springer.
32. Mackowiak, R., et al., *Cereals-cost-effective region-based active learning for semantic segmentation*. *arXiv preprint arXiv:1810.09726*, 2018.
33. Kasarla, T., et al. *Region-based active learning for efficient labeling in semantic segmentation*. in *2019 IEEE winter conference on applications of computer vision (WACV)*. 2019. IEEE.
34. Gorriz, M., et al., *Cost-effective active learning for melanoma segmentation*. *arXiv preprint arXiv:1711.09168*, 2017.
35. Di Scandalea, M.L., et al., *Deep active learning for axon-myelin segmentation on histology data*. *arXiv preprint arXiv:1907.05143*, 2019.
36. Ock, J., et al., *Evaluation of skin cancer resection guide using hyper-realistic in-vitro phantom fabricated by 3D printing*. *Scientific Reports*, 2021. **11**(1): p. 8935.
37. Kwon, J., et al., *Modelling and manufacturing of 3D-printed, patient-specific, and anthropomorphic gastric phantoms: a pilot study*. *Scientific Reports*, 2020. **10**(1): p. 1-11.

38. Kang, S., et al., *Generation of customized orbital implant templates using 3-dimensional printing for orbital wall reconstruction*. Eye, 2018. **32**(12): p. 1864-1870.
39. Hong, D., et al., *Development of a personalized and realistic educational thyroid cancer phantom based on CT images: An evaluation of accuracy between three different 3D printers*. Computers in biology and medicine, 2019. **113**: p. 103393.
40. Hong, D., et al., *Usefulness of a 3D-printed thyroid cancer phantom for clinician to patient communication*. World journal of surgery, 2020. **44**: p. 788-794.
41. Hong, D., et al., *Development of patient specific, realistic, and reusable video assisted thoroscopic surgery simulator using 3D printing and pediatric computed tomography images*. Scientific Reports, 2021. **11**(1): p. 6191.
42. Zheng, H., et al., *CAD-based automatic path generation and optimization for laser cladding robot in additive manufacturing*. The International Journal of Advanced Manufacturing Technology, 2017. **92**: p. 3605-3614.
43. Xia, J., et al., *Three-dimensional virtual-reality surgical planning and soft-tissue prediction for orthognathic surgery*. IEEE transactions on information technology in biomedicine, 2001. **5**(2): p. 97-107.
44. Ong, S. and Y. Shen, *A mixed reality environment for collaborative product design and development*. CIRP annals, 2009. **58**(1): p. 139-142.
45. Nicolau, S., et al., *Augmented reality in laparoscopic surgical oncology*. Surgical oncology, 2011. **20**(3): p. 189-201.
46. Lorenz, M., et al., *CAD to VR—a methodology for the automated conversion of kinematic CAD models to virtual reality*. Procedia Cirp, 2016. **41**: p. 358-363.
47. Kwon, J., J. Ock, and N. Kim, *Mimicking the mechanical properties of aortic tissue with pattern-embedded 3D printing for a realistic phantom*. Materials, 2020. **13**(21): p. 5042.
48. Kim, T., et al., *Accuracy of a simplified 3D-printed implant surgical guide*. The Journal of prosthetic dentistry, 2020. **124**(2): p. 195-201. e2.
49. Kim, T., et al., *Accuracies of 3D printers with hard and soft materials*. Rapid Prototyping Journal, 2020. **26**(7): p. 1227-1235.
50. Han, P. and G. Zhao, *CAD-based 3D objects recognition in monocular images for mobile augmented reality*. Computers & Graphics, 2015. **50**: p. 36-46.
51. Moreno, R. and A. Bazán. *Design automation using script languages. High-level CAD templates in non-parametric programs*. in *IOP conference series: materials science and engineering*. 2017. IOP Publishing.
52. Joshi, H., et al. *Automated CAD modelling of mechanical components*. in

*International Conference on Communication and Signal Processing 2016 (ICCASP 2016)*. 2016. Atlantis Press.

53. Siddesh, S. and B. Suresh, *Automation of generating CAD models*. Journal of Mechanical Engineering and Automation, 2015. **5**(3B): p. 55-58.
54. Jayesh, P., H. Khairnar, and M.T.C. Cam, *Master Model Automation Using NX Unigraphics Customization*. International Journal of Engineering Development and Research, 2014. **2**(2): p. 2184-2189.
55. Hull, C., *Apparatus for production of three-dimensional objects by stereolithography*. US 4575330 A, Google Patents. 1986.
56. Whitaker, M., *The history of 3D printing in healthcare*. The Bulletin of the Royal College of Surgeons of England, 2014. **96**(7): p. 228-229.
57. Wong, K.V. and A. Hernandez, *A review of additive manufacturing*, *ISRN Mech. Eng*, 2012. **1**: p. 1-10.
58. Kim, W.K., et al. *3D-printing-based open repair of extensive thoracoabdominal aorta in severe scoliosis*. in *Seminars in Thoracic and Cardiovascular Surgery*. 2019. Elsevier.
59. Javan, R., D. Herrin, and A. Tangestanipoor, *Understanding spatially complex segmental and branch anatomy using 3D printing: liver, lung, prostate, coronary arteries, and circle of Willis*. Academic radiology, 2016. **23**(9): p. 1183-1189.
60. Dawood, A., et al., *3D printing in dentistry*. British dental journal, 2015. **219**(11): p. 521-529.
61. Alssabbagh, M., M. Abdulmanap, and R. Zainon, *Evaluation of 3D printing materials for fabrication of a novel multi-functional 3D thyroid phantom for medical dosimetry and image quality*. Radiation Physics and Chemistry, 2017. **135**: p. 106-112.
62. Chen, M.C., et al., *Deep learning to classify radiology free-text reports*. Radiology, 2018. **286**(3): p. 845-852.
63. Christ, P.F., et al. *Automatic liver and lesion segmentation in CT using cascaded fully convolutional neural networks and 3D conditional random fields*. in *International conference on medical image computing and computer-assisted intervention*. 2016. Springer.
64. Kim, K.H., S.H. Choi, and S.-H. Park, *Improving arterial spin labeling by using deep learning*. Radiology, 2018. **287**(2): p. 658-666.
65. Lakhani, P. and B. Sundaram, *Deep learning at chest radiography: automated classification of pulmonary tuberculosis by using convolutional neural networks*. Radiology, 2017. **284**(2): p. 574-582.



66. Liu, F., et al., *Deep learning MR imaging–based attenuation correction for PET/MR imaging*. *Radiology*, 2018. **286**(2): p. 676-684.
67. Yamashita, R., et al., *Convolutional neural networks: an overview and application in radiology*. *Insights into imaging*, 2018. **9**: p. 611-629.
68. Yasaka, K., et al., *Deep learning with convolutional neural network for differentiation of liver masses at dynamic contrast-enhanced CT: a preliminary study*. *Radiology*, 2018. **286**(3): p. 887-896.
69. Falk, T., et al., *U-Net: deep learning for cell counting, detection, and morphometry*. *Nature methods*, 2019. **16**(1): p. 67-70.
70. Livne, M., et al., *A U-Net deep learning framework for high performance vessel segmentation in patients with cerebrovascular disease*. *Frontiers in neuroscience*, 2019. **13**: p. 97.
71. Ma, X., et al., *U-Net based deep learning bladder segmentation in CT urography*. *Medical physics*, 2019. **46**(4): p. 1752-1765.
72. Al-Masni, M.A., et al. *A two cascaded network integrating regional-based YOLO and 3D-CNN for cerebral microbleeds detection*. in *2020 42nd Annual International Conference of the IEEE Engineering in Medicine & Biology Society (EMBC)*. 2020. IEEE.
73. Liu, J., et al., *A cascaded deep convolutional neural network for joint segmentation and genotype prediction of brainstem gliomas*. *IEEE Transactions on Biomedical Engineering*, 2018. **65**(9): p. 1943-1952.
74. Raju, M., et al., *Multi-class diagnosis of Alzheimer's disease using cascaded three dimensional-convolutional neural network*. *Physical and Engineering Sciences in Medicine*, 2020. **43**: p. 1219-1228.
75. Isensee, F., et al., *nnu-net: Self-adapting framework for u-net-based medical image segmentation*. *arXiv preprint arXiv:1809.10486*, 2018.
76. Hatamizadeh, A., et al. *Unetr: Transformers for 3d medical image segmentation*. in *Proceedings of the IEEE/CVF winter conference on applications of computer vision*. 2022.
77. Tang, Y., et al., *High-resolution 3D abdominal segmentation with random patch network fusion*. *Medical image analysis*, 2021. **69**: p. 101894.
78. Xu, Z., et al., *Efficient multi-atlas abdominal segmentation on clinically acquired CT with SIMPLE context learning*. *Medical image analysis*, 2015. **24**(1): p. 18-27.
79. Hatamizadeh, A., et al. *Swin unetr: Swin transformers for semantic segmentation of brain tumors in mri images*. in *Brainlesion: Glioma, Multiple Sclerosis, Stroke and Traumatic Brain Injuries: 7th International Workshop, BrainLes 2021, Held in Conjunction*

with MICCAI 2021, Virtual Event, September 27, 2021, Revised Selected Papers, Part I. 2022. Springer.

80. Tang, Y., et al. *Self-supervised pre-training of swin transformers for 3d medical image analysis*. in *Proceedings of the IEEE/CVF Conference on Computer Vision and Pattern Recognition*. 2022.

81. Kim, T., et al., *Active learning for accuracy enhancement of semantic segmentation with CNN-corrected label curations: Evaluation on kidney segmentation in abdominal CT*. Scientific reports, 2020. **10**(1): p. 366.

82. Hong, D., et al., *Development of a CT imaging phantom of anthropomorphic lung using fused deposition modeling 3D printing*. Medicine, 2020. **99**(1).

83. Ock, J., et al., *Patient-specific and hyper-realistic phantom for an intubation simulator with a replaceable difficult airway of a toddler using 3D printing*. Scientific Reports, 2020. **10**(1): p. 10631.

84. Camba, J.D., M. Contero, and P. Company, *Parametric CAD modeling: An analysis of strategies for design reusability*. Computer-Aided Design, 2016. **74**: p. 18-31.

85. González-Lluch, C., et al., *A survey on 3D CAD model quality assurance and testing tools*. Computer-Aided Design, 2017. **83**: p. 64-79.

86. Fu, J., X. Chen, and S. Gao, *Automatic synchronization of a feature model with direct editing based on cellular model*. Computer-Aided Design and Applications, 2017. **14**(5): p. 680-692.

87. Qin, X., Z. Tang, and S. Gao, *Automatic update of feature model after direct modeling operation*. Computer-Aided Design and Applications, 2021. **18**: p. 170-85.

88. Zou, Q. and H.-Y. Feng, *Push-pull direct modeling of solid CAD models*. Advances in Engineering Software, 2019. **127**: p. 59-69.

89. Lipson, H., et al., *3-D printing the history of mechanisms*. 2005.

90. Montero, M., et al., *Material characterization of fused deposition modeling (FDM) ABS by designed experiments*. Society of Manufacturing Engineers, 2001. **10**(13552540210441166): p. 1-21.

91. Sachs, E.M., et al., *Three-dimensional printing techniques*. 1993, Google Patents.

92. Asberg, B., et al., *Feasibility of design in stereolithography*. Algorithmica, 1997. **19**(1-2): p. 61-83.

93. Lan, P.-T., et al., *Determining fabrication orientations for rapid prototyping with stereolithography apparatus*. Computer-Aided Design, 1997. **29**(1): p. 53-62.

94. Patel, D.K., et al., *Highly stretchable and UV curable elastomers for digital light*

- processing based 3D printing*. *Advanced Materials*, 2017. **29**(15): p. 1606000.
95. Snyder, T.J., et al., *3D systems' technology overview and new applications in manufacturing, engineering, science, and education*. *3D printing and additive manufacturing*, 2014. **1**(3): p. 169-176.
96. Yang, H., et al., *Performance evaluation of projet multi-material jetting 3D printer*. *Virtual and physical prototyping*, 2017. **12**(1): p. 95-103.
97. Gaynor, A.T., et al., *Multiple-material topology optimization of compliant mechanisms created via PolyJet three-dimensional printing*. *Journal of Manufacturing Science and Engineering*, 2014. **136**(6).
98. Khaing, M., J. Fuh, and L. Lu, *Direct metal laser sintering for rapid tooling: processing and characterisation of EOS parts*. *Journal of Materials Processing Technology*, 2001. **113**(1-3): p. 269-272.
99. Kruth, J.P., et al., *Binding mechanisms in selective laser sintering and selective laser melting*. *Rapid prototyping journal*, 2005.
100. Polascik, T.J., et al., *Partial nephrectomy: technique complications and pathological findings*. *The Journal of urology*, 1995. **154**(4): p. 1312-1318.
101. Martín, O.D., et al., *Determinant factors for chronic kidney disease after partial nephrectomy*. *Oncoscience*, 2018. **5**(1-2): p. 13.
102. Pancherz, H., *A cephalometric analysis of skeletal and dental changes contributing to Class II correction in activator treatment*. *American Journal of Orthodontics*, 1984. **85**(2): p. 125-134.
103. Takada, K., S. Petdachai, and M. Sakuda, *Changes in dentofacial morphology in skeletal Class III children treated by a modified maxillary protraction headgear and a chin cup: a longitudinal cephalometric appraisal*. *The European Journal of Orthodontics*, 1993. **15**(3): p. 211-221.
104. De Clerck, H., L. Cevidanes, and T. Baccetti, *Dentofacial effects of bone-anchored maxillary protraction: a controlled study of consecutively treated Class III patients*. *American Journal of Orthodontics and Dentofacial Orthopedics*, 2010. **138**(5): p. 577-581.
105. Schiffman, E., et al., *Diagnostic criteria for temporomandibular disorders (DC/TMD) for clinical and research applications*. 2014.
106. Hwang, S.-J., et al., *Surgical risk factors for condylar resorption after orthognathic surgery*. *Oral Surgery, Oral Medicine, Oral Pathology, Oral Radiology, and Endodontology*, 2000. **89**(5): p. 542-552.
107. Cevidanes, L., et al., *Quantification of condylar resorption in temporomandibular*

- joint osteoarthritis*. Oral Surgery, Oral Medicine, Oral Pathology, Oral Radiology, and Endodontology, 2010. **110**(1): p. 110-117.
108. Schilling, J., et al., *Regional 3D superimposition to assess temporomandibular joint condylar morphology*. Dentomaxillofacial Radiology, 2014. **43**(1): p. 20130273.
109. Amorim, P., et al. *InVesalius: an interactive rendering framework for health care support*. in *Advances in Visual Computing: 11th International Symposium, ISVC 2015, Las Vegas, NV, USA, December 14-16, 2015, Proceedings, Part I II*. 2015. Springer.
110. Yushkevich, P.A., et al., *User-guided 3D active contour segmentation of anatomical structures: significantly improved efficiency and reliability*. Neuroimage, 2006. **31**(3): p. 1116-1128.
111. Velazquez, E.R., et al., *Volumetric CT-based segmentation of NSCLC using 3D-Slicer*. Scientific reports, 2013. **3**(1): p. 3529.
112. Kim, J.J., et al., *Reliability and accuracy of segmentation of mandibular condyles from different three-dimensional imaging modalities: A systematic review*. Dentomaxillofacial Radiology, 2020. **49**(5): p. 20190150.
113. Liu, Y., et al., *Tracking-based deep learning method for temporomandibular joint segmentation*. Annals of Translational Medicine, 2021. **9**(6).
114. Kim, Y.H., et al., *Automated cortical thickness measurement of the mandibular condyle head on CBCT images using a deep learning method*. Scientific Reports, 2021. **11**(1): p. 1-11.
115. Alam, S.R., et al., *Generalizable cone beam CT esophagus segmentation using physics-based data augmentation*. Physics in Medicine & Biology, 2021. **66**(6): p. 065008.
116. Liu, H., et al. *CU-Net: Cascaded U-Net with loss weighted sampling for brain tumor segmentation*. in *Multimodal Brain Image Analysis and Mathematical Foundations of Computational Anatomy: 4th International Workshop, MBIA 2019, and 7th International Workshop, MFCA 2019, Held in Conjunction with MICCAI 2019, Shenzhen, China, October 17, 2019, Proceedings 4*. 2019. Springer.
117. Ham, S., et al., *Multi-structure segmentation of hard tissues, maxillary sinus, mandible, mandibular canals in cone beam CT of head and neck with 3d u-net*. 2018.
118. Crawford, E.S. and R.W. DeNatale, *Thoracoabdominal aortic aneurysm: observations regarding the natural course of the disease*. Journal of vascular surgery, 1986. **3**(4): p. 578-582.
119. Coselli, J.S., et al., *Outcomes of 3309 thoracoabdominal aortic aneurysm repairs*. The Journal of thoracic and cardiovascular surgery, 2016. **151**(5): p. 1323-1338.

120. Park, S.J. and J.B. Kim, *An eight-branched aortic graft for reconstruction of visceral and intercostal arteries during extent II thoraco-abdominal aortic surgery*. *European Journal of Cardio-Thoracic Surgery*, 2018. **53**(6): p. 1282-1283.
121. Tanaka, H., et al., *The impact of preoperative identification of the Adamkiewicz artery on descending and thoracoabdominal aortic repair*. *The Journal of thoracic and cardiovascular surgery*, 2016. **151**(1): p. 122-128.
122. Katsargyris, A., et al., *Spinal cord ischemia after endovascular repair of thoracoabdominal aortic aneurysms with fenestrated and branched stent grafts*. *Journal of vascular surgery*, 2015. **62**(6): p. 1450-1456.
123. Etz, C.D., et al., *Thoracic and thoracoabdominal aneurysm repair: is reimplantation of spinal cord arteries a waste of time?* *The Annals of thoracic surgery*, 2006. **82**(5): p. 1670-1677.
124. Kim, T., et al., *Utilizing patient-specific 3D printed guides for graft reconstruction in thoracoabdominal aortic repair*. *Scientific Reports*, 2021. **11**(1): p. 18027.
125. Rhee, Y., et al. *Pre-sewn multi-branched aortic graft and 3D-printing guidance for Crawford extent II or III thoracoabdominal aortic aneurysm repair*. in *Seminars in Thoracic and Cardiovascular Surgery*. 2022. Elsevier.
126. Patro, S. and K.K. Sahu, *Normalization: A preprocessing stage*. arXiv preprint arXiv:1503.06462, 2015.
127. Yeghiazaryan, V. and I. Voiculescu, *Family of boundary overlap metrics for the evaluation of medical image segmentation*. *Journal of Medical Imaging*, 2018. **5**(1): p. 015006-015006.
128. Wanhainen, A., et al., *Editor's choice—European Society for Vascular Surgery (ESVS) 2019 clinical practice guidelines on the management of abdominal aorto-iliac artery aneurysms*. *European Journal of Vascular and Endovascular Surgery*, 2019. **57**(1): p. 8-93.
129. Chaikof, E.L., et al., *The Society for Vascular Surgery practice guidelines on the care of patients with an abdominal aortic aneurysm*. *Journal of vascular surgery*, 2018. **67**(1): p. 2-77. e2.
130. Lee, R., et al., *International opinion on priorities in research for small abdominal aortic aneurysms and the potential path for research to impact clinical management*. *International Journal of Cardiology*, 2017. **245**: p. 253-255.
131. Chandrashekar, A., et al., *Prediction of Abdominal Aortic Aneurysm Growth Using Geometric Assessment of Computerized Tomography Images Acquired During the Aneurysm Surveillance Period*. *Annals of surgery*, 2023. **277**(1): p. e175-e183.

132. Lee, R., et al., *Integrated plasma and tissue proteomics reveals attractin release by intraluminal thrombus of abdominal aortic aneurysms and improves aneurysm growth prediction in humans*. *Annals of Surgery*, 2022. **275**(6): p. 1206-1211.
133. Lee, R., et al., *Integrated physiological and biochemical assessments for the prediction of growth of abdominal aortic aneurysms in humans*. *Annals of surgery*, 2019. **270**(1): p. e1-e3.
134. Lee, R., et al., *Applied machine learning for the prediction of growth of abdominal aortic aneurysm in humans*. *EJVES short reports*, 2018. **39**: p. 24-28.
135. Vorp, D.A., M. Raghavan, and M.W. Webster, *Mechanical wall stress in abdominal aortic aneurysm: influence of diameter and asymmetry*. *Journal of vascular surgery*, 1998. **27**(4): p. 632-639.
136. Azar, D., et al., *Mechanical and geometrical determinants of wall stress in abdominal aortic aneurysms: A computational study*. *PLoS One*, 2018. **13**(2): p. e0192032.
137. Jalalahmadi, G., et al. *(Peak) Wall Stress as an indicator of abdominal aortic aneurysm severity*. in *2018 IEEE Western New York Image and Signal Processing Workshop (WNYISPW)*. 2018. IEEE.
138. Sternbergh III, W.C., et al., *Influence of endograft oversizing on device migration, endoleak, aneurysm shrinkage, and aortic neck dilation: results from the Zenith Multicenter Trial*. *Journal of vascular surgery*, 2004. **39**(1): p. 20-26.
139. Criado, F.J., et al., *Challenges in stent grafting: dealing with difficult neck and iliac artery anatomy*. *Perspectives in vascular surgery and endovascular therapy*, 2001. **14**(2): p. 41-55.
140. Mora, C.E., et al., *Maximum diameter of native abdominal aortic aneurysm measured by angio-computed tomography*. *Aorta*, 2015. **3**(02): p. 47-55.
141. Park, K.-H., et al., *Suitability of endovascular repair with current stent grafts for abdominal aortic aneurysm in Korean patients*. *Journal of Korean Medical Science*, 2011. **26**(8): p. 1047-1051.
142. Bland, J.M. and D. Altman, *Statistical methods for assessing agreement between two methods of clinical measurement*. *The lancet*, 1986. **327**(8476): p. 307-310.
143. Dardik, A., et al., *Aneurysmal expansion of the visceral patch after thoracoabdominal aortic replacement: an argument for limiting patch size?* *Journal of vascular surgery*, 2001. **34**(3): p. 405-410.
144. Kokotsakis, J., et al., *Thoracoabdominal aneurysm repair using a four-branched thoracoabdominal graft: a case series*. *Cases journal*, 2009. **2**: p. 1-4.

145. Tshomba, Y., et al., *Fate of the visceral aortic patch after thoracoabdominal aortic repair*. European journal of vascular and endovascular surgery, 2005. **29**(4): p. 383-389.
146. De Rango, P., et al., *Operative outcomes using a side-branched thoracoabdominal aortic graft (STAG) for thoraco-abdominal aortic repair*. European Journal of Vascular and Endovascular Surgery, 2011. **41**(1): p. 41-47.
147. Kim, I., et al., *Thoracoabdominal aortic aneurysm repair with a branched graft*. Annals of cardiothoracic surgery, 2012. **1**(3): p. 381.
148. Kouchoukos, N.T., A. Kulik, and C. Castner, *Branch graft patency after open repair of thoracoabdominal aortic aneurysms*. The Journal of thoracic and cardiovascular surgery, 2017. **153**(2): p. S14-S19.
149. Estrera, A.L., et al., *A quarter century of organ protection in open thoracoabdominal repair*. Annals of surgery, 2015. **262**(4): p. 660-668.
150. Koleilat, I., et al., *Interobserver variability in physician-modified endograft planning by comparison with a three-dimensional printed aortic model*. Journal of Vascular Surgery, 2016. **64**(6): p. 1789-1796.
151. Chen, J.V., et al., *Identifying a commercially-available 3D printing process that minimizes model distortion after annealing and autoclaving and the effect of steam sterilization on mechanical strength*. 3D printing in medicine, 2020. **6**(1): p. 1-10.

## Abstract (In Korean)

의료분야에서 3D 프린팅 기술은 환자 맞춤형 수술 가이드, 시뮬레이터, 수술 계획, 교육, 임플란트 등에 적용이 되어오고 있다. 의료에서 3D 프린팅 기술을 적용하기 위해서는 영상 획득, 분할, 3D CAD (Computed Aid Design) 모델링 혹은 측정과 같은 필수적인 작업이 수행되어야 한다. 그러나, 이러한 업무들은 반복적이고 수작업으로 진행되며 시간 소비적이고 노동 집약적인 업무가 될 수 있으며 작업자 간의 일관성도 부족하다. 이러한 단점을 해결하기 위해서 CT 영상을 기반으로 딥러닝 기술을 사용하여 분할 하고 3 차원 모델을 생성하여 스크립트 기반 API (Application Programming Interface) 를 이용하여 자동화 모델링을 함으로서 개선이 될 수 있다. 이 연구는 3 가지로 나뉘어서 진행하였다: 1) 레이블링 업무를 줄이기 위한 능동적 학습을 이용하여 자동화 및 강화된 분할, 2) 자동화된 분할을 기반으로 3D 모델을 생성하여 스크립트 기반 API 를 이용한 자동화된 환자 맞춤형 모델링과 특정 랜드마크에 대한 자동화 측정, 3) 3D 프린팅 기술을 이용하여 환자 맞춤형 수술 가이드 제작 및 임상 적용을 통한 환자 맞춤형 수술 가이드에 대한 유용성과 효율성을 증명하였다.

첫번째 연구에서 의료영상 분할은 인체 내 다양한 정보를 얻기 위해 필수적이며 해부학적 구조를 시각화 하여 의료진의 진단, 수술 계획, 장기 혹은 병변에 대한 정보를 제공할 수 있다. 기존 의료영상 분할은 여러 도구를 사용하여 픽셀 단위로 수동 혹은 반자동으로 분할하는 경우가 많았다. 그러나, 이러한 분할 방법은 낮은 대비, 영상 잡음 등 다양한 요인으로 인해 일관된 분할이 어렵고 많은 시간이 소요된다. 최근 몇 년 동안 심층 합성곱신경망 (convolution neural network, CNN), 완전 합성곱 네트워크 (fully convolutional networks, FCN), U-Net 등과 같은 모델을 사용하여 이미지 분할에서 상당한 발전을 이루고 있다. 이 연구에서는 흉복부 대동맥 박리 CT (Computed Tomography), 복부 대동맥류 CT, 하악과두 CBCT (Cone Beam CT), 신세포암을 포함한 신장 CT 에서 데이터셋을 기반으로 여러 단계로 나누고 레이블링이 진행된 초기의 소량 데이터셋에 대한 학습을 진행하여 새로운 데이터에 예측하고 전문가가 수정하는 작업을 반복하는 (Human in the loop) 능동적 학습 방법을 도입하였다. 네트워크는 3D U-Net, Cascade 3D U-Net, UNETR, SwinUNETR, 그리고 nnU-Net 을 연구에 따라 선택적으로 사용하여 능동적 학습을 수행했다. 평가 방법으로는 면적의 일치도를 평가하는 DSC (Dice similarity coefficient) 와 거리의 일치도를 평가하는 95% HD (Hausdorff distance)를 사용하여 일정한 데이터셋으로 나뉜 단계에 대한 정확성, 분할하고자 하



는 분류에 대한 정확성, 수동 분할과 스마트 레이블링을 이용한 분할 시간 비교, 최적화된 데이터 수를 결정하기 위한 스트레스 테스트를 수행하였다.

두번째 연구에서 자동화된 분할로 얻어진 3D 모델을 기반으로 3D CAD 기능을 이용하여 목적에 맞는 모델링이나 진단 및 병변 추적을 위한 랜드마크 측정이 이루어진다. CAD 시스템을 통해 디자인을 쉽게 수정하여 임상 적용에서 정확도를 높일 수 있으며 임상주의 특정 요구에 충족할 수 있도록 최적화 되어있다. 그러나, 수동적인 분할 작업과 마찬가지로 기존의 모델링 방식은 시간 소비적이고 상당한 노동력이 요구된다. 스크립트 기반 API를 이용한 자동화된 CAD 모델링 시스템은 기존 모델링 방법의 한계를 해결하기 위해 짧은 시간에 우수한 성능, 정확성 및 효율성을 제공한다. 자동화된 CAD 모델링은 일반적으로 3D 모델링에 대한 입력값과 매개변수를 설정하고 해당 사양을 기반으로 알고리즘 및 프로그래밍 코드를 생성하여 API를 통해 코드를 CAD 소프트웨어와 통합하여 모델링 및 수정이 가능하다. 흉복부 대동맥 박리 CT와 복부대동맥류 CT에서 자동화된 3D CAD 모델링 및 측정은 기존의 수동 방식과 비교하였으며 다양한 해부학적 구조를 가진 환자에 대한 설계 및 측정을 수행하기 위해 우리는 자동화 모델링에 필요한 일련의 과정을 최적화 및 모듈화하고 검증하였다. 평가 방법으로는 기존의 사용된 수동 방식과 자동화 CAD 모델링으로 수행된 3D 모델과 측정에 대한 정확성 그리고 모델링에 대한 소요 시간을 분석하였다.

마지막 연구에서 3D 프린팅 기술은 대부분의 의료기기가 일반적인 질병이나 성인에 맞게 개발되어 있거나 맞춤화 되어 소아, 희귀하고 복잡한 사례, 표준화되기 어려운 수술에 대한 임상적 미충족 수요를 해결할 수 있는 장점을 가지고 있다. 3D 프린팅 기술은 물체가 완전히 출력이 될 때까지 한 층씩 적층 하는 원리로 다양한 분야에서 적용되고 있다. 사용하는 재료, 출력 방식에 따라 다양한 방식으로 분류할 수 있으며 자동화된 분할과 3D CAD 모델링을 통해 얻어진 3D 모델을 STL으로 변환하여 알맞은 3D 프린팅 방식을 선택해 출력을 진행하고 멸균을 거쳐 임상에 적용된다. 흉복부 대동맥 박리에 대한 수술에서 환자 맞춤형으로 인공혈관 재건을 하기 위해서 3D 프린팅된 시각화 가이드를 이용한 모델 기반 기술과 마킹 가이드를 이용한 가이드 기반 기술을 개발하였다. 두개의 새로운 방법과 기존 이미지 기반 기술을 비교하여 정확성, 마킹 소요 시간, 재현성, 임상의를 대상으로 한 유용성과 효율성에 대한 설문조사 결과를 바탕으로 그 효과를 입증하였다. 3D 프린팅 가이드에 대한 오차는 외부 환경이나 3D 프린터의 사용 기간, 해상도, 사용된 재료, 3D 모델의 형상, 3D 프린팅 조건, 그리고 후처리 등

에 여러 영향으로 인해 3D 모델과의 차이가 발생할 수 있다.

결론적으로 우리는 3D 프린팅 기술을 임상에 적용하기 위한 절차인 분할과 모델링에 대한 자동화 워크플로우를 개발하였으며 기존 작업의 한계점인 반복적인 작업과 노동 집약적인 과정을 상당히 줄일 수 있었으며 코드화하여 작업에 대한 일관성 유지와 작업 시간 절약을 통한 작업자의 피로도를 완화 시키고 3D 프린팅 기술에 대한 적용을 기존 방법에 비해 가속화 하였다. 또한, 기존에 존재하는 임상적 미충족 수요를 3D 프린팅 기술로 제작된 수술 가이드를 적용하여 임상적 유용성과 효율성이 증명되었다.

Key words: Automation, Segmentation, Active learning (AL), Computer aided design

## Acknowledgements

### 감사의 글

2016년 12월을 시작으로 학부생 신분에서 석사를 거쳐 마침내 박사 학위 과정까지 끝을 맺게 되었습니다. 지난 6년반 이라는 시간을 돌이켜 보면 아쉬움과 후회가 남지만 이 시간들이 저에게 있어서 감사한 시간이 였고 공학 박사로서 성장을 할 수 있었던 잊지 못할 중요한 시간들이었습니다. 이러한 결실을 맺기 까지 그동안 주변에서 많은 도움을 주시고 격려와 응원을 해주신 덕분에 박사 과정이라는 힘든 여정에 마침표를 찍을 수 있게 되었습니다.

학문과 연구가 무엇인지 깨달음을 주시고 부족했던 저를 아낌없이 지도를 해주신 김남국 교수님께 감사의 말씀을 전합니다. 교수님의 가르침으로 인해 의학과 공학에 대한 융합 연구를 배울 수 있었으며 연구에 대한 시야를 넓힐 수 있었고 연구자로서의 실적도 많이 쌓을 수 있도록 이끌어주셔서 감사합니다. 의학적인 관점에서 여러 지도를 해주신 양동현 교수님께 감사의 말씀을 전합니다. 함께 연구를 진행함으로써 의료의 미충족 수요들을 파악하여 공학적으로 해결할 수 있는 능력을 키울 수 있었습니다. 그리고, 연구실 생활 초기 팀을 이끌어 주시고 지금까지 저의 연구를 지켜봐주신 김국배 대표님께 감사의 말씀 전합니다. 박사과정을 시작하기 전 막연한 두려움이 있었을 때 대표님께서 격려 해주신 덕분에 용기내어 박사과정을 시작 할 수 있었습니다. 또한, 바쁘신 와중에 박사 심사와 졸업논문에 대해서 의학적인 관점에서 가치 있는 조언을 해주신 고범석 교수님, 유진수 교수님께도 감사의 말씀 전합니다. 교수님들의 의견을 보완하여 한층 더 완성도가 높은 졸업 논문을 작성하였습니다.

저의 첫 사수이자 의료 3D 프린팅에 대한 모든 것을 알려주신 이상욱 선생님, 석사, 박사 학위까지 약 6년이라는 긴 시간 동안 함께 고생하신 홍다영 선생님, 연구에 대해서 조언을 구하고 의견을 나눌 수 있는 옥준혁 선생님, 유일한 연구실 동기이자 정신적 지주가 되어준 권진희 선생님, 딥러닝에 대한 지식을 알려 주시고 박사 졸업에 도움을 주신 함성원 교수님, 저와 비슷한 연구를 하시는 온성철 선생님, 열정을 가지고 연구하시는 김현정 선생님, 항상 밝은 모습을 보이는 김지연씨도 깊은 감사의 마음을 전합니다. 선생님들이 계셨기에 함께 다양한 연구를 하면서 결과를 만들고 즐겁게 연구를 할 수 있었습니다. 이외에도 저

와 같이 연구를 했었고 하고 계신 연구원분들께 감사한 마음을 전하고 좋은 결과가 있기를 바라겠습니다.

마지막으로 지금의 제가 있기 까지 항상 곁에서 힘이 되어주시고 관심을 가져 주신 아버지와 어머니, 그리고 형에게도 감사의 말을 전합니다. 많은 분들의 도움과 성원이 있었기에 힘든 과정을 견디고 한 분야의 어엿한 박사가 되었습니다. 온전히 저 혼자만의 노력만으로는 불가능 했을 것이라 생각하며 지금까지 달려온 것 처럼 앞으로도 더 성장할 수 있는 연구자가 될 수 있도록 최선과 노력을 다 하도록 하겠습니다.